UiT
THE ARCTIC
UNIVERSITY
OF NORWAY

Faculty of Science and Technology

Reconstruction of ice stream retreat and palaeoceanographic development during the deglaciation and Holocene in the Storfjorden Trough, Svalbard

Based on geophysical data, benthic foraminiferal and sedimentological records

—

Christine Lockwood
Master thesis in Marine Geology and Geophysics (GEO-3900)
May 2016

Abstract

Here we investigate the retreat of a palaeo-ice stream and the subsequent palaeoceanographic development in the eastern Storfjorden Trough during the deglaciation and Holocene. The results are based on multibeam bathymetric and acoustic sub-bottom data, and a multiproxy analysis of a ^{14}C dated sediment core (including benthic foraminifera, $\delta^{13}C$, $\delta^{18}O$ and sedimentology). The ice stream experienced a rapid retreat with a still-stand of the grounding line leading to the deposition of a glacial sediment lobe (<14,000 cal. years). Atlantic Water has continuously been present in the eastern Storfjorden Trough since the Allerød interstadial, following the rapid retreat of the ice stream and onset of glaciomarine sedimentation (c. 13,800 cal. years). The Younger Dryas (c. 12,700 cal. years) and late Holocene (c. 4000 cal. years) were identified as cold periods characterised by reduced Atlantic Water inflow and extensive sea ice cover. Warmer periods in the early Holocene (c. 9000 cal. years) and mid-Holocene (after c. 8200 cal. years) were characterised by a prevalence of Atlantic Water. The reconstruction of the retreat of the palaeo-ice stream and palaeooceanographic development presented gives a further understanding of the dynamic responses of ice-ocean interactions to past climatic changes.

Keywords

Palaeoceanography; deglaciation; ice stream; retreat; Atlantic Water; Arctic water; Storfjorden; benthic foraminifera; oxygen isotopes; carbon isotopes.

Acknowledgements

Firstly, I would like to thank my supervisors: Professor Tine L. Rasmussen at the University of Tromsø (UiT) for her advice and support throughout my thesis, and help with the identification of the foraminifera; and Professor Riko Noormets at The University Centre in Svalbard (UNIS) for his guidance with the interpretation of the geophysical data.

I would like to thank: the laboratory staff at UiT Trine Dahl and Ingvild Hald for their help with using the equipment; the crew on board the R/V Helmer Hanssen in September 2013 for collecting the CTD, multibeam bathymetry, acoustic sub-bottom profile (chirp) data and recovery of the sediment core HH13-26-GC; the laboratory staff at the 14CHRONO Centre, Queens University Belfast for the AMS radiocarbon analysis; and Professor Martin Jakobsson and the laboratory staff at Stockholm University for the analysis of the stable isotopes.

I am happy to say thank you and goodbye to my best friend of many months, my trusty microscope I used for the identification of the foraminifera. We became well acquainted during our time together and I think I spent more time with it than my husband! Safe to say I could see foraminifera when I closed my eyes at night!

Finally, I would like to thank my husband, Grace Ireland for your support and encouragement throughout all of my studies. Sitting inside doing laboratory work and writing my thesis in such an amazing place as Svalbard has been very difficult, but I think I found a great balance between studying and enjoying the life up here. Thank you for Grace for coming on many adventures with our sled dogs, if I didn’t get out on trips with you guys I think I would have gone insane!

Christine Lockwood

Longyearbyen, May 2016

Contents

1. Introduction……………………………………………………………………...1

1.1 Objectives…………………………………………………………………………1

1.2 Background………………………………………………………………………1

1.2.1 The Arctic Ocean…………………………………………………………1

1.2.2 The Svalbard Archipelago……………………………………………......4

1.2.3 Glacial history of Svalbard and the Barents Sea……………………………6

1.2.4 Bølling-Allerød interstadials…………………………………………..……8

1.2.5 Younger Dryas stadial………………………………..…………………..8

1.2.6 Holocene…………………………………………..………………...9

2. Study area…………………………………………………………………………11

2.1 Oceanographic and environmental setting……………………………………………11

3. Methods……………………………………………………………………...15

3.1 Core recovery……………………………………………………………………16

3.2 Geophysical data…………………………………………………………...16

3.2.1 Multibeam bathymetric data…………………………………………...…..16

3.2.2 SIMRAD echo sounder…………………………………………….....16

3.2.3 Acoustic sub-bottom profile (Chirp) data..……………………………...…16

3.3 Conductivity, temperature, depth (CTD) data……………………………………..16

3.4 Laboratory work………………………………………………………………...17

3.4.1 Magnetic susceptibility (loop sensor)……………………………...………17

3.4.1.1 Principle…………………......…………………………...…..17

3.4.1.2 Procedure…………………………………………………...…17

3.4.2 Sedimentology………………………………………………..…...18

3.4.3 Magnetic susceptibility (point sensor)……………………………………....18

3.4.4 Shear Strength………………………………………………………..……19

3.4.5 X-radiographs……………………………………………………….......19

3.4.5.1 Principle………………………………………………………19

3.4.5.2 Procedure………………………………………………..........…20

3.4.6 Sediment sample preparation……………………………………………20

3.4.7 Freeze drying……………………………………………………………20

3.4.8 Sieving……………………………………………………………......21

3.4.9 Grain size analysis………………………………………………….....…21

3.4.10 Ice-rafted debris………………………………………………………..…21

3.4.11 Foraminiferal analysis…………………………………………........…22

3.4.12 Preservation of foraminifera……………………………………………….23

3.4.13 Radiocarbon dating…………………………………………………......…24

3.4.13.1 Principle……………………………………………………....24

3.4.13.2 Assumptions and sources of error……………………….....……25

3.4.13.3 Accelerator mass spectrometry radiocarbon analysis..……..…....27

3.4.13.4 Calibration…………………………………………………...….29

3.4.14 Age model and accumulation rates…………………………..……......29

3.4.15 Stable isotopes…………………………………………………….…..30

3.4.15.1 Principle……………………………………………………....…30

3.4.15.2 Oxygen isotopes……………………………………………..…31

3.4.15.3 Oxygen isotope limitations……………………..…………...32

3.4.15.3 Carbon isotopes…………………………………………..…….33

3.4.15.4 Carbon isotope limitations……………………………...…..35

3.4.15.5 Stable isotope analysis………………………………...……36

3.5 Processing and illustration of data…………………………………….…..…38

4. Foraminifera……………………………………………………………...39

4.1 Background and ecology……………………………………………..…39

4.2. Foraminifera ecology………………………………………………......40

4.2.1 Ecology of calcareous benthic species…………………………..….41

4.2.1.1 *Cassidulina reniforme* (Nørvangi, 1945)……………….…...41

4.2.1.2 *Elphidium excavatum* forma *clavata* (Cushman, 1930)………41

4.2.1.3 *Nonionellina labradorica* (Dawson, 1860)…………….…….42

4.2.1.4 *Islandiella norcrossi* (Cushman, 1933)………………….…..43

4.2.1.5 *Cibicides lobatulus* (Walker and Jacob, 1798)……………...43

4.2.1.6 *Melonis barleeanus* (Williamson, 1858)……………….…43

4.2.1.7 *Cassidulina neoteretis* (Seidenkrantz, 1995)……………..…44

4.2.1.8 *Elphidium subarcticum* (Cushman, 1944)…………………..44

4.2.1.9 *Buccella frigida* (Cushman, 1922), *Buccella tenerrima* (Bandy, 1950)………………………………………………44

4.2.1.10 *Stainforthia loeblichi* (Feyling-Hanssen, 1954)……………..44

4.2.1.11 *Astrononion gallowayi* (Loebilch & Tappan, 1953)………..45

4.3.2 Agglutinated benthic species………………………………………45

4.3.2.1 *Adercotryma glomerata* (Brady, 1878)……………………..45

4.3.3 Planktonic species…………………………………………………45

4.3.3.1 *Neogloboquadrina pachyderma* (sinistral) (Ehrenberg, 1861) 45

4.3.3.2 *Neogloboquadrina pachyderma* (dextral) (Ehrenberg, 1861)...46

4.3.3.3 *Globigerina/Globigerinita* spp. (d'Orbigny, 1826; Ehrenberg 1861; Egger, 1893)……………………………………...46

5. Results…………………………………………………………………47

5.1 Bathymetry……………………………………………………………………47
   5.1.2 Description……………………………………………………………47
5.2 Sub-bottom profile and acoustic units....……………………………………48
5.3 Modern hydrography………………………………………………………..51
5.4 Sedimentology………………………………………………………………52
   5.4.1 Lithological description………………………………………………53
   5.4.2 X-radiographs……………………………………………………...53
   5.4.3 Magnetic susceptibility……………………………………………….54
   5.4.4 Shear strength………………………………………………….……..56
   5.4.5 Water content…………………………………………………...…56
   5.4.6 Grain size distribution……………………………………………..56
   5.4.7 Ice-rafted debris concentration……………………………………….58
   5.4.8 Lithological units…………………………………………………..58
      5.4.8.1 Diamicton unit (L1) (283-171 cm)…………………………60
      5.4.8.2 Fine-grained mud unit (L2) (171-0 cm)……………………60
5.5 AMS radiocarbon dating and age model……………………………………..61
5.6 Sedimentation rates…………………………………………………………..63
   5.6.1 Mass accumulation rates……………………………………………..63
   5.6.2 Ice-rafted debris and sediment flux…………………………………..63
5.7 Stable isotopes………………………………………………………………..66
   5.7.1 δ^{13}C record…………………………………….………………66
   5.7.2 δ^{18}O record…………………………………………...………67
5.8 Foraminifera…………………………………………………………………69
   5.8.1 Benthic foraminifera…………………………………………………..69
   5.8.2 Benthic foraminiferal assemblage zones………………………………73

5.8.2.1 Assemblage zone 1 (AZ1) (170-154 cm)…………………...73

5.8.2.2 Assemblage zone 2 (AZ2) (154-130 cm)……………………73

5.8.2.3 Assemblage zone 3 (AZ3) (130-110 cm)……………………74

5.8.2.4 Assemblage zone 4 (AZ4) (110-106 cm)……………………75

5.8.2.5 Assemblage zone 5 (AZ5) (106-74 cm)……………………..76

5.8.2.6 Assemblage zone 6 (AZ6) (74-30 cm)………………………76

5.8.2.7 Assemblage zone 7 (AZ7) (30-0 cm)………………………..77

5.8.3 Planktonic foraminifera……………………………………..…78

6. Interpretation and Discussion…………………………………………………81

6.1 Last Glacial Maximum and early deglaciation (<14,000 cal. years)……....88

6.2 Allerød interstadial and the Younger Dryas (c. 13,800-11,500 cal. years)..100

6.3 Early Holocene (c. 11,500-8200 cal. years)………………………………106

6.4 Mid-Holocene (c. 8200-4000 cal. years)…………………………………..109

6.5 Late Holocene-recent (the last 4000 cal. years)…………………………...113

7. Conclusions…………………………………………………………….…...…117

References………………………………………………………………………..119

1. Introduction

1.1 Objectives

In this study, we present results based on geophysical data, and foraminiferal and sedimentological records from a sediment core recovered from approximately 112 km east from the mouth of the Storfjorden Trough, Svalbard using a multi-proxy approach. An age model for the core is presented based on lithological composition and is constrained by accelerator mass spectrometry (AMS) radiocarbon dates.

We aim to present the first reconstruction of the retreat of the palaeo-ice stream in the eastern Storfjorden Trough and the development of post-glacial palaeooceanography and palaeoenvironment, with a main focus on the inflow of Atlantic Water. The reconstruction of high-latitude depositional settings, sedimentation pathways, palaeooceanography and palaeoenvironment environment in glacially influenced systems is critical to understanding the dynamic responses of ice-ocean interactions to past climatic changes.

1.2 Background

1.2.1 The Arctic Ocean

The Arctic Ocean is the smallest of the world's oceans and is situated north of the polar circle, encompassing the Greenland Sea, Iceland Sea, Norwegian Sea and Barents Sea (Fig. 1). It is characterised by wide, shallow continental shelves that flank four deep central basins, which are divided by submarine ridges (Rudels, 2009) (Fig. 1).

The Arctic Ocean is considered to be the isolated as it is surrounded by continental landmasses, with only three oceanic passages linking it to the rest of the oceans (Rudels, 2009; O'Regan et al., 2011). The Bering Strait is shallow (45 m) and narrow (50 km) connecting the Arctic Ocean to the Pacific Ocean and is situated between western Canada and Russia (Fig. 1). There are several shallow (150-230 m) and narrow channels in the Canadian

Arctic Archipelago, linking it to the north Atlantic (Rudels, 2009). The Fram Strait is a unique oceanic gateway and is the only deep water (~2500 m) connection from the Arctic Ocean to the north Atlantic, situated between northeast Greenland and the Svalbard Archipelago (Thiede et al., 1990; Klenke and Schenke, 2002) (Fig. 1).

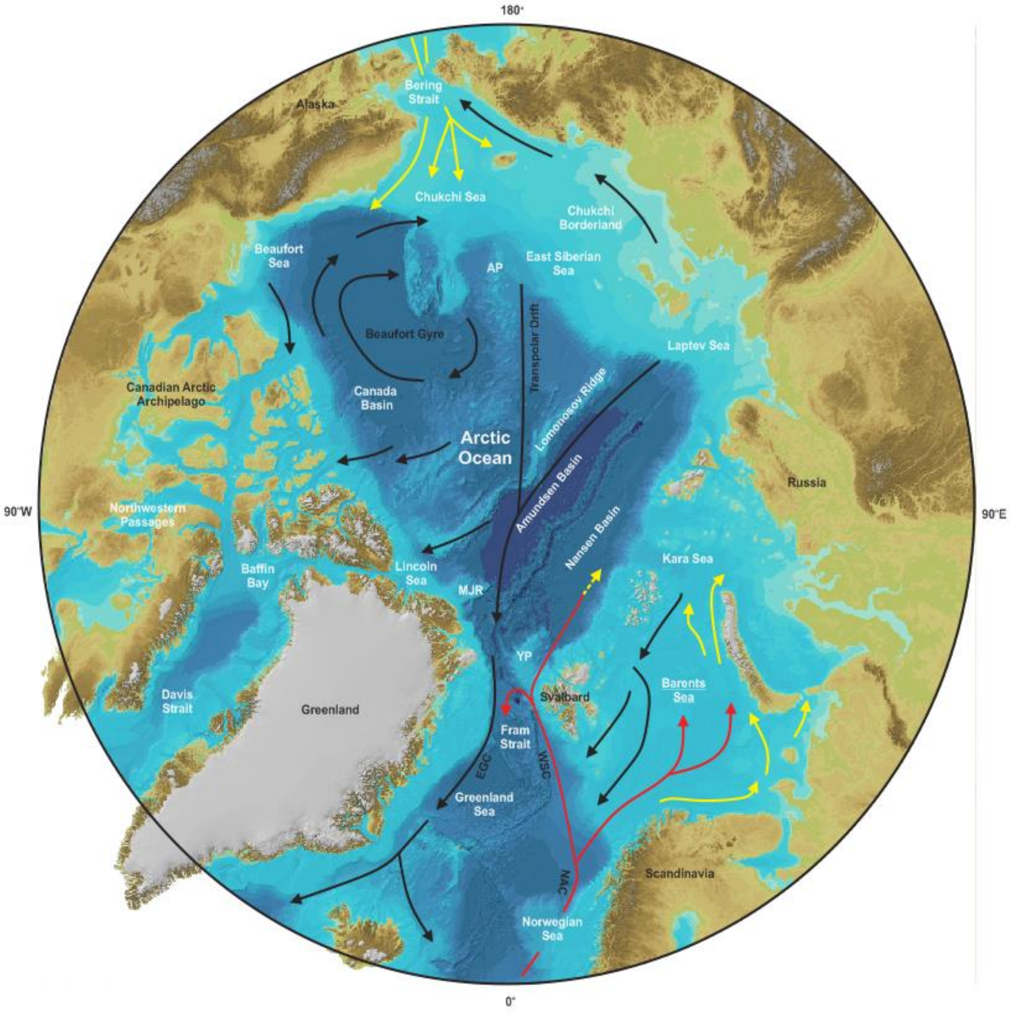

Figure 1: Map of the Arctic Ocean based on the International Bathymetric Chart of the Arctic Ocean (IBCAO) Version 3.0 (Jakobsson et al., 2012). The general circulation of the surface water masses in the present Arctic Ocean is shown (modified from Rudels et al., 2012). Warm Atlantic currents are indicated by red arrows, cold, less-saline polar water and Arctic currents by black arrows and low-salinity transformed currents are shown by yellow arrows. AP = Arlis Plateau; EGC = East Greenland Current; MJR = Morris Jesup Rise; NAC = North Atlantic Current; WSC = West Spitsbergen Current; YP = Yermak Plateau.

The physical oceanography in the Arctic Ocean predominantly consists of three stratified layers; surface water, intermediate water and bottom waters that are topographically steered throughout the central Arctic Ocean (Rudels, 2009). The present oceanographic regime of the surface waters is dominated by the bidirectional flow of two water masses in the Fram Strait. The West Spitsbergen Current (WSC) transports warm, saline Atlantic surface waters northward along the eastern Fram Strait, which cool and form the subsurface intermediate Atlantic Waters that circulate throughout the Arctic (Fig. 1). The western Fram Strait provides a major route for cold, fresh polar surface waters and sea ice export out of the Arctic as the East Greenland Current (EGC) (Quadfasel et al., 1987; Klenke and Schenke, 2002) (Fig. 1).

Mixing of Atlantic Water with Polar water forms Arctic water that are observed in the Barents Sea (Skogseth et al., 2005). The density gradient produced by these water masses forms two oceanic fronts; the contact zone between the Polar water-Arctic water is the Polar Front and the contact zone between the Arctic water-Atlantic Water is the Arctic Front (Piechura and Walcozowski, 1995). The position of these oceanic fronts controls sea ice extent and hence the marginal ice zone (MIZ), which is an area that promotes primary production (Quadfasel et al., 1987; Zamelczyk et al., 2013).

The Arctic Ocean also receives inflow from the Pacific Ocean of low salinity water (Fig. 1) and outflow of cold, Arctic surface water also occurs through the shallow Canadian Arctic Archipelago (Rudels, 2009).

Although the Arctic is the smallest of the world’s oceans, its physiography and oceanography has a pivotal role in regulating many climatic processes. Sea ice influences atmosphere-ocean heat exchanges due to its high albedo and its formation is the main driver of deep-water formation (Curry et al., 1995). The transport of warm surface Atlantic Water into the Arctic supplies the primary source of heat and salt into this region (Aagaard et al., 1985). The subduction of Atlantic Water combined with deep-water formation is the driving mechanism for the Atlantic Meridional Overturning Circulation (AMOC) that influences global thermohaline circulation. (Quadfasel et al., 1987; Broecker, 1991). Regime shifts in the Arctic can have profound effects on global climate, with a sea ice free Arctic Ocean being proposed to have provided the moisture supply for northern hemisphere glaciation during the Quaternary (Donn and Ewig, 1966).

1.2.2 The Svalbard Archipelago

The Svalbard Archipelago is a group of islands in the Arctic situated approximately half way between Norway and the north pole, between 78º-81ºN and 10º-35ºE. It consists of two large islands; Spitsbergen and Nordaustlandet, and several smaller islands; Barentsøya, Edgeøya, Kong Karls Land, Prins Karls Forland and Bjørnøya (Ingólfsson, 2004) (Fig. 2).

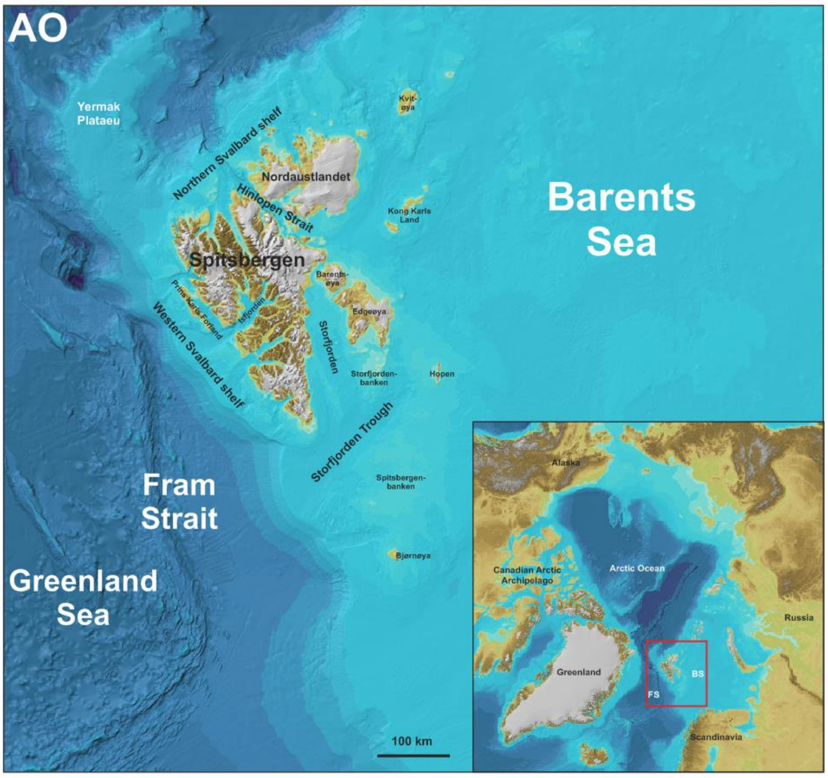

Figure 2: Map of the Svalbard Archipelago based on the International Bathymetric Chart of the Arctic Ocean (IBCAO) Version 3.0 (Jakobsson et al., 2012). AO = Arctic Ocean; BS = Barents Sea; FS = Fram Strait.

The Svalbard Archipelago is surrounded by the Fram Strait and Greenland Sea to the west, the Barents Sea to the east and the central Arctic Ocean to the north (Fig. 2). The landscape is predominantly mountainous cut by large ice caps, glaciers and fjords. The glaciers are either valley glaciers terminating on land or tidewater glaciers that terminate in the fjords (Ingólfsson, 2004).

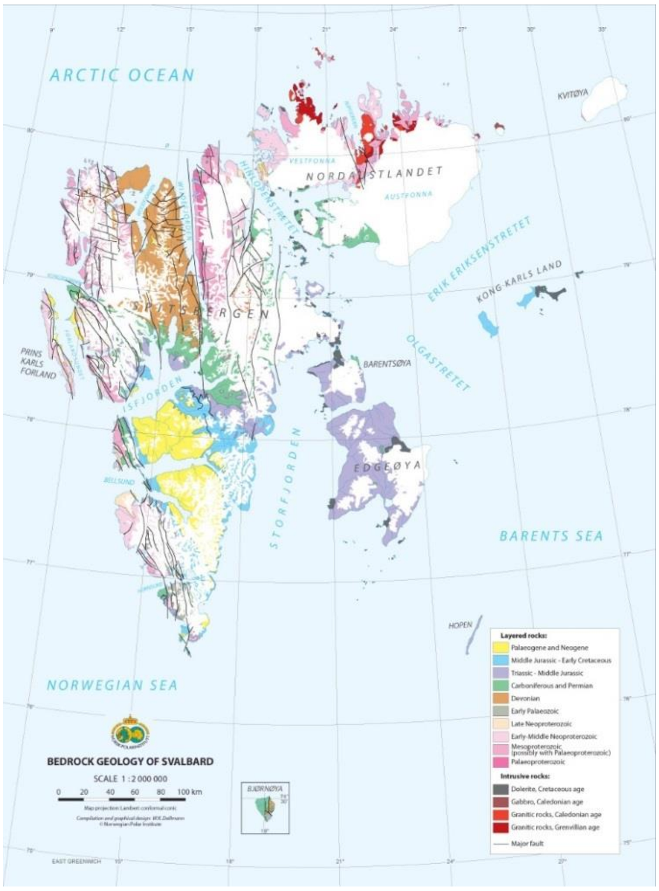

Figure 3: Map of the bedrock geology of the Svalbard Archipelago (Norwegian Polar Institute)

Svalbard is a geologically old and diverse region that has undergone many tectonic and sedimentary processes. The geology of Svalbard is a mosaic of various old formations (Fig.. 3), some dating back to the Precambrian (~600 My) when it was situated close to the South Pole, through to relatively young Tertiary (~60 My) coal deposits from when Svalbard was a shallow marine environment. The Quaternary (~2.8 My) on Svalbard was dominated by repeated glaciations which has shaped the landscape that is observed today (Ingólfsson, 2004).

1.2.3 Glacial history of Svalbard and the Barents Sea

The Svalbard and the Barents Sea region has undergone repeated glaciations during the Quaternary (Ingólfsson, 2004). Evidence suggests that the onset of glaciation on the landmasses occurred in the Pliocene-Pleistocene (~3.5-2.4 My) and expanded during the early Pleistocene (2.6-1 My) (Knies et al., 2009; Laberg et al., 2010). Large ice shelves are suggested to have extended onto the continental shelves surrounding Svalbard by ~1.6 My (Sejrup et al., 2005; Knies et al., 2009).

The advection of Atlantic Water into the Arctic during the last glacial period is proposed to have promoted seasonally ice-free conditions in the Fram Strait, and provided a source of moisture for the growth of the Svalbard-Barents Sea Ice Sheet (SBIS) (Hebbeln et al., 1994).

Terrestrial (e.g., Landvik et al., 1995) and marine evidence supports the theory of a marine-based ice shelf extending out to the shelf break on the western Svalbard margin at c. 21,400 cal. years (e.g., Elverhøi et al., 1995; Landvik et al., 1998; Jessen et al., 2010).

Palaeoreconstructions have shown that the SBIS covered much of the Barents Sea, northern Svalbard and western Svalbard margin during the Last Glacial Maximum (LGM) (e.g., Elverhøi et al., 1995; Landvik et al., 1998; Jessen et al., 2010). This is reflected in the distribution of well-preserved glaciomarine sediments and submarine landform assemblages in this region (Ottesen and Dowdeswell, 2009; Ingólfsson and Landvik, 2013).

The seafloor morphology reveals that deposition was characterised by dynamic ice-sheet behaviour. High-resolution studies have confirmed that fast-flowing ice streams drained the ice-sheets through the deep fjords and cross-shelf troughs along the continental shelves surrounding Svalbard (Fig. 4) The fast-flowing ice streams were divided by less-active ice, known as inter-ice stream areas (Landvik et al., 2005; Ottesen and Dowdeswell, 2009; Ingólfsson and Landvik, 2013).

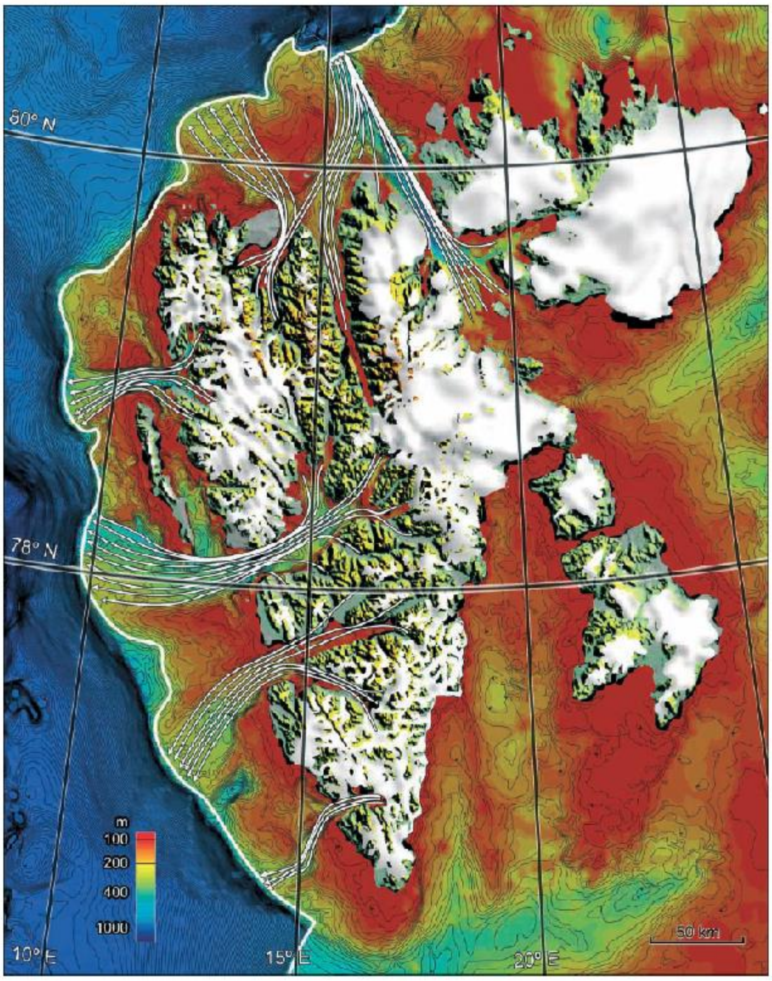

Figure 4: Reconstruction of past ice stream flow on the western and northern margin of the SBIS (Ottesen et al., 2007).

Numerous studies have reconstructed the Svalbard-Barents Sea Ice Sheet (SBIS) extent and the influence of the inflow of Atlantic Water during the last glaciation from marine archives (e.g., Hebbeln et al., 1994; Elverhøi et al., 1995; Anderson et al., 1996; Nørgaard-Pedersen et al; 2003; Landvik et al., 2005; Jessen et al., 2010). It is now the common consensus that the retreat of the SBIS occurred before c. 19,700 cal. years from the outer shelf on the north and west of Svalbard (Landvik et al., 2005; Ślubowska et al., 2005; Rasmussen et al., 2007; Ślubowska-Woldengen et al., 2008). Nevertheless, there are still discrepancies and unanswered questions regarding the dynamic behaviour during the LGM and subsequent demise of the SBIS, particularly in eastern Svalbard. The impacts of the advection of Atlantic

Water into this region and its influence on the climate, ice sheet activity, oceanography, and environment are still under debate (Ingólfsson and Landvik, 2013; Jakobsson et al., 2014).

1.2.4 Bølling-Allerød interstadials

The last glacial was succeeded by the Bølling and Allerød interstadials occurring c. 14,700-12,900 cal. years and are regarded as warmer periods from evidence in terrestrial and ice cores records (Daansgaard et al., 1984: De Jong, 1988). Around Svalbard the early Bølling interstadial was characterised by increased Atlantic Water flow and a large meltwater event following the retreat of the SBIS. The retreat was suggested to be rapid with high sedimentation from the turbid meltwater plumes, which have been identified as a wide-spread laminated layer of fine-grained sediments along the northern and western margins of Svalbard (Elverhøi et al., 1995; Lubinski et al., 2001; Nørgaard-Pedersen et al; 2003; Jessen et al., 2010).

1.2.5 Younger Dryas stadial

The Younger Dryas stadial was a cold period that occurred between c. 12,900-11,700 cal. years and is documented to have been initiated by the drainage of the proglacial Lake Agassiz from the Laurentide Ice Sheet. This catastrophic event suppled of large volumes of fresh meltwater into the north Atlantic is suggested to have suppressed the AMOC and caused subsequent weakening of Atlantic Water flow north into the Arctic. The meltwater formed a low salinity surface layer and the reduction of heat from the Atlantic Water may have permitted sea ice to form as far south as the southern British Isles (Kennett and Shackleton, 1975; Broecker et al., 1989; Broecker, 2006, a; Broecker, 2006, b). Evidence of the Younger Dryas is present in ice cores, and marine records around Svalbard as a rapid and short-term cold event of reduced Atlantic Water inflow and dominance of polar waters (Stuiver and Groots, 2000; Rasmussen et al., 2007; Ślubowska-Woldengen et al., 2007).

1.2.6 Holocene

The Holocene is an interglacial period that is divided into the early-, mid-, and late-Holocene. The early Holocene is documented to have been a warm period termed the Holocene Climatic Optimum, with warmer atmospheric temperatures compared to the 20th century (Kaufman et al., 2004). The HCO was driven by high summer insolation permitting a strong inflow of Atlantic Water into the Arctic, leading to the northward movement of the Arctic Front and reduction of sea ice (Koç et al., 1993; Kaufman et al., 2004; Jessen et al., 2010). Around Svalbard and in the Barents Sea the HCO is suggested to have occurred c. 11-7.5 Ky ago (Hald et al., 2004; Ślubowska et al., 2005; Rasmussen et al., 2007; Ślubowska-Woldengen et al., 2007; 2008). The presence of *Mytilus edulis* around Svalbard between c. 9500-3500 cal. years indicates that water temperatures were higher than that of today (Salvigsen et al., 1992; Berge et al., 2006).

The presence of strong Atlantic Water inflow is suggested to persist into the mid-Holocene with little glacial activity being documented on Svalbard (Elverhøi et al., 1995; Svendsen and Mangerud, 1997; Ślubowska-Woldengen et al., 2008).

The late Holocene climate shifts between short-term warm and cold phases. Evidence for glacial fluctuations during the late Holocene has been presented, with a glacial advance being documented c. 4400-1000 cal. years in Linnédalen, on the west of Spitsbergen. The maximum extent of the advance occurred during the 13th and 14th centuries until the end of the Little Ice Age in the 19th century. This coincides with evidence of increased glacial activity documented in Billefjorden in the late Holocene (Svendsen and Mangerud, 1997).

2. Study area

2.1 Oceanographic and environmental setting

Storfjorden is a sound located in the south eastern sector of the Svalbard Archipelago, situated between the islands of Spitsbergen to the west, Edgeøya and Barentsøya to the east (Fig. 5). The passages of Heleysundet and Freemansundet connect the head of Storfjorden to the Barents Sea in the northeast. Storfjorden is composed of a ~190 m deep inner basin bound by shallow, 40 m deep shelves to the north and east. A 115 m deep submarine sill separates the mouth of the fjord from the Storfjorden Trough (Storfjordrenna) in the southwest and Storfjordenbanken in the southeast (Fig. 5).

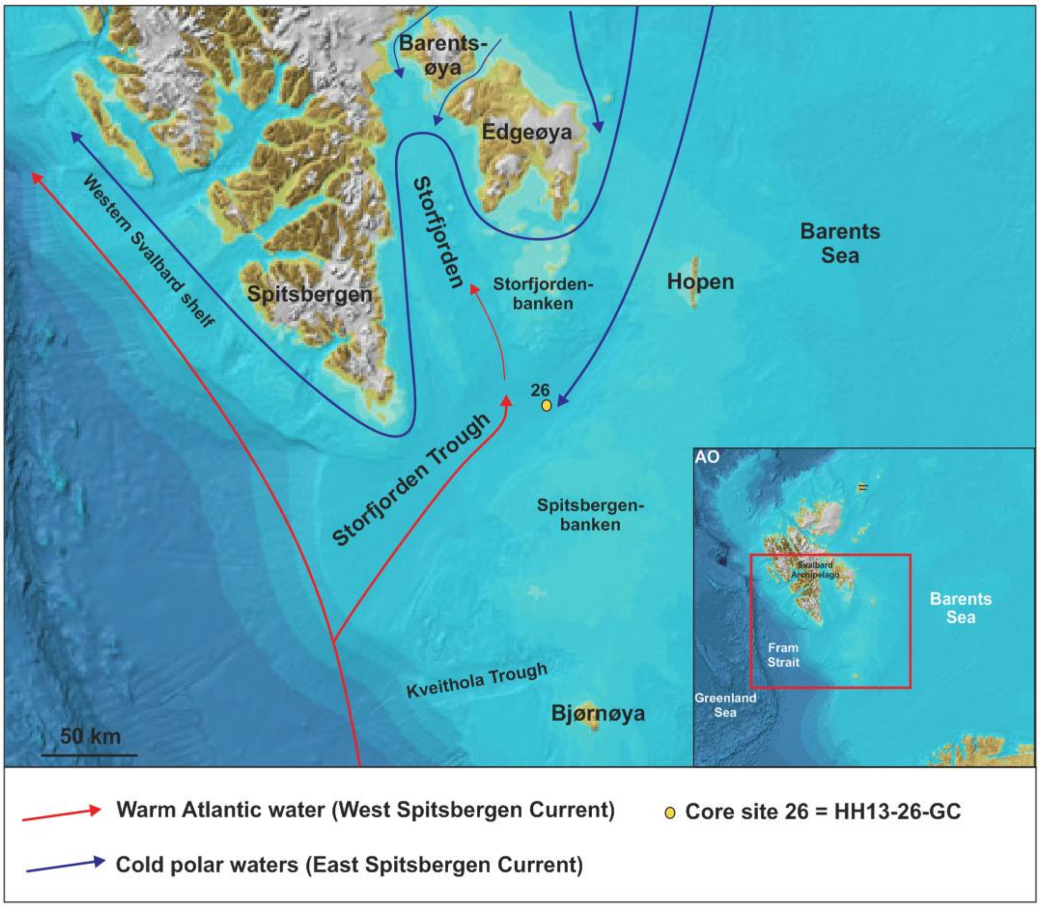

Figure 5: Map of Svalbard based on the International Bathymetric Chart of the Arctic Ocean (IBCAO) Version 3.0 (Jakobsson et al., 2012) with the core location of HH13-26-GC in the Storfjorden Trough marked. AO = Arctic Ocean.

The Storfjorden Trough is a between 150-420 m deep and extends 254 km westwards from the mouth of the fjord to the Barents Sea shelf break (Fig. 5). The trough was formed from glacial erosion by a fast-flowing ice stream of the SBIS, identified through various streamlined landforms that terminate at the Storfjorden Fan at the shelf edge (Laberg and Vorren, 1996; Dowdeswell et al., 1996). It has been proposed that the palaeo-ice flow was dynamic and that three sub-ice streams drained within the Storfjorden Trough (Pedrosa et al., 2011).

The present day oceanographic regime is dominated by two water masses Arctic water and Atlantic Water. The cold (<0.0 ºC), fresh (34.3-34.8) Arctic water enters Storfjorden through the passages in the northeast, and the Storfjorden Trough from the southeast near Edgeøya by the East Spitsbergen Current flowing from the Arctic Ocean (Loeng, 1991; Skogseth et al., 2005) (Fig. 5). It is transported along the coast of eastern Spitsbergen, eventually flowing westward around Sørkapp, at the southern tip of Spitsbergen as the Sørkappstrømmen coastal current (Sjøkartverk, 1990; Skogseth et al., 2005).

The North Atlantic Current flows as a surface current along the western Svalbard shelf where it loses heat as it is transported northwards to the Arctic, where it sinks and circulates as a subsurface layer. The surface flow of Atlantic Water branches and is topographically steered eastward transporting warm (>3 ºC), saline (>34.9) water into the Storfjorden Trough (Fig. 5) in a cyclonic style (Schauer, 1995; Loeng, 1991; Skogseth et al., 2005). This Atlantic Water is cooled, submerged beneath the various cold, local surface waters and is modified into Transformed Atlantic Water, which is still relatively warm (>0 ºC) and saline (>34.8). The Atlantic Water is navigated along the southern margin of the Storfjorden Trough, before it is deflected to the left following the topography due to the Coriolis Force caused by the rotation of the earth (Skogseth et al., 2005) (Fig. 5).

The boundary between the Arctic water and Atlantic Water is known as the Arctic Front and is located along the slope of the Storfjorden Trough (Loeng, 1991). The Arctic water and Atlantic Water are modified through mixing processes with each other and fresh water from melted sea ice, glaciers and river runoff, and heat exchange with the atmosphere to form locally produced Polar Front Water (Loeng, 1991; Skogseth et al., 2005). A list of the main water masses and locally formed water masses is given in Table 1.

Brines are produced through persistent sea ice formation that occurs in the inner basin of Storfjorden during the winter months, which is promoted by wind driven polynya activity. The dense, brine-enriched water fills up the basin and under specific hydrographic conditions it flows over the sill and is transported along Storfjorden Trough to the outer shelf (Quadfasel et al., 1988; Haarpaintner et al., 2001; Skogseth et al., 2005).

Table 1: List of the main water masses and locally formed water masses modified from Skogseth et al., 2005.

Water Mass	**Water mass characteristics**	
	Temperature (°C)	**Salinity**
Main water masses		
Atlantic Water	>3.0	>34.5
Arctic water	<0.0	34.3-34.8
Locally formed water masses		
Melt water	>0.0	34.2
Polar front water	-0.5 to 2.0	34.8-35.0
East Spitsbergen water	-1.0 to 0.5	34.8-34.9
Brine-enriched shelf water	<-1.5	>34.8
Storfjorden surface water	1.0 to 3.0	<34.4
Transformed Atlantic Water	>0.0	>34.8

3. Methods

3.1 Core recovery

The studied sediment core was acquired during an educational cruise with the R/V Helmer Hanssen in September 2013 as part of the AG211 Arctic Marine Geology course with The University Centre in Svalbard (UNIS). The location of the sediment core was selected based on the results of multibeam and acoustic surveys.

A gravity corer was deployed to recover the 283-cm-long core HH13-26-GC hereafter, HH13-26, from a prominent sediment lobe in Storfjorden at a water depth of 236 m (table 2).

The gravity corer (GC) consists of a 6 m-long steel barrel with a 1600 kg weight at the top. A plastic liner was inserted inside the barrel and was secured with a core cutter and core catcher at the base. The gravity corer was deployed from the vessel and reaches the seafloor due to the weight on top of the device. The core cutter penetrates the sediments and the core catcher encloses them at the base, preventing them from falling out on the up-cast of the corer.

Once on board the plastic liner containing the sediments was removed from the steel barrel of the coring device. The core was measured and divided into 1 m-long sections, labelled, cut and closed with plastic caps secured on the ends. The core sections were placed into cold storage (4^{o}C) while on board the ship and then at UNIS until they were opened in 2015.

Table 2: Location (Fig. 5), water depth and length of studied core HH13-26-GC.

Location	**Water depth**	**Core length**
76:21.55’N 20:07.34’E	236 m	283 cm

3.2 Geophysical data

3.2.1 Multibeam bathymetric data

Seafloor mapping data were collected using a hull mounted (HM) Kongsberg Maritime EM 300 multibeam echo sounder, yielding a high-resolution bathymetric image of the seafloor morphology. Sound-velocity profiles of the water column were obtained using the Seabird Inc. CTD probe. The multibeam image was processed and the submarine landforms were described and interpreted.

3.2.2 SIMRAD echo sounder

A SIMRAD ER60 single beamed echo sounder (18 kHz and 38 kHz) was used to obtain additional information on the acoustic properties of the water column. These data are commonly used in high-resolution investigations of the water column, such as for fisheries and mapping of natural seabed gas seeps.

3.2.3 Acoustic sub-bottom profile (Chirp) data

An EdgeTech 3300-HM sub-bottom profiler (Chirp) has a chirp frequency range of 2-16 kHz, to provide information on the structure of the sediments based on their acoustic characteristics. The multibeam, singlebeam and sub-bottom systems were running continuously during the survey.

The sub-bottom profile images were uploaded into the Discovery programme and the acoustic characteristics of the sediments were described and interpreted.

3.3 Water column properties

A Seabird 911 Plus CTD was used to study the properties of the water column, measuring conductivity (salinity), temperature, fluorescence (productivity) and oxygen content during down and up-casts of a station close to the coring site (table 2). The data gathered from the

CTD bins are used to characterise the present-day oceanography and aids with locating oceanographic features such as the Arctic Front or the presence of brines in bottom waters. The sound-velocity of the water is calculated from CTD data and is used to process the multibeam echo sounder data.

Table 2: Location and water depth of the CTD station.

CTD station	Latitude	Longitude	Water Depth
HH13-28	76:20.119'N	19:45.739'E	244 m

3.4 Laboratory work

3.4.1 Magnetic susceptibility (loop sensor)

3.4.1.1 Principle

A magnetic field is applied to the sediment core as it is passed through the loop sensor and the amount the sediment is magnetised is measured through changes in the frequency. If the sediment has a high ferromagnetic content the magnetic susceptibility (MS) reading will be positive whereas negative readings are given by diamagnetic material which reduce the magnetic field (GeoTek website). The loop sensor is specialised to be used in the field or on board a ship due to the minor influence of low temperature induced drift (Bartington manual).

3.4.1.2 Procedure

The core sections were passed through a Bartington MS2C loop sensor providing down-core profiles of magnetic susceptibility (MS) at 2 cm intervals. The sensor gives volume MS measurements of the sediment within the plastic core liner. The sections were taken out of cold storage (24 hours) to allow them to adjust to room temperature as the MS instrument is affected by temperature fluctuations.

The instrument was placed in a selected site in the Geology Laboratory at UNIS with stable temperature and all items that could cause electromagnetic interference were removed. Prior to taking measurements the loop sensor was switched on for 5 minutes settling time and was calibrated as recommended in the Bartington MS2 Manual.

Prior to lithological analysis the MS loop and point sensor data can be used to identify changes in lithology usually linked to provenance shifts and has been used as a stratigraphic tool to identify key events in the sedimentary record in particular on the Western Svalbard Slope (Jessen et al., 2010).

3.4.2 Sedimentology

The cores were split in half length ways using a band saw into archive and working halves. The archive sections were wrapped in plastic and placed into cold storage (4^{o}C) at UNIS. The working sections were photographed with a Panasonic Lumix DMC-XS1 digital camera, cleaned using a flexible plastic slide (perpendicular to the direction of deposition), photographed again, visually logged and described, taking note of colour changes (referring to the Munsell Colour Chart), sediment grain size, texture, contacts, features (i.e. clasts, shells) and structures. Bivalve shells were collected for radiocarbon dating and photographs were taken. Larger clasts that were visible on the core surface (>2 cm) were sampled, cleaned, photographed and placed into labelled plastic bags.

3.4.3 Magnetic susceptibility (point sensor)

A handheld Bartington MS2E surface scanning point sensor was used to measure the magnetic susceptibility at 1 cm intervals along the flat surface to obtain a MS down-core profile. The same protocols as used with the loop sensor were used with the point sensor such as; core temperature acclimatisation, the removal of metallic items, calibration and instrument settling time. The point sensor has a higher resolution due to the smaller sensor element than the loop sensor, but both instruments are often used in combination as the point sensor provides a higher spatial resolution MS record (Bartington manual; GeoTek website).

The unusually large peaks caused the presence of large clasts, and measurements obtained from the core ends were removed. The MS was used in combination with the lithological descriptions to gain an insight into grain size and sediment composition changes.

3.4.4 Shear strength

A device from Geonor was used to test the undrained shear strength of the sediments at 1 cm intervals. The shear strength was measured to give information on parameters such as sediment compaction and water content. Fall cones with various weights were used to measure the penetration of the cone into the sediment. For each interval the sediment core was placed under the magnet holder of the apparatus with the tip touching the sediment surface. The cone was released from the magnet holder and the depth of penetration measured in millimetres (mm) and was subsequently converted into a pressure measurement kilopascals (kPa) from the tables given in the Geonor manual (Geonor manual).

3.4.5 X-radiographs

3.4.5.1 Principle

The X-radiograph projects radiation (X-rays) towards the core and the amount that is absorbed by the surface is dependent on the density of the sediments. The X-radiograph images display the different density properties of the sediment structures in negative polarity (i.e. lighter shades are higher in density than darker shades) or positive polarity whereby density is displayed opposite to negative polarity. This is a non-destructive method of identifying clasts, shells and internal sedimentary structures such as laminations or lithological changes internally.

3.4.5.2 Procedure

The core sections of the working half were packaged and transported to Tromsø, Norway for the taking of X-radiographs and freeze drying of samples in the laboratory at the Department of Geology, University of Tromsø, Norway.

The internal structure of the sediments was investigated by passing the core sections through a GeoTek X-radiograph machine with an imaging interval of 20 mm that is processed into one image.

The X-radiographs for HH13-26 were best presented by inverting the image to negative polarity in the GeoTek Quick View programme. The images were processed by using the Virtual Compensator to smooth out the unevenness of the core surface and the contrast within the images were edited by adjusted from the histogram of intensity to best represent the contents of the core. The X-radiographs were used in combination with the lithological description and grain size analysis, and were digitised into a composite log in the CorelDRAW X8 illustrating programme.

3.4.6 Sediment sample preparation

Sediment samples were taken in 1 cm thick slices for the entire core length, placed into labelled plastic bags, wet weighed and stored in the laboratory freezer (12 hours; -20 ºC). During sampling bivalve shells were collected for radiocarbon dating and large clasts (>2 cm) were removed, cleaned and photographed.

3.4.7 Freeze drying

Freeze drying is a process whereby a vacuum is created and the water within the frozen sediments is vaporised and removed. This aids with the sieving process and foraminifera preservation within the samples (Rasmussen pers. comm. 2014). The frozen sediment samples were placed onto frozen metal plates and inserted into a Christ Alpha 1-4 freeze drier (-45 ºC; 48 hours). The samples were removed from the freeze drier and were weighed to measure the dry weight of the sediments. The wet weight and dry weight measurements were used to calculate the water content within the sediments.

3.4.8 Sieving

The sediment samples were transported to UNIS for further analysis. The sample resolution used was selected at 4 cm intervals down-core to provide a high-resolution dataset for interpretation in this study. The freeze dried samples were wet sieved to separate them into desired the grain sizes in mesh sizes of 63 µm, 100 µm, 500 µm and 1000 µm. The residues of each grain size fraction were washed onto filter papers using water and placed into an oven to dry (40ºC; 12 hours). The weight of each grain size fraction was determined by placing them into a metal dish of a known weight (22.0243 g) using a medium-sized paint brush and weighing them on Mettler Toledo XS 204 scales, and placing them into labelled glass vials.

3.4.9 Grain size analysis

The water content (% water) was calculated as follows:

$$\%\ \text{water content} = ((\text{wet weight} - \text{dry weight}) / \text{wet weight}) \times 100$$

The grain size distribution (>63 µm; 100-500 µm; 0.5-1 mm; >1 mm) for each sample is calculated as a percentage of the total dry weight sediment.

3.4.10 Ice-rafted debris

The ice-rafted debris (IRD) content of each sample was investigated by evenly distributing the 0.5-1 mm and >1 mm size fractions of each sample on a squared picking tray and counting the number of mineral grains under a light microscope. For the >1 mm size fraction the whole sample was counted. The bulk IRD count was used to calculate the number of IRD per gram of dry weight sediment.

The entire sample was counted if there were <300 grains in the 0.5-1 mm fraction, however in many samples the IRD was extremely abundant (>500 grains) therefore at least 300 grains were counted for quantitative analysis and the number of IRD per gram of dry weight sediment was calculated.

Authigenic material such as gypsum or pyrite crystals and clay aggregates were not included in the bulk count. It was noted if there was authigenic material, shell fragments or microfossils, such as large foraminifera were present.

3.4.11 Foraminifera analysis

The 100-500 µm fraction was used to investigate the benthic foraminifera content (calcareous and agglutinated). The samples were relatively large therefore only a portion of each sample was evenly distributed over a picking tray with 45 identical squares and placed under a Leica MZ16 light microscope for analysis. A number >300 benthic foraminifera were picked, counted, identified to species level from randomly selected squares on the tray and placed onto a slide with numbered boxes for later referral if needed.

Identification of the most dominant species was facilitated by scanning electron micrographs of benthic foraminiferal species from Storfjorden found in Rasmussen and Thomsen (2014). *Buccella frigida* and *Buccella tenerrima* were not differentiated and are labelled *Buccella* spp. *Cassidulina neoteretis* and *Islandiella norcrossi* are often labelled *Cassidulina/Islandiella* spp. as many specimens were difficult to distinguish due to poor preservation. Some species were grouped as indeterminate as there was a lack of features that could allow an accurate identification.

Many samples had partial foraminifera tests, half tests were classed as one specimen if they were easily identified and if less than half a test was observed it was classed as half a specimen, only if the first chamber was observed and identified.

Planktonic species were counted but specimens were in low numbers for many of the samples. If over 100 specimens were counted, they were also identified and samples with less than 50 specimens will be omitted from quantification as the error would be too large with such a low amount.

The sediment residue that was not used for foraminifera analysis was weighed to calculate the weight of sediment used to count the foraminifera and subsequently calculate the number of foraminifera per gram. If there weren't many specimens in a sample more than one tray was counted to identify >300 specimens.

The number of calcareous and planktonic foraminifera per sample and the total concentration of benthic foraminifera were calculated (number per gram dry weight sediment). The percentage of agglutinated and calcareous benthic foraminifera for each sample was also calculated relative to total foraminifera. The relative abundance (percentage) of the most dominant species was calculated relative to the total number of benthic forms. Considering the latter only the samples with more than 50 specimens were included in this calculation, to reduce the risk error and misrepresentation.

During foraminiferal analysis the samples in the upper 1 m of the core were noted as being very organic-rich therefore they were re-sieved to be sure all of the smaller (<100 µm) organic grain sizes were removed.

3.4.12 Preservation of foraminifera

Fragments of the calcareous foraminifera tests were counted in the squares that were used to count and identify the foraminifera. The number of calcareous fragments per gram dry weight sediment was calculated and the data was used to calculate the percentage of fragmentation of calcareous specimens in each sample relative to the concentration of whole specimens. The percentage fragmentation will be used to give an insight into the preservation state of the foraminifera.

Percentage fragmentation calculation:

Number fragments g^{-1} / (Number fragments g^{-1} + Number benthic foraminifera g^{-1}) x 100

3.4.13 Radiocarbon dating

3.4.13.1 Principle

Radiocarbon was discovered by Libby in 1949 and is currently the most widely used radiometric dating technique. Carbon has three isotopes ^{14}C, ^{12}C and ^{13}C, the latter two are naturally occurring in the environment and are stable, whereas ^{14}C is unstable (Walker, 2005). Carbon-14 is produced in the upper atmosphere through the nuclear reaction between cosmic rays and nitrogen which incorporate oxygen to yield a form of carbon dioxide; $^{14}CO_2$ (Faure and Mensing, 2005; Walker, 2005). ^{14}C is radioactive and decays through time at a known rate of 1% per 83 years, it decays exponentially therefore the half-life for a ^{14}C atom is 5730 years and the rate can be measured up to eight half-lives (~45,000 years) (Walker, 2005).

$^{14}CO_2$ is a component of the global carbon cycle and is absorbed through photosynthesis by plants that are subsequently consumed by animals. Most ^{14}C is absorbed through the oceans as dissolved carbonate (CO_3) which is assimilated by marine organisms such as foraminifera and molluscs to construct their exoskeletons through the precipitation of calcium carbonate (CaCO3) (Walker, 2005). ^{14}C in biogenic material is in a steady-state equilibrium with the atmosphere, as it decays it is constantly replaced by the atmosphere. When a marine organism dies it ceases to incorporate $CaCO_3$ from the system, therefore by knowing the rate of decay of ^{14}C a calendar age of the fossil material can be derived (Faure and Mensing, 2005; Walker, 2005).

There are two methods to measure ^{14}C in samples, beta counting and accelerator mass spectrometry (AMS), the latter approach was used in this study. Mass spectrometers are used to identify the atoms in elements based on their different atomic weights (Lowe and Walker, 2015). AMS is based upon using particle accelerators as mass spectrometers to count the relative number of ^{14}C atoms in the sample that is being dated. The lighter and heavier particles are detected in the mass spectrometer as they are passed through a magnetic field and are deflected from a straight path. The degree to which they are deflected is in proportion to their atomic weight, therefore lighter particles have a larger deflection from the straight path (Linick et al., 1989; Lowe and Walker, 2015). ^{14}C and ^{14}N have a similar atomic weight therefore their particles must travel at high speeds from large charge differences to distinguish between the two isotopes (Lowe and Walker, 2015). Using this method AMS can detect minor quantities of ^{14}C atoms in a sample. The age of the sample is determined by the comparison of the ratio between the residual ^{14}C, and ^{12}C and ^{13}C to a standard of known ^{14}C content (Walker, 2005).

3.4.13.2 Assumptions and sources of error

The radiocarbon dating method is based on the following set of assumptions which are potentially sources of error within the technique (Walker, 2005):

. The ^{14}C and ^{13}C ratio is virtually constant through time in each component of the global carbon reservoir.

. Globally ^{14}C entirely mixes rapidly through each individual reservoir.

. Apart from the decay of ^{14}C within the organism, the ratios between the other carbon isotopes haven’t changed.

. The half-life of ^{14}C is known to an accurate and acceptable level of precision.

. The measurement of natural levels of ^{14}C is to acceptable levels of accuracy and precision.

The general consensus is that the half-life and the natural levels of ^{14}C can be accurately measured. However, due to the uncertainties with the other three assumptions there potentially large sources of error within the accuracy of this dating method that must be considered (Faure & Mensing, 2005; Walker, 2005):

. **Contamination of the sample** with younger or older carbon could yield an inaccurate date. This could occur in the marine environment through mixing of older and younger sediments through mass wasting events such as turbidites and gravity flows, or through disturbance during the coring process (Walker, 2005).

. **Isotopic fractionation**, for example, the preferential absorption of an isotopic form of carbon (e.g. ^{12}C) leading to enrichment. In the marine environment ocean water is enriched in the heaviest isotope of carbon (^{14}C). The enrichment of ^{14}C in ocean water causes the organisms that assimilate it into their exoskeletons to have greater ^{14}C activity, yielding a younger ^{14}C age (Ravelo and Hillaire-Marcel, 2007).

. **Long-term variations in ^{14}C production** could occur through changes in the cosmic ray flux from variations in solar activity or the earth's geomagnetic field. Anthropogenic effects such as the increased burning of fossil fuels has released vast amount of ^{12}C into the atmosphere, diluting the levels of ^{14}C present. However, large-scale nuclear weapons testing in the 1950's has almost doubled the amount of atmospheric ^{14}C, counteracting the effect of Industrial Revolution. Due to the major impact of these variations on radiocarbon dating it is important to calibrate radiocarbon ages into calendar ages using various calibration programmes (Faure & Mensing, 2005; Walker, 2005).

. **Marine reservoir effects** are due to the variations in the ages of seawater globally. The replenishment of ^{14}C as dissolved carbonate in seawater is through the gaseous exchange of CO_2 between the atmosphere and ocean surface. The slow mixing processes that occur in surface waters gives a reservoir age of approximately 400 years for near surface waters (Stuiver et al., 2005).

Thermohaline circulation causes the surface water masses to eventually cool and sink at high latitudes to form the intermediate and deep layers. These deep waters are isolated from this atmospheric exchange and will decay without any replenishment of ^{14}C, adding to the reservoir age compared to the surface water (Walker, 2005).

The different water masses will have an apparent age which is dependent on their location and depth. The isotopic properties of the water masses are incorporated into the exoskeleton of the marine organisms and the residence times in the deep ocean can be up to thousands of years (Walker, 2005).

The dating of any material from the marine environment must be calibrated for the apparent reservoir age of the seawater.

3.4.13.3 AMS radiocarbon dating

Radiocarbon ages of three samples containing bivalve shells (Fig. 6) were selected from depths representing a wide age distribution of the core (table 3). The shells that were sent for radiocarbon dating were well-preserved and they did not appear to have been re-deposited (Fig. 6).

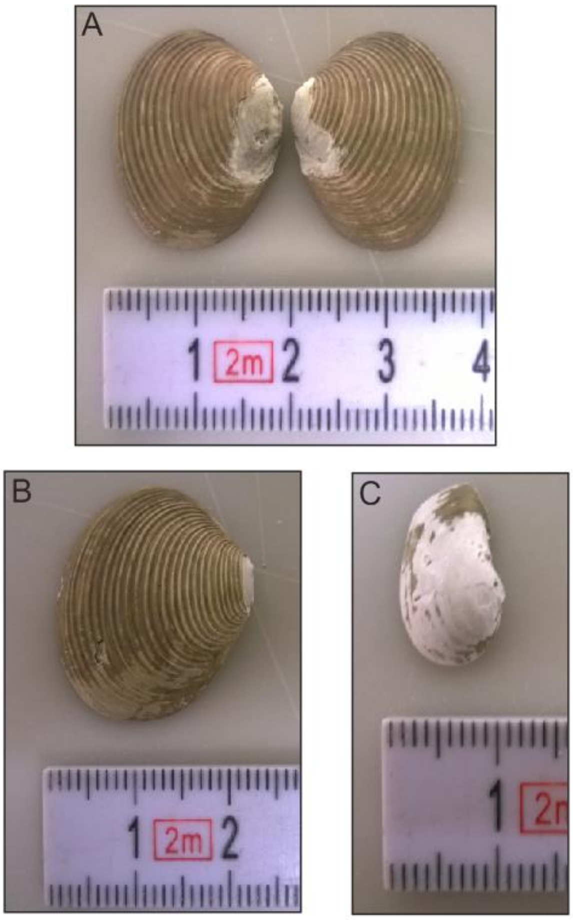

Figure 6: Photographs of bivalve shells set for radiocarbon dating.

A sample containing calcareous benthic foraminifera in a good preservation condition (>1500 specimens) was also sent and was selected due to a faunal change observed at this depth.

Table 3: Details of samples sent for radiocarbon dating; type, depth and weight for studied core HH13-26-GC.

Sample number	Sample type	Depth (cm)	Weight (mg)
HH13-26-GCA	Foraminifera	141-142	7.5
HH13-26-GCB	Bivalve	48-50	1220
HH13-26-GCC	Bivalve	95-97	499.2
HH13-26-GCD	Bivalve	162-163	860

The radiocarbon ages were determined using AMS at 14CHRONO Centre, Queens University Belfast.

3.4.13.4 Calibration

To correct the radiocarbon ages derived from the AMS dating for the marine reservoir effect and other sources of error the dates were calibrated into calendar years before present, hereafter cal. years, using the CALIB 7.0.4 program. The programme is a calibration dataset developed based on dendrochronological records for Holocene records and other independently ^{14}C dated samples e.g., corals to calculate the probability distribution of the samples true age (Stuiver and Reimer, 1993; Stuiver et al., 2005).

Marine13 calibration curve was selected to correct for the global reservoir effect in marine samples of approximately 400 years. The regional difference in the reservoir age of different water masses compared to the global model was corrected by applying a ΔR value (Stuiver et al., 2005). The ΔR in the Svalbard region of 150 ± 24 years was applied and has been used to correct for the local effects on the reservoir age around western Svalbard (Mangerud et al., 2006; Łącka et al., 2015). There are no data for reservoir ages in Storfjorden or east of Svalbard which is under the influence of the cold, East Spitsbergen Current, so it should be noted the reservoir age may differ in this region (Łącka et al., 2015).

The calendar ages were calculated as distribution within a 2-sigma (2 σ) range as it gives a higher probability of the correct age. The two ages within the 2 σ range were added together and divided by two to get the average calendar age which will be used in this study.

3.4.14 Age model and accumulation rates

The age model for core HH13-26 was determined by assuming that the sedimentation rate was constant between the calendar ages derived from the ^{14}C dated samples. The linear sedimentation rate (cm ky^{-1}) was calculated for the intervals between the dates and approximate calendar ages applied from 171-0 cm and is further described in the results section.

The mass accumulation rate (MAR) is expressed as g cm^2 ky^{-1} was calculated from the dry bulk density (DBD) of the sediment samples. The MAR was applied to calculate the accumulation rate of the various grain size fractions expressed as g cm^2 ky^{-1}, and the IRD, benthic and planktonic foraminifera expressed as no. cm^2 ky^{-1}.

3.4.15 Stable isotopes

3.4.15.1 Principle

Pioneering studies have revealed the thermodynamic properties and fractionation processes that occur with stable isotopes, alongside the development of mass spectrometry which permitted the measurement of miniscule differences in isotopic composition in fossils (Urey, 1947; Nier, 1947). Fractionation is the change in the isotope ratio of an element within a compound and is primarily regulated by temperature and the difference in mass of the isotopes. There are three isotope fractionation pathways; equilibrium exchange, mass-dependent and kinetic reactions (Hoefs, 2009, a; Pearson, 2012). Heavier isotopes are more stable than lighter isotopes as their covalent bonds are stronger and they have weaker vibrational energies. The measurements of isotopes are presented as a ratio relative to a standard ratio. Isotopic ratios are expressed as a concentration quoted as delta notation (δ) in parts per thousand (‰) (Faure and Mensing, 2005; Pearson, 2012).

Stable isotopes are widely used as geochemical proxies in palaeo-environmental studies to reconstruct a range of palaeo-climatic and -oceanographic conditions from fossil foraminifera in marine sediment cores (e.g., Emiliani, 1955; Ravelo and Hillaire-Marcel, 2007). Foraminifera build their calcareous tests by incorporating elements from the ambient seawater and in doing so record a geochemical signature from the water chemistry within their exoskeletons (Katz et al., 2010). Analysis of oxygen and carbon isotopes from foraminifera has been fundamental to our understanding of palaeo-climate.

3.4.15.2 Oxygen isotopes

Oxygen is the most abundant element on earth and exists in three forms (^{16}O, ^{17}O, ^{18}O) of different mass and abundance (table 4) (Faure and Mensing, 2005; Hoefs, 2009, b).

Table 4: Abundance and mass of each oxygen isotope.

Isotope	Abundance	Mass
^{16}O	99.762%	15.994915 amu
^{17}O	0.038%	16.999131 amu
^{18}O	0.200%	17.999160 amu

^{18}O and ^{16}O have the greatest mass difference (table 4) and are more abundant therefore the ratio of oxygen isotopes within a sample ($^{18}O/^{16}O$) is expressed as positive or negative values of $\delta^{18}O$ relative to a standard (Ravelo and Hillaire-Marcel, 2007; Lowe and Walker, 2015), and is calculated as:

$$\delta^{18}O\text{sample} = 1000 \times (^{18}O/^{16}O\text{sample} - {}^{18}O/^{16}O\text{standard}) / {}^{18}O/^{16}O\text{standard}$$

The standard used for $\delta^{18}O_{\text{sea water}}$ is the Vienna Standard Mean Ocean Water (VSMOW) and the standard used for $\delta^{18}O$ values from carbonates in foraminifera is the Vienna PeeDee Belemnite (VPDB) (Ravelo and Hillaire-Marcel, 2007).

Fractionation of oxygen occurs between the liquid and vapour water molecule phases. ^{16}O evaporates from the sea surface more readily than ^{18}O as it is isotopically lighter. The ^{16}O rises into the atmosphere and is released as precipitation over the landmasses and transported back to the oceans through river runoff during interglacial periods or sequestered in ice sheets during glacial periods (Ravelo and Hillaire-Marcel, 2007; Katz et al., 2010). As evaporation is temperature dependent the amount of ^{16}O in glacial ice is much more pronounced at higher latitudes as the colder air masses are less capable of up-taking the heavier ^{18}O isotope (Lowe and Walker, 2015). Seawater during glacial periods is enriched by the heavier ^{18}O isotope as the lighter ^{16}O is locked up in the continental ice sheets (Katz et al., 2010). When the ice sheets melted the ^{16}O was released in vast quantities back in to the ocean.

As foraminifera secrete their calcium carbonate ($CaCO_3$) test within ambient seawater the oxygen isotope signature ($\delta^{18}O$) represents the isotopic composition of the seawater (δ_{sw}) and the temperature-dependent fractionation at the time of calcification (Katz et al., 2010). The factors that influence the $\delta^{18}O$ of the seawater are the continental ice volume which is linked to sea level and salinity (Ravelo and Hillaire-Marcel, 2007). Considering this, $\delta^{18}O$ from foraminifera tests can gain an insight into past ice sheet volume, linked to sea level and salinity, and bottom water temperature.

A global benthic oxygen isotope record has been derived for the entire Cenozoic based on foraminifera from deep-sea sediment cores. The marine record represents down-core oscillations between lower values of $\delta^{18}O$ during interglacial periods and higher values of $\delta^{18}O$ during glacial periods (Zachos et al., 2001; Lowe and Walker, 2015).

3.4.15.3 Oxygen isotope limitations

Oxygen isotope analysis has several limitations that affects the interpretation of the record and must be considered (Ravelo and Hillaire-Marcel, 2007; Lowe and Walker, 2015):

. **Biological vital effects** could cause some species to calcify in disequilibrium with the seawater, for example, species containing photosynthetic symbionts can encourage higher calcification rates and a depletion of $\delta^{18}O$. Therefore, certain species that do calcify in equilibrium with the seawater such as *Uvigerina senticosa* and *Globocassidulina subglobosa* are selected as they provide a more reliable record.

. **Temporal resolution** of the record can be short due to low sedimentation accumulation rates, especially in the deep sea. A sediment sample could span thousands of years leading to an average isotope value for this time interval.

. **Sediment mixing** through bioturbation or turbidity currents could distort the isotope record through reworking of the sediments.

. **Carbonate preservation** of the foraminifera tests can vary in certain regions and species with colder regions being more susceptible to dissolution. Well-preserved tests are desired for analysis to ensure an accurate record is obtained.

3.4.15.4 Carbon isotopes

Carbon is extremely abundant on earth and has two stable forms ^{12}C and ^{13}C (Faure and Mensing, 2005) (table 5).

Table 5: Abundance and mass of stable isotopes of carbon.

Isotope	Abundance	Mass
^{12}C	98.90%	12.000000 amu
^{13}C	1.10%	13.003355 amu

The earth's biosphere is built from carbon and climate is regulated by its abundance (Armstrong and Braiser, 2005). Fractionation of carbon predominantly occurs through chemical and biological processes as ^{13}C has a larger mass than ^{12}C (Lowe and Walker, 2015). The technique used to measure $\delta^{18}O$ yields a measurement of $\delta^{13}C$ which is the deviation of the $^{13}C/^{12}C$ sample ratio from a standard $^{13}C/^{12}C$ ratio (Katz et al., 2010), calculated by:

$$\delta^{13}C = 1000 \text{ x } (^{13}C/^{12}C\text{sample} - {}^{13}C/^{12}C\text{standard}) / {}^{13}C/^{12}C\text{standard}$$

The standard used for $\delta^{13}C$ values is the VPDB standard as with $\delta^{18}O$ values (Ravelo and Hillaire-Marcel, 2007).

Photosynthesis is the dominating fractionation method, biologically ^{12}C is preferentially absorbed during photosynthesis as it is isotopically lighter leading to much of the earth's biosphere having negative $\delta^{13}C$ values (Katz et al., 2010).

Carbon enters the ocean the gaseous exchange of CO_2 from the atmosphere and through riverine supply from the chemical weathering of continental rocks. Carbon is sequestered in carbonate rocks and organic carbon in sediments (Katz et al., 2010).

Measurements of $\delta^{13}C$ in the deep ocean are lower than in the surface ocean due to primary production causing the surface water mass to contain DIC enriched in $\delta^{13}C$, as the ^{12}C is preferentially taken up in biological processes. The ^{12}C is biologically pumped to the deep ocean when sinking organic matter rich in ^{12}C and lowers the $\delta^{13}C$ in the deep waters further (White. 2015).

Carbon from the seawater is assimilated into foraminifera while calcifying their tests in the same manner as with oxygen (Katz et al., 2010). $\delta^{13}C$ in foraminifera tests represents the carbon isotopic composition of the DIC in the surrounding seawater during calcification. The $\delta^{13}C$ content within the benthic foraminifera test can provide information on the surface ocean productivity. High surface productivity will yield low $\delta^{13}C$ values in benthic foraminifera as DIC enriched in ^{12}C is transported to the seafloor and assimilated into their tests (Ravelo and Hillaire-Marcel, 2007).

As previously mentioned the age of deep water can vary regionally and can be restricted from exchange with the surface for thousands of years. Ventilation of the deeper water masses through vertical mixing with the upper water masses supplies oxygen which aids with productivity (Lowe and Walker, 2015). Deep water masses have prominent $\delta^{13}C$ characteristics and measurements from benthic foraminifera can provide information of bottom water circulation and thus ventilation patterns. For example, Pacific Deep Water is considered old and has a low $\delta^{13}C$ value whereas Antarctic Bottom Water (AABW) is mixed with North Atlantic Bottom Water (NABW) which is young with a high $\delta^{13}C$ content (Kroopnick, 1980; White, 2015). Considering this, the two water masses contain a $\delta^{13}C$ signature and can be distinguished at the time of calcification by analysing the $\delta^{13}C$ from the benthic foraminifera in deep sea sediments (White, 2015; Ravelo and Hillaire-Marcel, 2007).

Carbon isotopes are used as a proxy to identify changes in content of CO_2 which is markedly reduced during glacial periods (Broecker, 1982). Shackleton (1977) first described the relationship between changes in $\delta^{13}C$ in foraminifera with changes in continental ice volume linked to the $\delta^{18}O$ record. During glacial phases $\delta^{13}C$ values are more negative compared to interglacial phases due to the decrease in terrestrial vegetation on the landmasses. The glacial effect on the $\delta^{13}C$ foraminiferal record must be corrected for the difference of 0.3-0.4 ‰ (Sigman and Boyle, 2000).

3.4.15.5 Carbon isotope limitations

Carbon isotope analysis has several limitations that affect the $\delta^{13}C$ record, listed below are the most important ones for marine studies:

. **Infaunal species** - many benthic foraminifera species are infaunal and record the $\delta^{13}C$ of the pore water during calcification. Pore water can be rather depleted in $\delta^{13}C$ due to the high rates of respiration of organic matter within the sediment column, which can lead to lower $\delta^{13}C$ values recorded compared with epifaunal species that recorded the $\delta^{13}C$ of the bottom water (Ravelo and Hillaire-Marcel, 2007).

. **Vital effects -** the foraminiferal $\delta^{13}C$ reflects the carbon isotopic composition of the DIC of seawater, but it does not calcify in isotopic equilibrium with the seawater. The calculated offsets of $\delta^{13}C$ for benthic foraminifera vary greatly depending on size, ontogenetic stage, calcification rates and temperature (Grossman, 1987; Ravelo and Hillaire-Marcel, 2007).

Considering the above limitations, $\delta^{13}C$ can still be used to speculate on multiple parameters such as ventilation of bottom waters and productivity as the $\delta^{13}C$ of DIC is not uniform throughout the world's oceans or constant over time (Ravelo and Hillaire-Marcel, 2007).

3.4.15.6 Stable isotope analysis

Stable isotopes of $\delta^{13}C$ and $\delta^{18}O$ were measured from samples from the upper 168 cm of the core containing calcareous benthic foraminifera. The entire sample was looked through to collect the desired species, *Cibicides lobatulus* as it is an epifaunal species that records the bottom water ventilation. If there were not enough well-preserved specimens of *C. lobatulus* to obtain a recommended minimum weight of 0.2 mg *C. reniforme* or *I. norcrossi* were collected with overlaps. These two species are shallow infaunal and record the pore water $\delta^{13}C$ and $\delta^{18}O$.

The foraminiferal species were picked based primarily on their preservation state and where possible, were of a similar size to minimise any error in the measurements, which was more difficult down-core. The *C. lobatulus* specimens were relatively large, a range between 3-10 specimens were picked. *C. reniforme* specimens were small, therefore at least 30-50 specimens were picked. The *I. norcrossi* specimens were quite large and 8-12 specimens were picked. The picked specimens were placed into labelled Eppendorf tubes and sent to Stockholm University for processing.

As some species of foraminifera do not calcify in equilibrium with the ambient seawater the $\delta^{18}O$ values for certain species must be corrected for vital effects (Duplessy et al., 1970). A correction factor of 0.64 ‰ was added to the $\delta^{18}O$ values for *C. lobatulus* (Duplessy et al., 2005). Vital effects were not corrected on either *C. reniforme* or *I. norcrossi* following other studies in the Svalbard region (Hald et al., 2004; Knudsen et al., 2004; Ślubowska-Woldengen et al., 2007; Klitgaard-Kristensen et al., 2013). Austin and Kroon (1996) state that *C. reniforme* calcifies in disequilibrium with an offset of 0.13 ‰. However, when this was applied to the $\delta^{18}O$ *C. reniforme* values there was a larger difference compared with the $\delta^{18}O$ values obtained from *C. lobatulus*, therefore the offset was not applied.

In this study the $\delta^{13}C$ and $\delta^{18}O$ records will be discussed with respect to water mass properties, ventilation and/or productivity and bottom water temperature. As the $\delta^{18}O$ record is from benthic foraminifera it is assumed that the salinity of the bottom water at the core location has not varied greatly over time (Lubinksi et al., 2001).

To reveal the temperature signals within the $\delta^{18}O$ record the effects of the changes in global ice volume were removed. The ice volume effects were calculating using the age model for the core HH13-26 and published changes in $\delta^{18}O_{water}$ over time linked to sea level changes caused by the fluctuating ice masses in Fairbanks (1989). The ice volume corrected $\delta^{18}O$ foraminiferal record was plotted on an inverse scale, the opposite to the $\delta^{18}O$ record obtained from ice cores.

The $\delta^{18}O$ values were converted into relative temperatures by linking the $\delta^{18}O$ from the foraminifera to the temperature during calcification and the $\delta^{18}O_{water}$ (Shackleton, 1974). The $\delta^{18}O_{water}$ is related to salinity, which is assumed to be relatively stable over time. The $\delta^{18}O_{water}$ at the core site HH13-26 was calculated using the $\delta^{18}O$ mixing line equation for outer fjord areas around Svalbard (MacLachlan et al., 2007):

$$\delta^{18}O_{water} = 0.43 \text{ x salinity} - 14.69$$

The bottom water salinity measurement obtained from the CTD data (35.10) was used in this calculation and yielded a value of 0.40 ‰, which is within the range of average $\delta^{18}O_{water}$ of 0-0.5 ‰ (Ravelo and Hillaire-Marcel, 2007).

The palaeotemperature equation that links $\delta^{18}O$ to temperature was inverted following Lubinski et al. (2001) to derive the relative temperature values from the $\delta^{18}O$ foraminiferal record:

$$\delta^{18}O_{foraminifera}\ (PDB) = (\delta^{18}O_{water}\ (SMOW) - 0.27) + ((-16.9 + temperature)/-4.0)$$

Where -0.27 ‰ is the conversion of SMOW to PDB standard (Hut, 1987), and 16.9 and -4.0 represent the upper and lower temperature domains.

To check the reliability of the calculated palaeotemperatures in this study, the $\delta^{18}O_{water}$ and a modern bottom water temperature (2 ºC) from the outer Kongsfjorden area from MacLachlan et al. (2007) was used to calculate a $\delta^{18}O_{foraminifera}$ value. The value yielded was considered to be realistic (3.86 ‰) and therefore the palaeotemperatures calculated in this study are used when interpreting the $\delta^{18}O$ record.

3.5 Processing and illustration of data

The data was entered into Microsoft excel and then plotted using the Grapher 7 programme and illustrated in CorelDRAW X8 programme.

4. Foraminifera

4.1 Background and ecology

Foraminifera are single-celled protists that contribute to the biomass of zoobenthos and zooplankton in the marine realm. The morphology of this group is characterised by a shell or ‘test’ with one or multiple chambers that are perforated with fine-pores, and features an opening or ‘aperture’ (Loeblich and Tappan, 1964; 1992; Tappan and Loeblich, 1988). The tests are built from calcium carbonate ($CaCO_3$) which is secreted either as calcite or aragonite, species adopting this method are known as calcareous species (Corliss, 1985). Other methods include the gathering of sediment particles carried out by agglutinated species, and the secretion of an organic substance known as tectin (Corliss, 1985; Tappan and Loeblich, 1988; Loeblich and Tappan, 1992). The growth of foraminifera is either continuous where the size of a single chamber is increased or by the episodic addition of a new chamber (Wynn Jones, 2014).

Foraminifera are ubiquitous throughout the marine environment and have various life strategies such as planktonic or benthic dwelling, the latter being either epifaunal or infaunal (Corliss, 1985). There have been over 38,000 fossil and living species identified dating back to the Cambrian-recent (Wynn Jones. 2014).

Identification of foraminifera is based on morphological features such as; wall structure, chamber arrangement, aperture shape and test composition (Loeblich and Tappan, 1964; 1992: Tappan and Loeblich, 1988). The distribution of foraminifera is dictated by their tolerance or preference to specific environmental conditions, for example, salinity, water depth, sedimentary environment or substrate, temperature, oxygen availability, geography, pH, $CaCO_3$ availability and oceanography (Hald and Korsun, 1997; Wynn Jones, 2014).

Foraminifera have been applied to various biostratigraphic and palaeo-studies as they are an abundant and diverse group. They provide an almost complete geological record as their tests are relatively well-preserved in marine sedimentary archives and record signals during calcification from the environment in which they inhabit (Hald and Korsun, 1997; Rasmussen and Thomsen, 2015). The study of foraminifera has proved invaluable in the understanding of modern and ancient marine environments as they can be used as indicators of salinity, water temperature, glacial and oceanographic conditions, productivity and oxygen level (e.g., Corliss. 1985).

Interpretation of foraminiferal records is based on quantitative techniques such as; relative and absolute abundance, diversity, dominance, equitability and isotope measurements, or more qualitative approaches such as; assemblage distribution and preservation state (Rasmussen pers. comm. 2014; Wynn and Jones. 2014).

The distribution of modern benthic foraminifera assemblages living in various environmental conditions from the fjords of Svalbard have been investigated and has provided an important analogue that can be applied to the interpretation of the palaeo-record of the Quaternary (Hald and Korsun, 1997). A number of palaeoenvironmental and palaeooceanographic reconstructions of the fjords of Svalbard have been achieved based on the comparison of the fossil foraminiferal record with the modern benthic distribution (e.g. Ślubowska et al., 2005; Rasmussen et al., 2007; Ślubowska-Woldengen et al., 2007; Skirbekk et al., 2010; Łącka et al., 2015; Rasmussen and Thomsen, 2015).

4.2 Foraminifera ecology

The ecological preferences of the most common benthic species identified in core HH13-26 is described below, with a focus on the typical environmental conditions and water mass characteristics in which each species thrives. This will aid in the interpretation of the palaeoenvironment and palaeooceanographic conditions that prevailed at that time. The planktonic species were in low quantities HH13-26 therefore their ecological preferences will only be briefly discussed.

4.2.1 Ecology of calcareous benthic species

4.2.1.1 *Cassidulina reniforme* (Nørvangi, 1945)

Cassidulina reniforme is an infaunal species and is one of the most common species living on Arctic shelves. It inhabits upper few centimetres of muddy sediments and prefers a cold-water (<2 ºC), relatively high salinity (>30) environment, with a seasonal sea ice coverage (Hald and Korsun, 1997; Polyak et al., 2002). The depth range of this species is wide occurring in fjords to shallow shelf environments (Hald and Korsun, 1997).

Ecologically it prefers a glaciomarine setting in the high latitudes located in the middle-inner fjord areas (Elverhøi and Bomstad, 1980; Korsun et al., 1995; Hald and Korsun, 1997). They are termed 'ice-proximal' faunas due to their abundance close to the glacier terminus, where it is considered to have poor conditions with an unstable and stressed environment (Hald and Korsun, 1997; Korsun and Hald, 1998). *C. reniforme* thrives in areas under the influence of cooled Atlantic Water (Hald and Vorren, 1987; Hald and Korsun, 1997). It can be in assemblages of both high and low diversity depending on the environmental conditions.

4.2.1.2 *Elphidium excavatum* forma *clavata* (Cushman, 1930)

Elphidium excavatum forma clavata, hereafter *E. excavatum* is a deep infaunal benthic species and is termed an 'ice-proximal' species due to its co-occurrence with *C. reniforme* close to glacier termini (Moodley and Hess, 1992; Hald and Korsun, 1997). *E. excavatum* is considered to be a eurytopic species as it is well-adapted to tolerate fluctuating environmental conditions. Close to the glacier front the environment is harsh, characterised by low salinity and temperature, and extremely turbid melt waters (Hald and Vorren, 1987; Hald and Korsun, 1997; Korsun and Hald, 1998).

This opportunistic species thrives in a relatively shallow water environment with a high accumulation of glaciomarine sediments, and has a tolerance to low oxygen content within the sediment column (Moodley and Hess, 1992; Hald and Korsun, 1997). Oceanographically their abundance could be related to several cold water masses such as Local Water, from sea ice formation or glacial melt water, Arctic Bottom Water or Intermediate Water (Hald and Korsun, 1997). Although *E. excavatum* thrives in low salinities it has been reported they thrive in brine influenced areas, which typically have a high salinity or areas with the presence of extended sea ice (Hald et al., 1994; Rasmussen et al., 2007).

4.2.1.3 *Nonionellina labradorica* (Dawson, 1860)

Nonionellina labradorica is an infaunal species that occupies deeper outer and middle fjord areas (Corliss, 1991; Korsun et al., 1995; Hald and Korsun, 1997). This glacier-distal species prefers cold (<1 ºC) and relatively temperate Transformed Atlantic Water with increased salinities above 30 ‰. (Cedhagen, 1991; Steinsund, 1994; Hald and Korsun, 1997; Korsun and Hald, 2000). The distribution of *N. labradorica* is associated with oceanic frontal zones such as the Arctic Front in the Barents Sea, which are areas of enhanced primary production. *N. labradorica* is highly abundant in these oceanic frontal areas that have a high supply of fresh phytodetritus setting to the benthos for it to consume, but it can also survive prolonged periods without any food supply (Cedhagen, 1991; Corliss, 1991; Hald and Korsun, 1997; Korsun and Hald, 2000). It may inhabit the deeper outer fjords of Svalbard as it will be less affected by seasonal variations such as sea ice (Hald and Korsun, 1997).

4.2.1.4 *Islandiella norcrossi* (Cushman, 1933)

Islandiella norcrossi is an infaunal species thrives in a glacier-distal environment in deeper outer fjord areas, suggesting it has a low tolerance for high sedimentation rates and turbulent water masses (Korsun and Hald, 2000; Zajączkowski et al., 2010). It is linked to the presence of Atlantic Water with relatively high and stable salinities (Polyak et al., 2002). In the Barents Sea *I. norcrossi* can be an indicator of seasonal sea ice cover and seasonal ice-marginal processes with high productivity supplying fresh phytodetritus to the benthos (Steinsund, 1994; Polyak et al., 2002).

4.2.1.5 *Cibicides lobatulus* (Walker and Jacob, 1798)

Cibicides lobatulus is an epifaunal species found in shallow water, coastal and fjord settings. It is predominantly used as an indicator of increased bottom current activity with a high food supply (Sejrup et al., 1981; Hald and Steinsund, 1992; Hald and Korsun, 1997). *C. lobatulus* is a suspension feeder and uses coarse sediments such as, sand and gravel as a substrate. In the Barents Sea it is linked to well-ventilated areas under the influence of warm Atlantic Water mixing with the cold, polar waters (Sejrup et al., 1981; Mackensen et al., 1985; Hald and Steinsund, 1992).

4.2.1.6 *Melonis barleeanus* (Williamson, 1858)

Melonis barleeanus is an infaunal species that thrives in an open-ocean ice-distal setting (Hald and Korsun, 1997; Korsun and Hald, 1998). It is found in high abundance in fine-grained, organic-rich marine muds in the troughs of the Barents Sea, suggesting it inhabits areas under the influence of high productivity conditions and sedimentation rates (Hald and Steinsund, 1992; 1996; Korsun and Hald, 1998; Polyak et al., 2002). The relative abundance of this species has been linked to the quality and quantity of food supply, related to slightly altered organic matter (Carlap, 1989).

4.2.1.7 *Cassidulina neoteretis* (Seidenkrantz, 1995)

Cassidulina neoteretis is an infanual species that inhabits shallow shelf to deep sea environments (150-3000 m) (Jansen et al., 1990; Seidenkrantz, 1995). *C. neoteretis* thrives in cold (-1 to 2 ºC), saline (34.9 ‰) bottom water conditions, linked to cooled, subsurface Atlantic Water (Mackensen and Hald, 1988; Polyak and Mikhailov, 1996; Lubinski et al., 2001). It is typically abundant in fine-grained organic rich muds and glaciomarine settings (Mackensen and Hald, 1988; Seidenkrantz, 1995). The co-occurrence of *C. neoteretis* with high abundances of planktonic species is suggested to be to be indicative of seasonally ice free conditions, with high seasonal productivity (Polyak and Mikhailov, 1996; Hald et al., 1999).

4.2.1.8 *Elphidium subarcticum* (Cushman, 1944)

Elphidium subarcticum is an epifaunal species that inhabits a shallow shelf setting under the influence of cold to temperature waters (Holtedahl, 1959; Sejrup et al., 1987). It has been documented that it is intolerant to extremely low or fluctuating salinities (Polyak et al., 2002).

4.2.1.9 *Buccella* spp. (Cushman, 1922; Bandy, 1950)

Buccella frigida and *Buccella tenerrima*, hereafter *Buccella* spp. are epifaunal species primarily linked to high seasonal productivity and seasonal sea ice cover, thriving on the supply of settling fresh phytodetritus (Roscoff and Corliss, 1992; Polyak and Solheim, 1994; Steinsund, 1994; Polyak et al., 2002). In the Barents Sea it has been documented that they like cold (0-1 ºC), saline (33-33 ‰) bottom waters (Steinsund, 1994).

4.2.1.10 *Stainforthia loeblichi* (Feyling-Hanssen, 1954)

Stainforthia loeblichi is an infaunal species and is predominantly used as an indicator of seasonal sea ice (Polyak et al., 2002). *S. loeblichi* is an opportunistic species linked to low sedimentation rates and high seasonal productivity in marginal ice zones (Cedhagen, 1991; Polyak et al., 2002,) and in the Barents Sea it is commonly associated with the Polar Front and high salinities (Steinsund, 1994; Hald and Korsun, 1997).

4.2.1.11 *Astrononion gallowayi* (Loebilch & Tappan, 1953)

Astrononion gallowayi has been described as either an infaunal species (Wollenburg and Mackensen, 1998). It commonly occurs with high abundances of *C. lobatulus* living in shallow water settings with coarse sediments, suggesting it is an epifaunal species linked to increased bottom current activity (Hald and Korsun, 1997; Polyak et al., 2002).

4.3.2 Ecology of agglutinated benthic species

4.3.2.1 *Adercotryma glomerata* (Brady, 1878)

Adercotryma glomerata is an epifaunal to shallow-infaunal species that inhabits sandy sediments in inner fjord to open shelf settings (Hald and Korsun, 1997; Korsun and Hald, 1998). *A. glomerata* is abundant when the occurrence of calcareous species is reduced, possibly due to its tolerance to particularly cold, saline water masses, particularly in areas of dense brine formation (Hald and Korsun, 1997; Rasmussen and Thomsen, 2015). In the Barents Sea its abundance has been linked to high productivity conditions near the mixing zone between cooled Atlantic Water and Polar Water (Hald and Korsun, 1997).

4.3.3 Ecology of planktonic species

4.3.3.1 *Neogloboquadrina pachyderma* (sinistral) (Ehrenberg, 1861)

Neogloboquadrina pachyderma (sinistral), hereafter *N. pachyderma* (s) is an Arctic species that thrives under polar surface water conditions (Bé and Tolderlund, 1971; Boltovskoy, 1996).

4.2.4.2 *Neogloboquadrina pachyderma* (dextral) (Ehrenberg, 1861)

Neogloboquadrina pachyderma (dextral), hereafter *N. pachyderma (d)* is the right-hand coiling variant of *N. pachyderma* (s) and is a sub-polar species that is linked to warm Atlantic surface water (Bé and Tolderlund, 1971; Carstens et al., 1997).

.

4.2.4.3 *Turborotalita quinqueloba* (Natland, 1938)

Turborotalita quinqueloba is classed as a sub-polar to Arctic species that is linked to oceanic frontal zones between Atlantic Water and Arctic water (Bé and Tolderlund, 1971; Carstens et al., 1997).

4.2.4.4 *Globigerina/Globigerinita* spp. (d'Orbigny, 1826; Ehrenberg 1861; Egger, 1893)

Globigerina bulloides, *Globigerinita uvula*, *Globigerinita glutinata*, hereafter *Globigerina/Globerinita* spp. are sub-polar species that thrive under the influence of warm Atlantic surface water or close to the Polar front (Boltovskoy et al., 1996; Carstens et al., 1997).

5. Results

5.1 Bathymetry

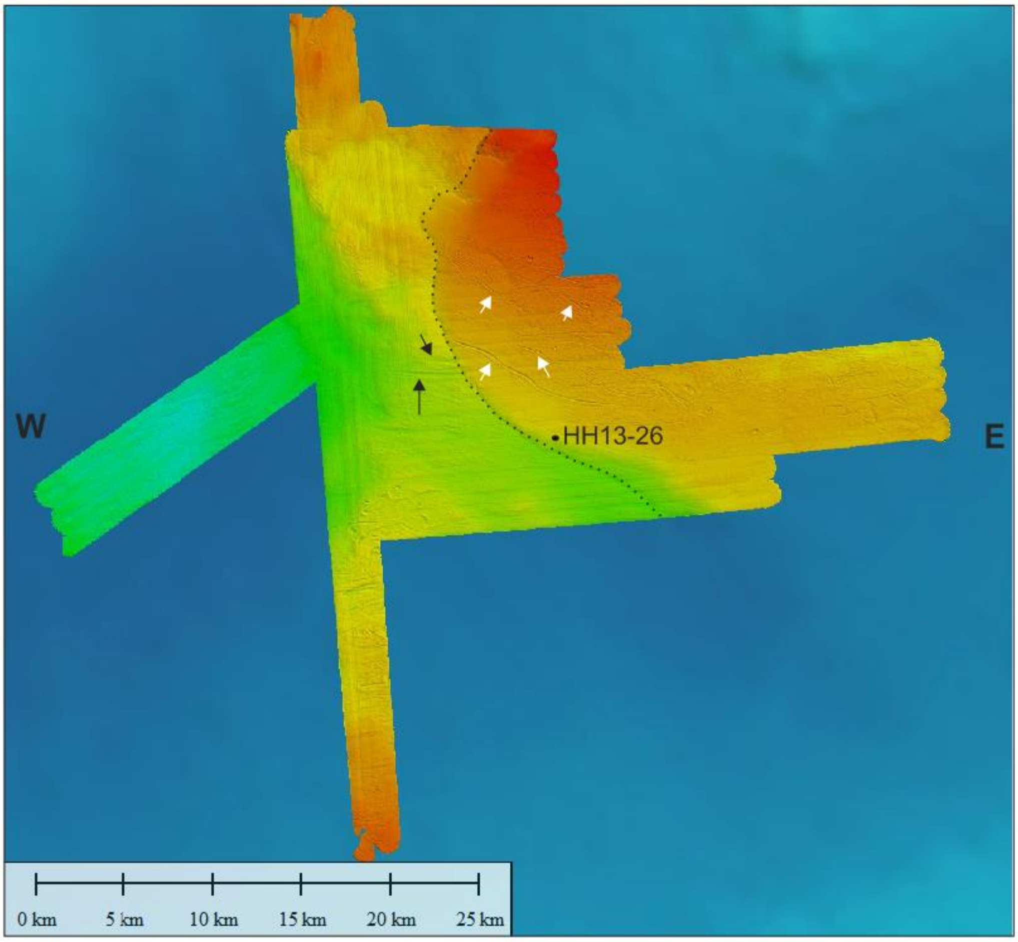

Figure 7: Multibeam bathymetric image of the core site HH13-26. The outline of the sediment lobe is highlighted by the black dashed line, the MSGL by the black arrows and the iceberg scours by the white arrows.

5.1.2 Description

The seafloor morphology of the core site is revealed from a high resolution image based on multibeam bathymetric data (Fig. 7). The surveyed area is dominated by a large protrusion extending from the east to the west (Fig. 7).

HH13-26 is located at 236 m water depth on the south-west boundary of the protrusion, which extends ~17 km to the north and ~21 km to the east of the core site. The curved margin of this submarine landform covers an area of ~30 km extending from the north to the south

(Fig. 7). The landform is raised in the north and to the east and tapirs down-slope towards the terminus.

The surface of the large protrusion is cut by large elongate grooves that appear to be of random orientation of various lengths (~2-10 km) (Fig .7).

Extending from the margin of the protrusion are large streamlined grooves (~1-4 km), that seem to have a preferred orientation from east to west (Fig. 7).

The mapped area does not cover the entire sediment lobe (Fig. 7) therefore it is not known the exact size or how the geomorphology appears further to the north and east.

5.2 Sub-bottom profile and acoustic units

The seafloor morphology and sediment structure in the surrounding the core site has been revealed by the acoustic sub-bottom (chirp) profile. Four acoustic stratigraphic units were identified through variations in acoustic characteristics (Fig. 8; table 6).

HH13-26 is recovered from a prominent sediment protrusion extending from the east to the west (~24 km) (Fig. 8). The interpretation of acoustic units A and B1 is supported by the lithology of HH13-26 (Fig. 12; Table 6), which penetrates through both of these units (Fig. 8b-c). The units that weren’t recovered in HH13-26 were interpreted based on their acoustic characteristics (table 6). The interpretation is supported by the interpretation of glacial sedimentary sequences from the acoustic characteristics from previous studies (e.g., LeBlanc et al., 1992; Noormets et al., 2002; Ottesen et al., 2008; Forwick and Vorren, 2012; Kempf et al., 2013).

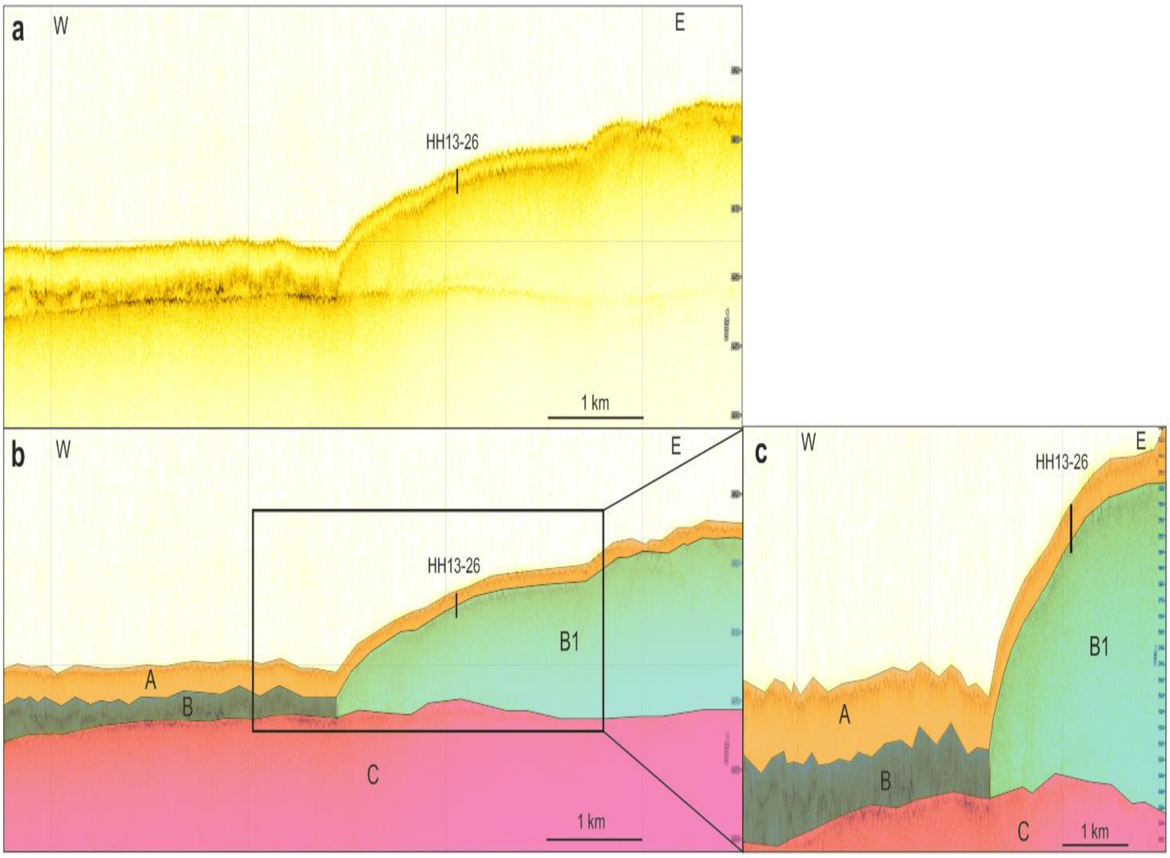

Figure 8: (a) Acoustic sub-bottom (chirp) profile of surveyed area with location of core site HH13-26. (b) Acoustic sub-bottom (chirp) profile of surveyed area with location core site HH13-26 and the acoustic units defined. (c) Acoustic sub-bottom (chirp) profile of core HH13-26 penetrating acoustic units A and B1.

Table 6: Acoustic units with descriptions of acoustic characteristics, geometry/dimensions, stratigraphic position and interpretation.

Units	**Acoustic characteristics**	**Geometry and dimensions**	**Stratigraphic position**	**Interpretation**
A	Medium amplitude, uniform/homogenous signature with a high continuity.	Conformable bedding, undulating surface to the east. 2-3 m thick above unit B1, 4-5 m above unit B.	Rests on unit B and B1. Contact between the units is sharp.	Glaciomarine deposits, possibly cut by ice-berg scours.
B	Chaotic, medium to high amplitude discontinuous reflectors terminating abruptly in contact with unit B1. Acoustically stratified with layers of various densities.	Filling-type in the lower part. 4-7 m thick.	Resting on C with a sharp contact. Overlain by unit A.	Proximal glacial with meltwater deposits.
B1	High amplitude reflectors on upper boundary. Diffuse, acoustic masking below.	Lobe-shape with an undulating surface. Thicker in the east (12-25 m), thinning westward.	Resting on C, contact between them isn't always sharp. Overlain by unit A. Sharp contact with unit B.	Glacial sediment lobe, composed of diamicton.
C	High amplitude reflectors below unit B. Low amplitude reflectors below unit B1, possible acoustic masking.	Uniform layer with an undulating surface to the west.	Acoustic basement, resting on bedrock.	Previous glacial succession or bedrock.

5.3 Modern hydrography

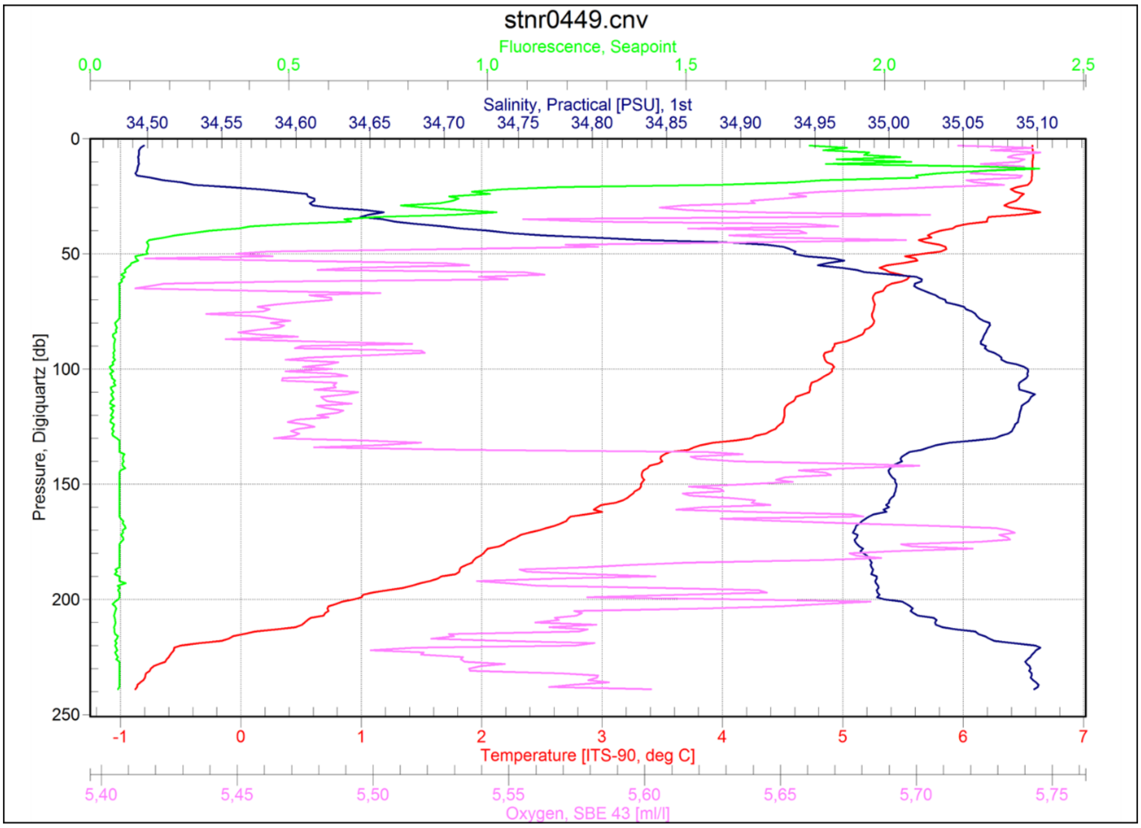

Figure 9: CTD station HH13-28 with profile of temperature, salinity, oxygen and fluorescence.

The core site is currently under the influence of four water masses as revealed by the CTD data and is supported by the literature (Quadfasel et al., 1988; Akimova et al., 2011). The water column consists of a warm (5.6-6.4 ºC), fresh (34.5-34.9) surface layer in the upper ~50 m (Fig. 9). A warm and fresh surface layer is typical in this region during summer (Akimova et al., 2011). Warm (>3.4 ºC), saline (35-35.1) Atlantic Water extends from ~50-140 m, below this lies relatively cold (-0.6 to 3.4 ºC), saline (35) East Spitsbergen Water (ESW) (Fig. 9). The temperature and salinity measured at the top of this water mass are slightly higher than the reported values for the Storfjorden Trough, suggesting a degree of mixing with the Atlantic Water (Skogseth et al., 2005). The ESW sits on top of a cold (-0.9 to –0.6 °C), saline (35.1) bottom water mass (Fig. 9), possibly brine-enriched shelf water common in this area (Skogseth et al., 2005).

5.4 Sedimentology

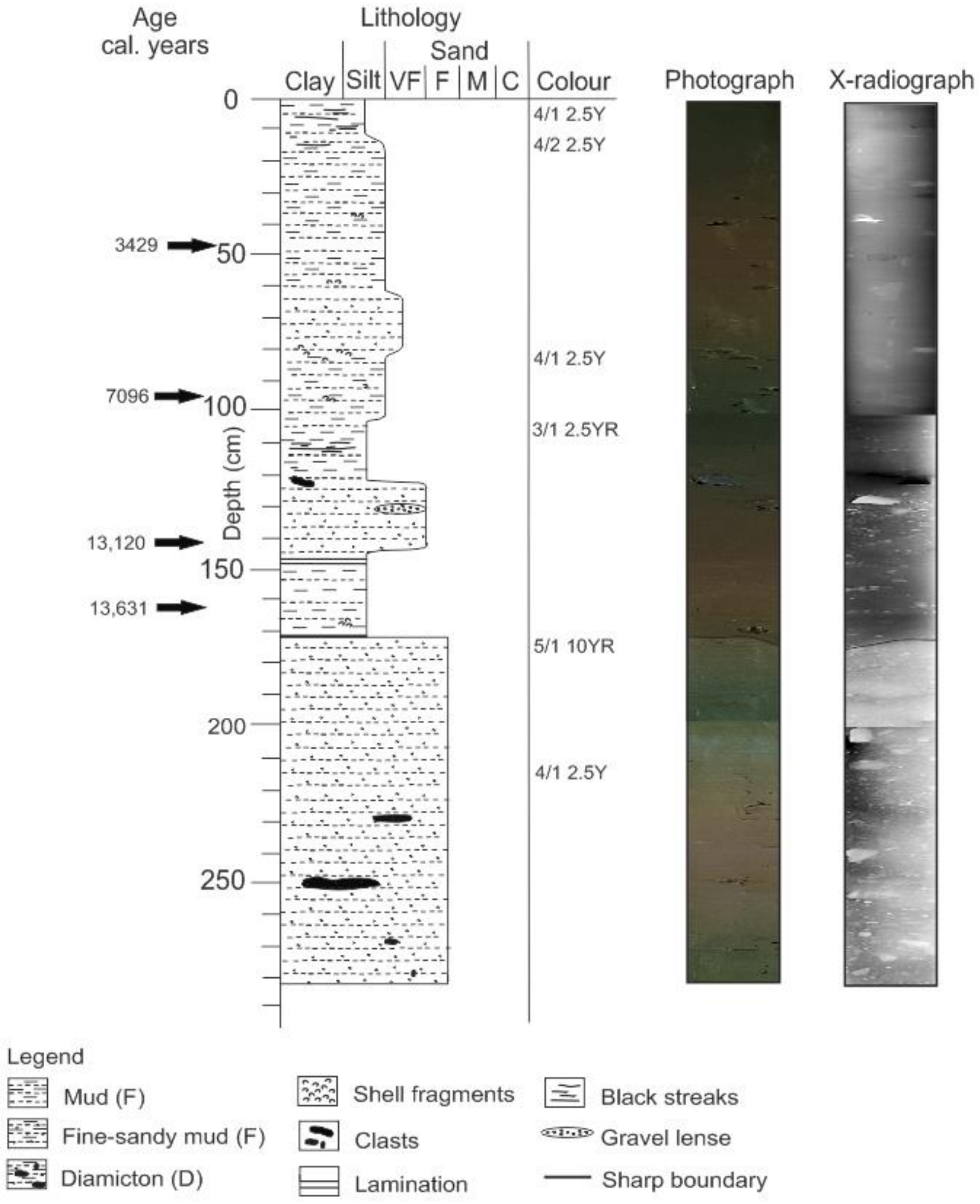

Figure 10: Lithological log with radiocarbon dates in calendar years indicated, photograph and x-radiograph image of core HH13-26.

5.4.1 Lithological description

In the lower section of the core (283-171 cm) the sediments are dry and compact, consisting of grey/dark grey (5/1 10YR / 4/1 2.5Y) fine sandy silt with frequent large clasts (Fig. 10). A prominent un-uniformed sharp boundary in both colour and decrease in grain size is observed at 171 cm. The sediments consist of fine silty clay from 171-146 cm with very few shell fragments and a light grey planar lamination between 148-147 cm. The sediments gradually coarsen to very fine to fine sandy silt between 146-127 cm with a lens of gravel sized clasts occurring between 132-128 cm. Above this, 127-104 cm contains very dark grey (3/1 2.5YR) silty clay with occasional black discontinuous streaks and a large clast. A gradual transition from dark grey (4/1 2.5Y) clayey silt between 104-82 cm with frequent shelf fragments, and a bivalve shell to very fine sandy silt with scattered shell fragments between 62-82 cm is observed. The grain size decreases between 62-15 cm to clayey silt with occasional worm tubes, bivalve shells and shell fragments. There is a gradual transition at 15 cm from dark greyish brown (4/2 2.5Y) clayey silt to dark grey (4/1 2.5Y) silty clay with black discontinuous streaks that continues to the top of the core.

5.4.2 X-radiographs

The x-radiographs image reveals the internal structure of the core showing a lower sequence of high density material with abundant presence of large clasts (lighter shades) from the base of the core to 171-174 cm (Fig. 10). At 171-174 cm there is a prominent tilted sharp contact with an abrupt transition between high density material to a lower density material with the occasional presence of small clasts. At 145 cm the content increases considerably up to 122 cm, however these are smaller in comparison to the lower portion of the core. The clast content is reduced between 122-104 cm with occasional small clasts. The upper sequence

(104-0 cm) is of low density material (darker shades) with occasional clasts and possibly shells (lighter shades).

5.4.3 Magnetic susceptibility

The magnetic susceptibility readings from both the loop and point sensors reveal a similar pattern of high values from the base of the core 283 cm to 224 cm (>35 SI 10^{-6}; >17 SI 10^{-6}) (Fig. 11). MS readings decrease between 224-202 cm steadily fluctuating between 31.1-51.6 SI 10^{-6} and 13.8-25.3 SI 10^{-6}. The values increase rapidly (23.7-27.7 SI 10^{-6}; 10.5-14.9 SI 10^{-6}) with a notable high in the MS between 202-189 cm. There is a sharp decrease in MS (36.6-28.3 SI 10^{-6}; 27.8-13.7 SI 10^{-6}) between 189-169 cm clearly shown in loop sensor data. Up-core the readings are more variable with decreased values (19.6-27.0 SI 10^{-6}; 10.5-22.5 SI 10^{-6}) between 168-104 cm. In the upper 104 cm of the core the MS shows a slight decreasing trend with relatively low and stable values (20.8-16.3 SI 10^{-6}; 16.6-9.7 SI 10^{-6})

The magnetic susceptibility record obtained the loop sensor was chosen when assigning the lithological units (Fig. 12) as it represents a more general overview of the MS pattern of the core, which is relevant for this study.

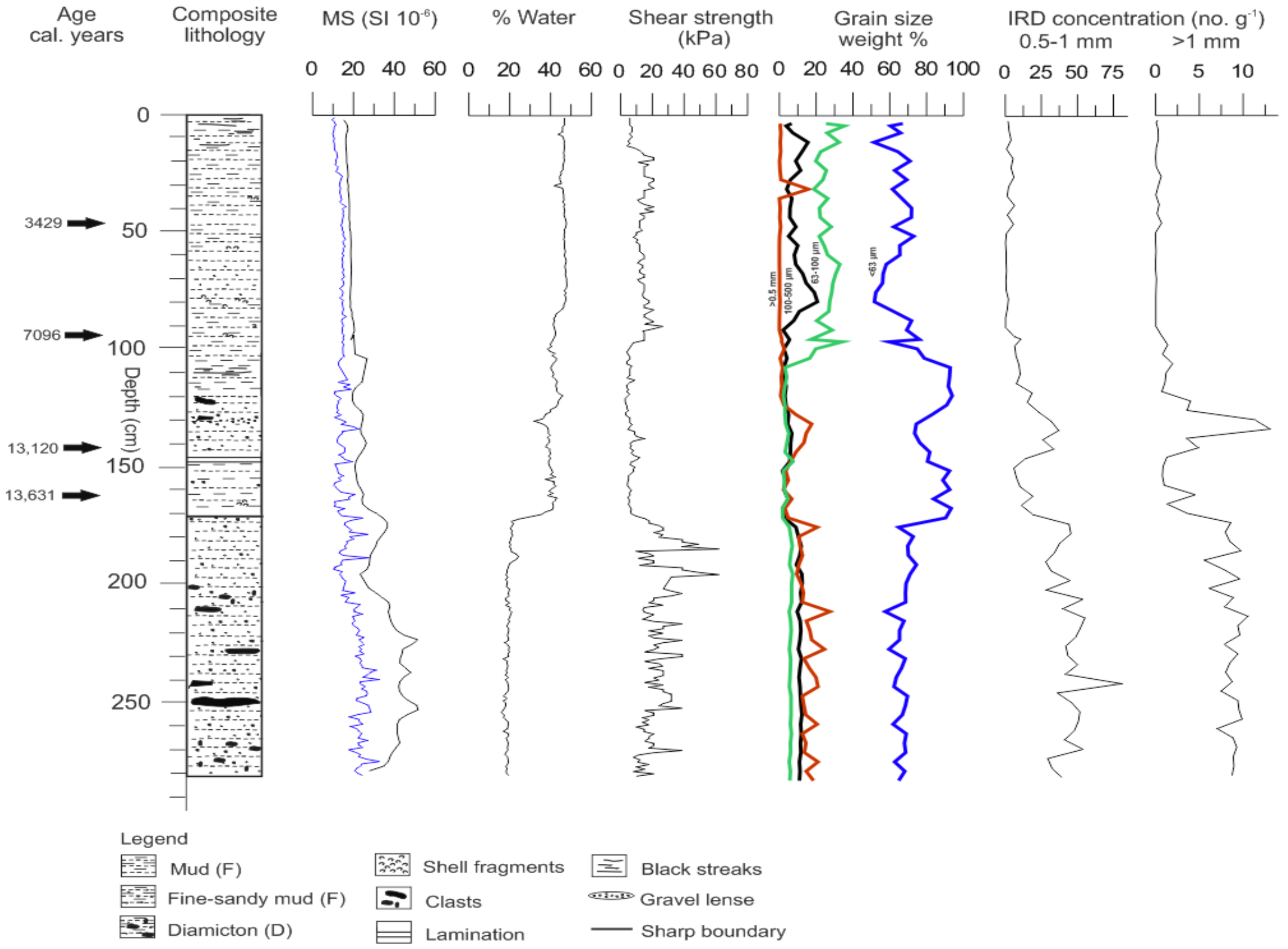

Figure 11: Composite lithological log of core HH13-26 with radiocarbon dates in calendar years indicated, loop (black line) and point (blue line) sensor magnetic susceptibility, % water content, shear strength, grain size weight % (>0.5 mm, red line; 100-500 µm, black line; 63-100 µm, green line; <63 µm, blue line), IRD concentration for 0.5-1 mm and >1 mm fractions.

5.4.4 Shear strength

The shear strength from the base of the core 283 cm to 195 cm displays a steady increasing trend with variable readings between 8.2-39 kPa (Fig. 11). Values increase sharply to 62 kPa at 196 cm and then decrease steadily to 10 kPa at 186 cm, before they increase sharply to 62 kPa at 185 cm. The shear strength decreases rapidly between 185-171 cm (62-10 kPa) with much lower readings (3.4-9.2 kPa) between 170-97 cm, except slightly increases values noted between 147-15 cm (10-15 kPa). Values between 96-14 cm are slightly increased and more variable (10-27 kPa), with low values <7.3 kPa in the upper 13 cm of the core.

5.4.5 Water content

The water content between the base of the core 283 cm to 188 cm are relatively constant and low with an overall increasing trend from 16-24 % (Fig. 11). Values decrease slightly at 187 cm to 21 % and remain almost constant up to 174 cm (20-22 %). A step-wise increasing trend occurs with a sharp decrease between 174-169 cm from 22-46 %, a slight increase between 169-120 cm (41-46 %) and variable high values between 120-82 cm (39-46 %). The upper 82 cm of the core consists of stable values of a relatively high water content (42-48 %).

5.4.6 Grain size distribution

The grain size distribution of the sediments is expressed as a percentage and varies considerably up-core (Fig. 11). The clayey silt content (<63 µm) is moderate (57-74 %) from the base of the core, 283 cm to 174 cm. The fine sand content (63-100 µm) is relatively constant 6-7 % and the 100-500 µm fraction is 10-12 %. The larger grain sizes (>0.5-1mm; >1mm) have high values ranging between 2-3 % and 7-25 % for the latter size fraction.

A prominent change in the grain size distribution is observed at 170 cm the clayey silt content (<63 µm) increases to values >84 % between 170-150 cm with fine sand content (63-100 µm;

100-500 µm) is <5 % (Fig. 11). The larger grain sizes (>0.5-1 mm; >1mm) are also in lower quantities (<1 %; <6 %).

The percentage of clayey silt (<63 µm) decreases slightly between 146-126 cm (73-83 %), with slightly increased fine sand content (63-100 µm, 3-7 %; 100-500 µm, 5-7 %). A large excursion in 0.5-1 mm and >1 mm (3%; 12-15%) is observed at within this depth interval (134-130 cm).

The percentage of clayey silt (<63 µm) increases rapidly and represents 91-94 % of the grain size distribution between 122-102 cm, with all other grain sizes in extremely low quantities (<4 % each) (Fig. 11).

The depth interval 102-82 cm decreases in clayey silt content with values between 59-79 %, whereas the very fine sand content (63-100 µm) has values frequently shifting between 17-34 %. A slight increase (2-6 %) is observed in the fine sand fraction (100-500 µm), and a slight decrease in medium/coarse sand fractions (0.5-1 mm; >1 mm) up to 0.52 % and 2.30% at 98 cm.

The clayey silt content (<63 µm) gradually increases to 52-66 % between 78-54 cm with a noticeable decrease in fine sand content (63-100 µm, 24-33 %; 100-500 µm, 8-21 %) (Fig. 11). The larger grain sizes (0.5-1 mm; >1 mm) remain exceptionally low (<0.11 %).

The upper 58 cm consists of 51-73 % clayey silt (<63 µm) and relatively high fine sand content (63-100 µm, 19-35 %; 100-500 µm, 4-16 %) (Fig. 11). The larger grain sizes 0.5-1 mm and >1 mm display extremely low values (<1 %), except for 30 cm where the large clasts (> 1 mm) accounted for 16 % of the grain size at this interval.

5.4.7 IRD concentration

The concentration of mineral grains is expressed as number of grains per gram of dry weight sediment for the 0.5-1 mm and >1 mm size fractions (Fig. 11).

The 0.5-1 mm fraction displays high, variable values from the base of the core 283 cm to 174 cm (28-81 g^{-1}) (Fig. 11). A sharp decrease is observed between 170-146 cm with the amount of mineral grains between 6-19 g^{-1}. The amount of mineral grains increases at 142 cm to 34 g^{-1} then decreases gradually between 138-118 cm to 37-15 g^{-1}. The upper portion of the core from 114-0 cm the 0.5-1 mm fraction has low values (<11 g^{-1}).

The >1 mm fraction follows a similar pattern as 0.5-1 mm with high values from the base of the core 283-174 cm (6-11 g^{-1}) (Fig. 11). A sharp reduction is observed at 170-138 cm (<5 g^{-1}), followed by a large peak (13 g^{-1}) at 134 cm. Values decrease sharply between 130-118 cm from 11-1 g^{-1} and the low values prevail to the top of the core (<2 g-1)

5.4.8 Lithological units

A composite log was produced based on a combination of the visual lithological description, grain-size analysis and x-radiographs (Fig. 10-12). This provides a more accurate representation of the lithology of the core by considering its internal structure and not only what is observed on the core surface.

The sedimentary sequence of HH13-26 was assigned standardised lithofacies codes based on the sediment composition and internal features (Eyles et al., 1983). The stratigraphy of HH13-26 was divided into two main lithological units described from the bottom of the core upwards; a). Diamicton unit (L1) and b). Fine-grained mud unit (L2) (Fig. 12). The lithological units are based upon similar sets of characteristics identified through lithofacies association and the sedimentological analyses described above (Fig. 10-12).

The shift in lithology between unit L1 and L2 is clearly shown on the all visual and sedimentological analyses performed e.g., X-radiographs, grain-size and magnetic susceptibility (Fig. 10-12). The lithological unit L2 was divided into sub-units; L2(a) and L2(b) due to the fluctuations in the grain-size and presence of clasts (Fig. 12). The assigned lithological units correspond to the acoustic units A and B1 as described in section 5.2 (Fig. 12).

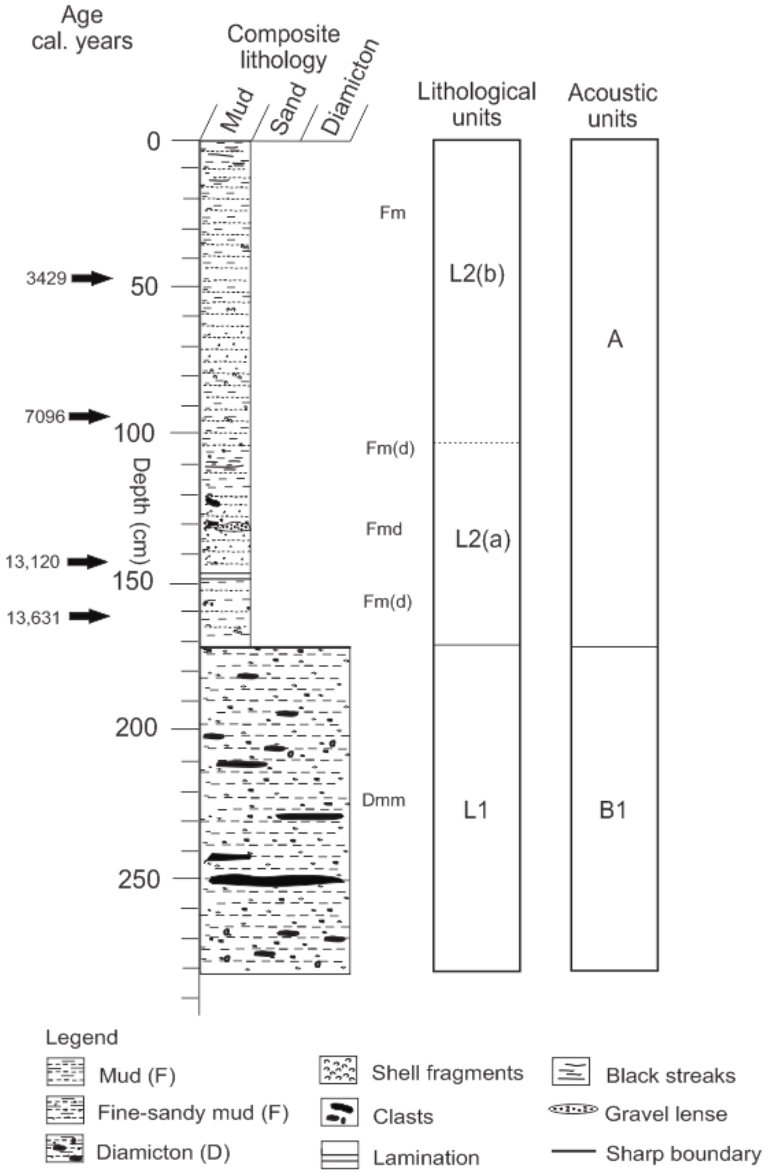

Figure 12: Composite lithology log of core HH13-26 with radiocarbon dates in calendar years indicated, assigned lithological units and acoustic units.

5.4.8.2 Diamicton unit (L1) (283-171 cm)

The basal unit occurs between 283-171 cm and consists of grey-dark grey (10YR 5/1; 2.5Y 4/1) matrix-supported, massive diamicton (Dmm) (Fig. 10; 12). Texturally the diamicton unit is composed of compact, poorly-sorted sediments in a fine-sandy mud matrix (Fig. 10-12). The upper limit of the unit is characterised by a sharp boundary in both colour change and increased grain size compared with unit L2 (Fig 10-12). The clast content (> 0.5 mm) varies throughout L1, it is most abundant in the lower 80 cm of the core (13-28 %) (Fig. 11) and is comprised of sub-angular to sub-rounded clasts. L1 is characterised by a high, variable MS (23.3-51.6 SI 10^{-6}) and shear strength (11-62 kPa), with a low water content (<24 %) (Fig. 11). The lithofacies code assigned to this unit is Dmm (Diamict, matrix -supported, massive) (Fig. 12).

5.4.8.1 Fine-grained mud unit (L2) (171-0 cm)

The uppermost unit is comprised of dark-very dark grey and dark greyish brown (2.5Y 4/1; 2.5Y 3/1; 2.5 Y 4/2) hemipelagic and glacigenic mud occurring between 171-0 cm (Fig. 10-12). The MS values are low to moderate (15.3-26.3 SI 10^{-6}) with a gradual up-ward decreasing trend that appears to decrease further with the absence of sand and clasts (Fig 11). The water content mirrors the MS record with a step-wise increasing trend (>32 %) towards the top of the unit and the shear strength is low to moderate (4.1-27 kPa) (Fig. 11) but is consistently lower than the diamicton unit. The overall lithology of L2 is similar, however there are slight changes in grain-size and clast content (Fig. 11-12). Unit L2 is described in its allocated sub-units L2(a) and L2(b):

Sub-unit L2(a) occurs between 171-104 cm and the sediments are composed of silty clay or fine sandy silt (Fig. 10). There is a prominent gravel lens occurring between 132-128 cm and a single 1 cm-thick lamination observed between 148-147 cm (Fig 10). The clast content in

L2(a) varies from rare, to abundant surrounding the gravel lens, which is clear from the x-radiographs (Fig. 10-12). The lithofacies codes allocated to this unit are Fm(d) and Fmd (Fine mud, massive with rare clasts; Fine mud, massive with clasts) (Fig. 12).

In sub-unit L2(b) texturally the sediments are silty clay, clayey silt and very-fine sandy silt that occur between 104-0 cm, with an extremely rare occurrence of clasts. The lithofacies code assigned to this sub-unit is Fm (fine mud, massive) (Fig. 10).

5.5 Radiocarbon dating and age model

The chronology of HH13-26 is based on four AMS ^{14}C dates yielded from samples containing bivalves and benthic foraminifera (Table 3; 7). The radiocarbon dates were calibrated into calendar age (years before present) as described in detail in the methods chapter (3.4.13). The calendar ages range from 3429 ±100 cal. years to 13,631 ±173 cal. years spanning the late Holocene to the Allerød interstadial period (Table 7).

The calendar ages were plotted against depth to show the age distribution of HH13-26 (Fig. 13), where a linear sedimentation rate between the calibrated ages was assumed and the top of the core (0 cm) is expected to be recent (Table 8).

The lower 120 cm of the HH13-26 was not dated due to the lack of reliable datable material in the oldest part, which appears to be a common problem in many studies (e.g., Rasmussen and Thomsen, 2015). A similar style of sedimentation occurs below the oldest date obtained at 163 cm to 171 cm where the abrupt lithological change to diamicton occurs (Fig. 12). A linear sedimentation rate between 163-171 cm was assumed and the age of the sediments at 171 cm is calculated to be 13,817 cal. years (Table 8). Therefore, the minimum age of the diamicton unit (L1) is speculated to be around this date.

Table 7: Details of samples sent for radiocarbon dating, the mean age in calendar years is used for the age model.

Lab code	**Sample depth (cm)**	**^{14}C age**	**Calibrated ages 2σ range (cal. years)**	**Mean age (cal. years)**	**Dated material**
UBA-31414	48-50	3635 ±29	3329 - 3528	3428.5 ±100	Bivalve shell
UBA-31415	95-97	6683 ±35	6975 - 7216	7096 ±121	Bivalve shell
UBA-31416	141-142	11,765 ±88	12,908 - 13,331	13,120 ±212	Benthic foraminifera
UBA-31417	163	12,285 ±57	13,458 - 13,804	13,631 ±173	Bivalve shell

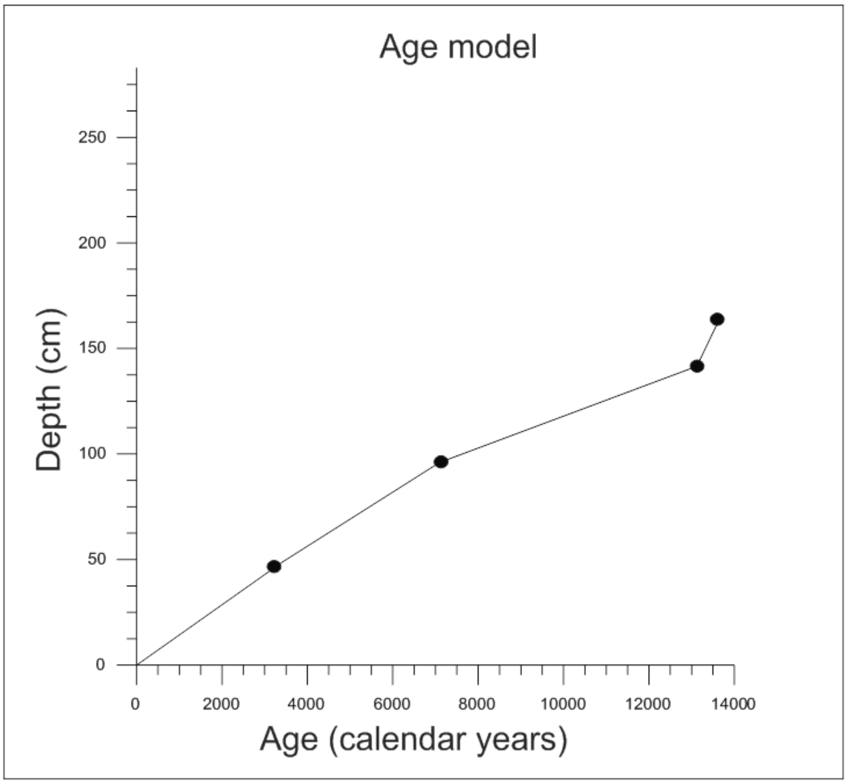

Figure 13: Age model with age in calendar years plotted against core depth, assuming linear sedimentation rates between the data points.

5.6 Sedimentation rates

The sedimentation between the dates are assumed to be constant, therefore the linear sedimentation rate was estimated from the age and depth between the intervals. Four sedimentation rates were calculated and they have varied greatly over time (Table 8).

The sedimentation rates are relatively similar in the upper 96 cm of the core with estimates of 14.3 cm ky^{-1} between 0-49 cm and 12.8 cm ky^{-1} between 49-96 cm (Table 8). The sedimentation rate decreases to 7.6 cm ky^{-1} between 96-141.5 cm then increases sharply to 42.1 cm ky^{-1} between 141.5 cm to 171 cm.

Table 8: Calculated linear sedimentation rates between the radiocarbon dates in calendar years.

Depth interval (cm)	**Age interval (cal. years)**	**Sedimentation rate (cm ky^{-1})**
0-49	0-3429	14.3
49-96	3429-7096	12.8
96-141.5	7096-13,120	7.6
141.5-171	13,120-13,817	42.1

5.6.1 Mass accumulation rates (MAR)

The accumulation of sediments over time was calculated by converting the sedimentation rate into a mass accumulation rate (g cm^{2} ky^{-1}) using the dry bulk density (Fig. 14). The MAR in the upper 138 cm are low and relatively constant (3.38-6.21 g cm^{2} ky^{-1}). A sharp increase is observed at 142 cm to 17.39 g cm^{2} ky^{-1} and values remain high (>13.40 g cm^{2} ky^{-1}) to 170 cm.

5.6.2 Ice-rafted debris and sediment flux

The IRD flux is calculated based on the relationship of clast count and the MAR, and is expressed as an accumulation rate, hereafter, flux of IRD (no. cm^{2} ky^{-1}). The 0.5-1 mm fraction has a greater accumulation rate than the >1 mm fraction e.g., at 142 cm the 0.5-1 mm fraction accumulated 585 cm^2 ky^{-1} compared to 85 cm^2 ky^{-1} for the >1 mm fraction (Fig. 14). The flux for both size fractions followed a similar pattern therefore they were added together to show an overall flux of IRD. The IRD flux (0.5-1 mm; >1 mm) is low in the upper 122 cm (>72 cm^2 ky^{-1}) then increases slightly to values ranging from 94-212 cm^2 ky^{-1} between 126-138 cm (Fig. 14). A sharp increase to 669 cm^2 ky^{-1} is observed at 142 cm and below this values decrease slightly but remain relatively high (153-511 cm^2 ky^{-1}).

The sediment flux is calculated based on the relationship of the percentage of the grain size interval and the MAR, and is expressed as a flux of each grain size interval g cm^2 ky^{-1}. The flux of the <63 µm fraction is relatively uniform and low in the upper 138 cm of the core (207-414 g cm^2 ky^{-1}) (Fig. 14). There is a sharp increase in the flux of <63 µm to 1421 g cm^2 ky^{-1} at 142 cm, steadily increasing to a maximum flux of 2057 g cm^2 ky^{-1} at 158 cm. Values decease slightly but remain high (1122-1990 g cm^2 ky^{-1}) to 170 cm.

The flux of the 63-100 µm fraction varies more overtime throughout the core (Fig. 14). The upper 102 cm the flux of sediment is most variable (57-213 g cm^2 ky^{-1}) and decreases to lower values (8-22 g cm^2 ky^{-1}) between 106-138 cm. The flux of 63-100 µm increases sharply at 146 cm to 153 g cm^2 ky^{-1} and then decrease to 31-62 g cm^2 ky^{-1} to 170 cm

The flux of the 100-500 µm fraction displays a similar pattern to that of the 63-100 µm fraction, with variable values (21-95 g cm^2 ky^{-1}) in the upper 86 cm (Fig. 14). A large decrease is observed with a sediment flux between 8-31 g cm^2 ky^{-1} between 90-138 cm, followed by a sharp increase to the maximum rate of 117 g cm^2 ky^{-1} at 146 cm. Values are slightly decreased (36-75 g cm^2 ky^{-1}) to 170 cm.

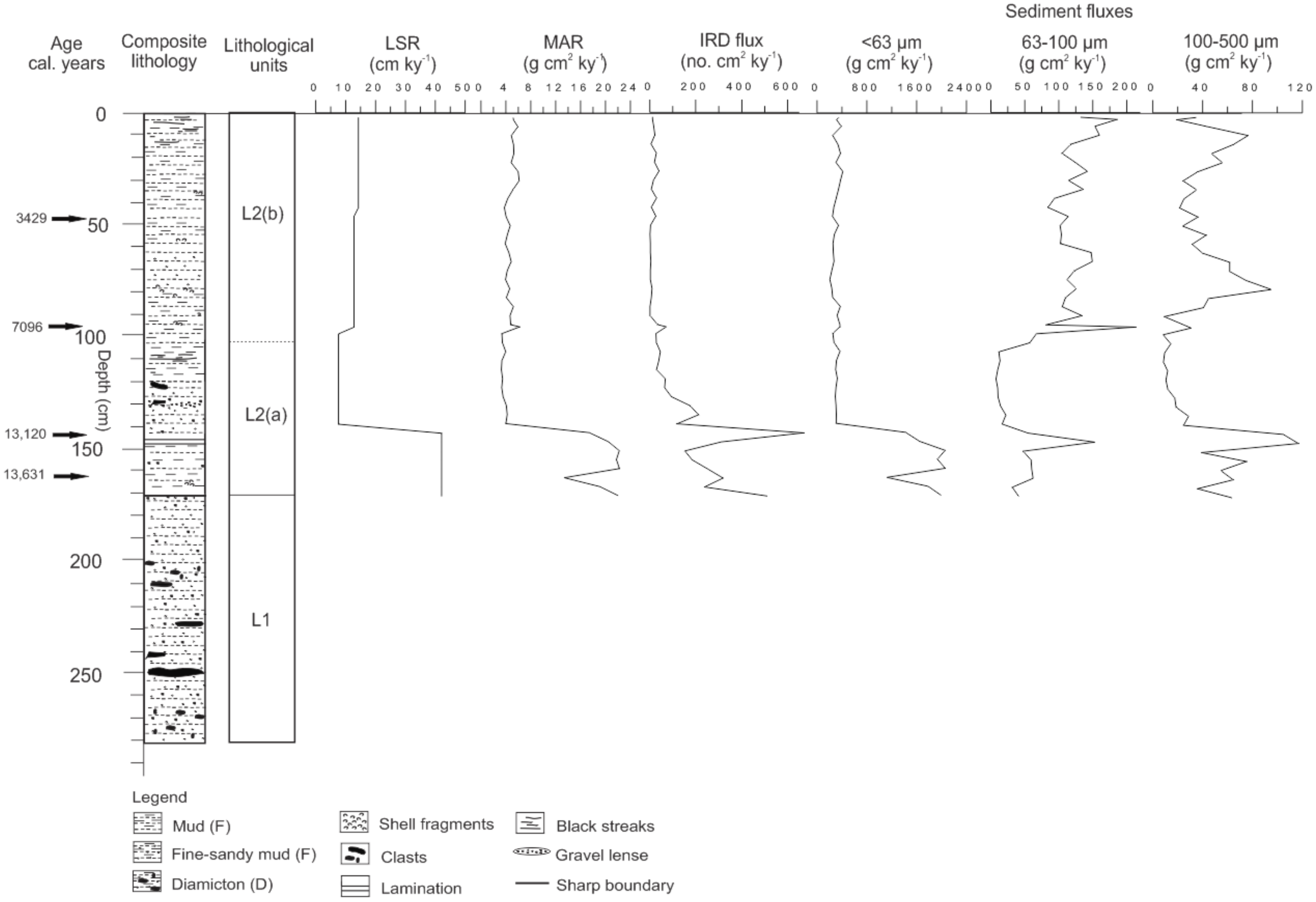

Figure 14: Composite lithological log with radiocarbon dates in calendar years indicated, lithological units, linear sedimentation rates, mass accumulation rates, IRD flux, sediment flux of the various grain sizes.

5.7 Stable isotopes

The stable isotope ($\delta^{18}O$ and $\delta^{13}C$) measurements were obtained from benthic foraminifera from core HH13-26 (Fig. 15). The species selected were *C. lobatulus*, *C. reniforme* and *I. norcrossi*. Unfortunately, five samples containing *C. reniforme* and five samples containing *C. lobatulus* did not contain enough material for measurement. Seven samples composed of *C. reniforme* were noted that because of the small sample size the measurement obtained had a high standard deviation, which was considered, when interpreting the results.

The $\delta^{13}C$ record from *C. reniforme* and *I. norcrossi* has relatively constant values up-core, whereas the *C. lobatulus* $\delta^{13}C$ record fluctuates (Fig. 15). The $\delta^{18}O$ record from all three species appears to follows a similar pattern up-core. As mentioned in the methods chapter (3.4.15.6) the stable isotope record from *C. lobatulus* is desired as it is an epifaunal species, which records the bottom water conditions, whereas *C. reniforme* and *I. norcrossi* are infaunal species and record the conditions of the sediment pore water. Considering this, the stable isotope record for this study will mainly focus on that obtained from *C. lobatulus* and only refer to *C. reniforme* and *I. norcrossi* as an overlap.

5.7.1 $\delta^{13}C$ record

The $\delta^{13}C$ values from the lowest samples (162-150 cm) were not measured from *C. lobatulus* due to the lack of material in the samples. Measurements from *C. reniforme* and *I. norcrossi* are low and relatively constant (-0.57 to -0.52 ‰; 0.04 to -0.18 ‰, respectively) (Fig. 15).

The *C. lobatulus* $\delta^{13}C$ record is characterised by two events with low values; at 146-138 cm with the lowest value recorded at 142 cm (-0.28 ‰), and $\delta^{13}C$ was 0.61 ‰ at 66 cm. $\delta^{13}C$ values increase sharply at 134-130 cm (1.33-1.21 ‰) (Fig. 15). There are no measurements of $\delta^{13}C$ from *C. lobatulus* between 126-114 cm due to the lack of specimens in this interval. *C. reniforme* displays slightly increased, relatively constant values (-0.41 to -0.67 ‰).

The $\delta^{13}C$ measurements recorded in *C. lobatulus* are slightly decreased at 110 cm to 0.95 ‰ and there was no measurement obtained from 106 cm, however the trend appears to gradually increase at 102 cm to 1.40 ‰ (Fig. 15). This increasing trend between 110-106 cm is observed in *C. reniforme* (-0.82 to -0.41 ‰). The $\delta^{13}C$ record remains relatively stable between 102-70 cm with higher values obtained from *C. lobatulus* between 1.27-1.63 ‰.

At 66 cm a distinct low measurement of $\delta^{13}C$ from *C. lobatulus* is observed (0.61 ‰) followed by a sharp increase to higher, stable values with a slight decreasing trend between 62-38 cm (1.37-1.30 ‰) (Fig. 15). Values decrease slightly between 34-30 cm (1.20-1.13 ‰).

The $\delta^{13}C$ record obtained from *C. reniforme* shows variable values between 26-0 cm (-0.29 to -1.18 ‰), but this could be due to the small amount of material in the sample and subsequent higher standard deviation noted in the measurements (Fig. 15). The *C. lobatulus* measurements of $\delta^{13}C$ higher in the upper portion of the core (22-0 cm), with a slight increasing trend observed between 22-14 cm of 1.19-1.53 ‰ and values between 1.31-1.60 ‰ at 6-3 cm. $\delta^{13}C$ measurements were not obtained from *C. lobatulus* at 26 cm and 10 cm due to the lack of material in the sample.

5.7.2 $\delta^{18}O$ record

The $\delta^{18}O$ record was corrected for ice volume effects and all three species appear to record a similar pattern up-core (Fig. 15). As with $\delta^{13}C$ no measurements of the $\delta^{18}O$ content in *C. lobatulus* were attained between 170-154 cm. $\delta^{18}O$ values recorded in *I. norcrossi* and *C. reniforme* are relatively stable (3.91-3.97 ‰; 3.39-3.60 ‰). At 146 cm the $\delta^{18}O$ values decrease sharply to 2.88 ‰ for *C. reniforme* and this low value of $\delta^{18}O$ also occurs in *C. lobatulus* (2.81 ‰). $\delta^{18}O$ values are higher and stable between 142-130 cm with 3.63-3.67 ‰ recorded from *C. lobatulus* and 3.13-3.45 ‰ from *C. reniforme*.

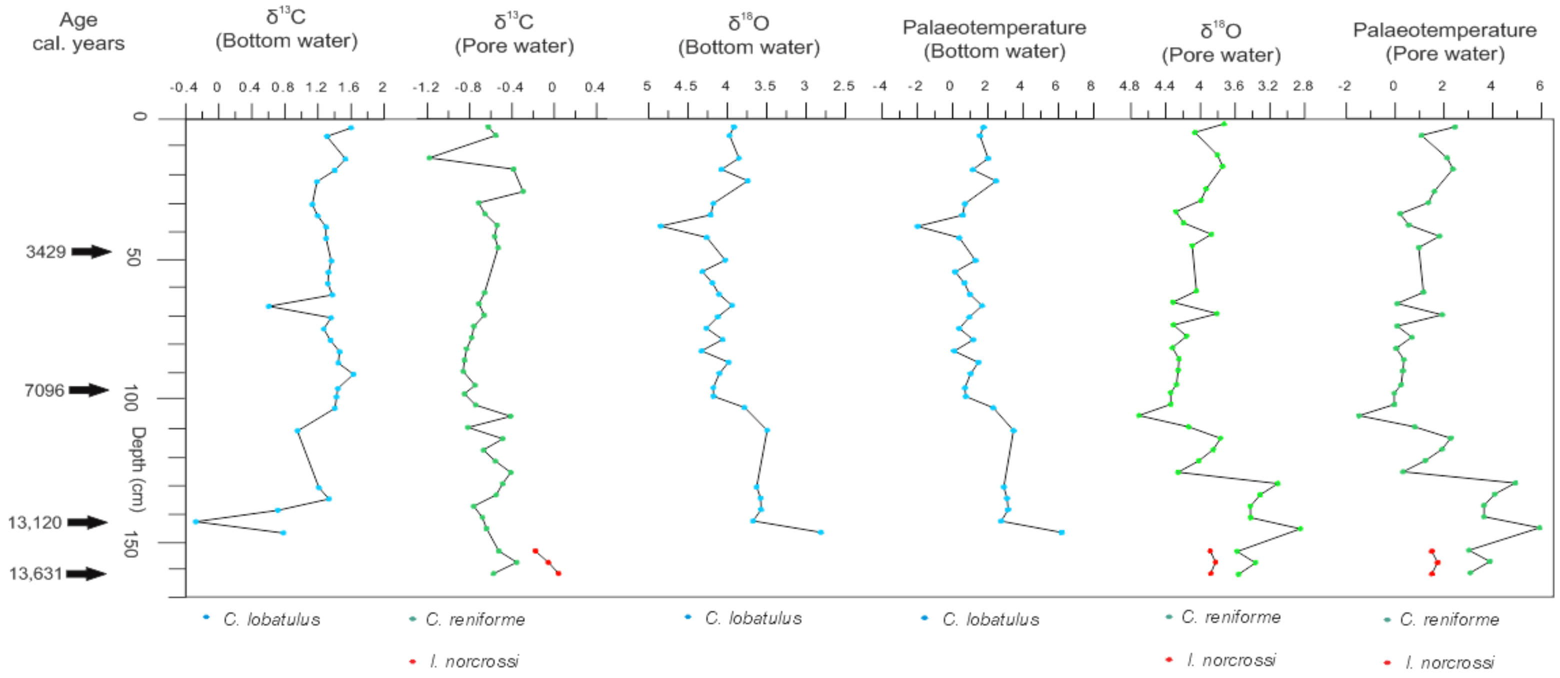

Figure 15 Measurements of stable isotopes of $\delta^{13}C$ and $\delta^{18}O$ and calculated palaeotemperatures from benthic foraminifera species C. lobatulus, C. reniforme and I. norcrossi, with radiocarbon dates in calendar years indicated.

There are no $\delta^{18}O$ data obtained from *C. lobatulus* between 126-114 cm or 106 cm. The $\delta^{18}O$ values measured in *C. reniforme* increase at 126 cm to 4.28 ‰ and slightly decrease to 3.79 ‰ at 114 cm. $\delta^{18}O$ is 3.49 ‰ at 110 cm in *C. lobatulus* and displays an increasing trend to 4.17 ‰ at 98 cm. The values of $\delta^{18}O$ are high between 98-42 cm, fluctuating between 3.99-4.33 ‰ for *C. lobatulus* and 3.83-4.37 ‰ for *C. reniforme*. A notable high peak is observed at 38 cm (4.85 ‰) for *C. lobatulus* and reduces to lower values with a slight decreasing trend (4.21-3.74 ‰) between 34 cm and the top of the core. The decreasing trend in $\delta^{18}O$ from 34-0 cm is also observed in the measurements from *C. reniforme* (4.31-3.83 ‰).

5.8 Foraminifera

5.8.1 Benthic foraminifera

A total of 45 calcareous species and 7 agglutinated species were identified representing a diverse and well-preserved foraminiferal assemblage within core HH13-26. The fauna was predominantly composed of calcareous benthic foraminifera (86-100 %) with a minor contribution from agglutinated species (<14 %) (Fig. 16).

Only the upper 170 cm contained enough specimens for quantification. The lower portion of the core was either totally devoid of foraminifera or specimens were rare and were poorly preserved showing an indication that they were possibly re-worked. The upper 126 cm of the core contained abundant bivalves, shell fragments and the presence of ostracods is frequent. Ostracods are abundant between 130-142 cm and become rare or absent below 146 cm.

The foraminiferal record was divided into seven foraminiferal assemblage zones (AZ1-AZ7), based on the distribution patterns of the benthic species (Fig. 16-17). The assemblage zones also correspond to changes in the sedimentology and foraminiferal accumulation rates (Fig 10-11; 16-17). *C. renifor*me and *E. excavatum* primarily dominate the calcareous faunas and appear to display an inverse relationship in many of the assemblage zones (Fig. 17). The other species that contribute to the benthic foraminiferal assemblages of HH13-26 include calcareous species; *N. labradorica*, *I. norcrossi*, *M. barleeanus*, *E. subarcticum*, *C. neoteretis*, *C. lobatulus*, *S. loeblichi*, *Buccella* spp. and *A. gallowayi*, and agglutinated species *A. glomerata* (Fig. 17). Some specimens of *Cassidulina* spp. and *Islandiella* spp. could not be distinguished between, as described in the methods chapter (3.4.11) they were grouped together and are included in the foraminiferal assemblages (Fig. 17). The relative abundance of the dominant species was plotted versus depth and will henceforth be discussed from the lower-most assemblage zone (AZ1) (Fig. 17).

It should be noted that if the species of *Cassidulina* or *Islandiella* could have been identified accurately it may have contributed greatly to either the *Cassidulina* or *Islandiella* species abundance. Some specimens were too badly preserved to distinguish between the two genus's. Other specimens were of such bad preservation condition there were no identifiable features. They were therefore classed as 'indeterminate species', but only represented 0-2.5 % of the foraminiferal distribution. Many of the agglutinated specimens were broken, which is common due to disintegration soon after death (Rasmussen and Thomsen. 2014). It should be considered if they were well-preserved it would have given a more accurate representation of the foraminiferal distribution.

The percentage of calcareous test fragments per sample was calculated, relative to the benthic foraminifera concentration (Fig. 16). This could show a pattern of preservation of the foraminifera.

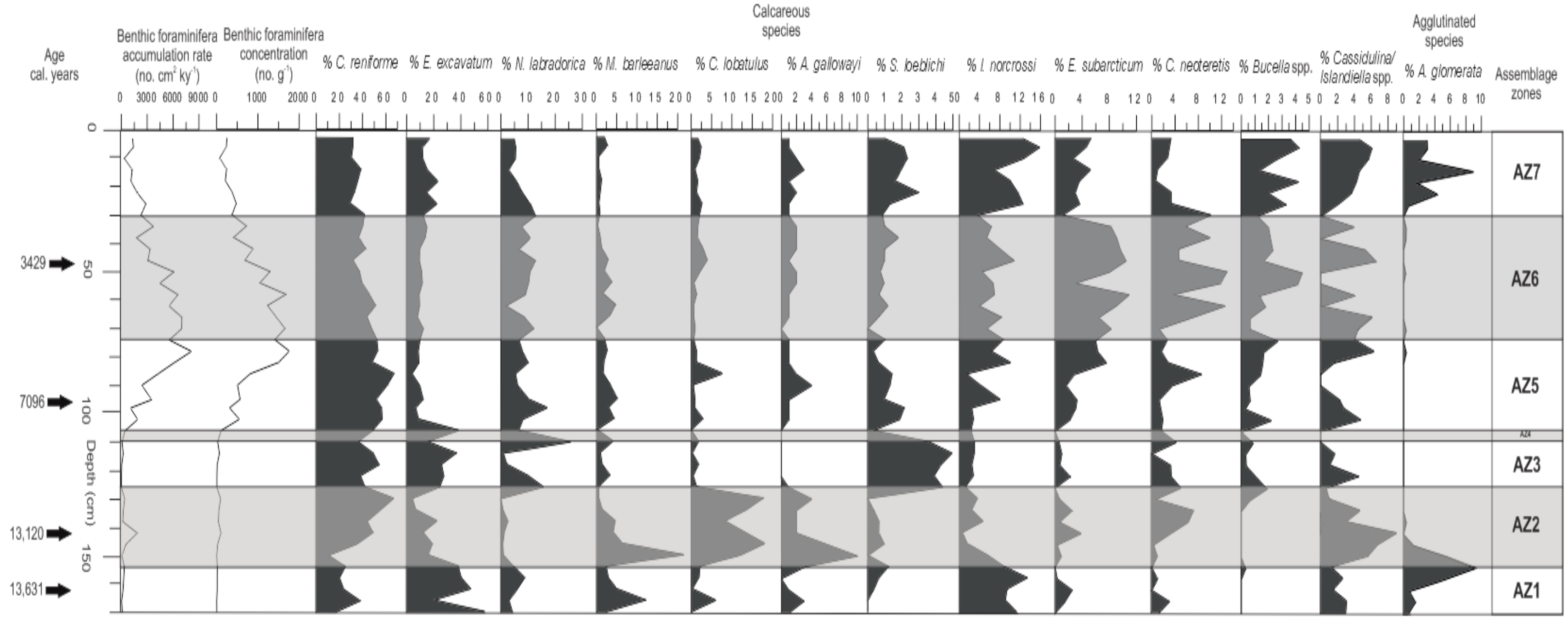

Benthic foraminifera are rare or absent below 170 cm.

Figure 16: Benthic foraminifera accumulation rate and concentration, relative abundance of dominant species plotted versus depth with assemblage zones and radiocarbon dates in calendar years indicated.

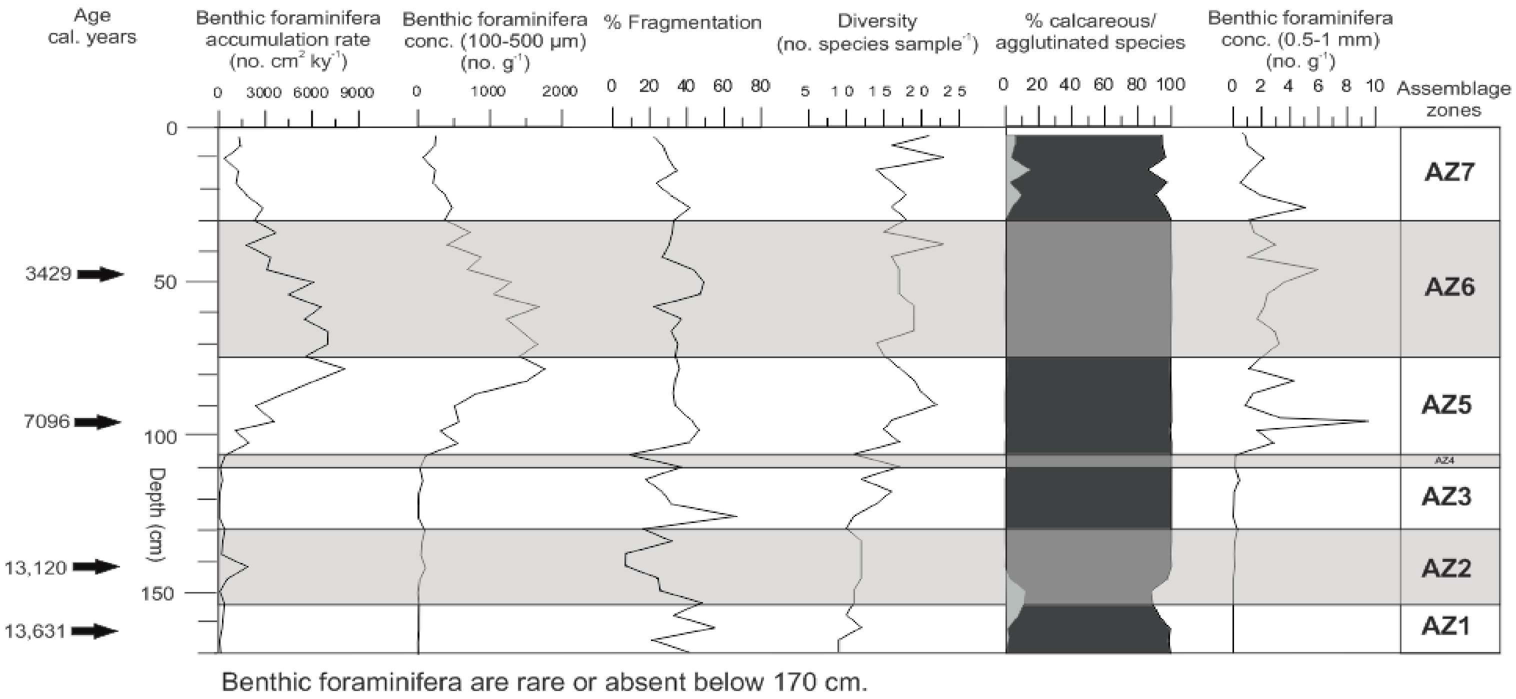

Figure 17: Benthic foraminifera accumulation rate and concentration, percentage of fragmentation, diversity, % calcareous/agglutinated specimens, benthic foraminifera concentration for the 0.5-1mm size fraction plotted versus depth and assemblage zones, with radiocarbon dates in calendar years indicated.

5.8.2 Benthic foraminiferal assemblage zones

5.8.2.1 Assemblage zone 1 (AZ1) (170-154 cm)

The fauna in AZ1 is dominated by the co-occurrence of the opportunistic species *E. excavatum* and *C. reniforme* with an average relative abundance of 41 % and 25 % respectively (Fig. 17). *I. norcrossi* has a moderate relative abundance in this zone of 9-13 %, peaking at 158 cm. *N. labradorica* is present in low abundances (<3 %) except for a peak of 9 % at 158 cm and *A. gallowayi* occurs in low abundances (<3 %) (Fig. 17). *M. barleeanus* and *C. lobatulus* are also of low relative abundance (<5 %; <3 %), apart from peaks at 166 cm (12 %; 6 %) (Fig. 17).

A notable peak in agglutinated species occurs in this zone constituting up to 7 % of the benthic fauna at 158 cm, below this the abundance of agglutinated species is <2 % (Fig 16). *A. glomerata* accounts for 5 % of the benthic foraminifera at 158 cm (Fig. 17), with extremely minor contributions (<1 %) from *Recurvoides turbinatus* and *Cribrostomoides crassimargo*.

Overall this zone has a low foraminiferal concentration, accumulation rate, and species diversity (Fig. 16). The concentration of foraminifera is particularly low (<16 g^{-1}) and the accumulation rate of benthic foraminifera decreases from 359 cm^2 ky^{-1} to 122 cm^2 ky^{-1} at the base of this zone (Fig. 16-17). The species diversity is <12 species per sample and the percentage of fragmentation was variable (22-55 %) (Fig. 16). The lowest three samples had less than 300 specimens in the entire sample (170 cm; 167; 166 cm; 65, 162 cm; 277).

5.8.2.2 Assemblage zone 2 (AZ2) (154-130 cm)

C. reniforme clearly prevails over *E. excavatum* in AZ2 with a gradual increasing trend in abundance towards the top of the zone 10-67 %, with an average relative abundance of 43 % for *C. reniforme* and 14 % for *E. excavatum* (Fig. 17). The average relative abundance of *C.*

lobatulus is high (14 %) in AZ2, with two notable peaks; 150-142 cm (12; 18%) and 134-130 cm (14; 18%) (Fig. 17). *M. barleeanus* has a low relative abundance except for a large isolated peak of 21 % at 150 cm (Fig. 17). There are minor contributions from *A. gallowayi* (<10 %), *C. neoteretis* (<7 %), *I. norcrossi* (<5 %), *E. subarcticum* (<4 %) and *N. labradorica* (<3 %) (Fig. 17). The undistinguished genus *Cassidulina*/*Islandiella* spp. was present in low to moderate abundances (1-9 %) with the highest value occurring at 142 cm (Fig. 17).

Agglutinated species contribute to 12 % of the fauna at the base of this zone, however decrease rapidly to <3 % above 150 cm (Fig. 16). *A. glomerata* is the most dominant agglutinated species, accounting for 1-9 % of the benthic foraminiferal fauna between 154-146 cm (Fig. 17). *R. turbinatus*, *T. nana*, *D. orchracea* and *C. crassimargo* provide extremely minor contributions (<1 %) to the agglutinated species relative abundance.

The species diversity is slightly improved in this zone with more persistent species numbers (11-12 species per sample) (Fig. 16). The accumulation rate of benthic specimens is low, except for a minor peak at 142 cm of 1841 cm^2 ky^{-1} and the concentration of benthic specimens is also low (<106 g^{-1}) (Fig. 16). The percentage of fragmentation was low to moderate between 7-32 %, but increases at the top of the zone to 67 % at 126 cm (Fig. 16). One sample from this zone had less than 300 specimens in the whole sample (150 cm; 107).

5.8.2.3 Assemblage zone 3 (AZ3) (130-110 cm)

C. reniforme is dominant in this zone with an average relative abundance of 44 %, followed by *E. excavatum* with an average relative abundance of 26 % (Fig. 17). The relative abundance of *E. excavatum* is at its lowest at the top of AZ3 (15%) where *N. labradorica* has an increased abundance from 2 % to 26%. *N. labradorica* is moderately abundant in the base of this zone (10-16%) (Fig. 17). There is a clear switch in faunas from *C. lobatulus* decreasing sharply to <2 %. *S. loeblichi* is present with 4-5 %. The contributions the following species are similar to zone AZ2; *C. neoteretis* (<5%), *I. norcrossi* (<3 %), *M. barleeanus* and *E. subarcticum* (<2 % each) (Fig. 17). The relative abundance of *A. gallowayi* is reduced <1 %, with the appearance of *Buccella* spp. with 1%. *Cassidulina*/*Islandiella* spp. showed a decreasing trend in relative abundance from 4-0 % (Fig. 17).

AZ3 predominantly consists of calcareous benthic species (>99 %). The concentration and accumulation rate of benthic foraminifera remain extremely low (<16 g^{-1}; <222 cm^{2} ky^{-1}). The percentage of fragmentation was moderate 18-37 %. The species diversity is generally increasing (11-17 species per sample) (Fig. 16). Two samples from this zone had less than 300 specimens in the whole sample (126 cm; 159, 122 cm; 179).

5.8.2.4 Assemblage zone 4 (AZ4) (110-106 cm)

AZ4 spans a short depth interval (110-106 cm) with distinct changes in the faunal distribution. *C. reniforme* and *E. excavatum* clearly prevail over all other species in this assemblage (49 % and 38 %) (Fig. 17). This is the oldest assemblage where *E. excavatum* is so abundant. Most notably *S. loeblichi*, *C. lobatulus* and *Buccella* spp. are absent from this interval (Fig. 17). *N. labradorica* is moderately abundant (7 %) and extremely minor contributions from *C. neoteretis* (2 %) and *I. norcrossi* (2%) are observed. *A. gallowayi* is absent from this zone (Fig. 17).

As with the lower assemblage zones (AZ1-AZ3) the concentration, accumulation rate of benthic foraminifera and percentage of fragmentation is extremely low (107 g^{-1}; 425 cm^{2} ky^{-1}; 9 %). The assemblage was 100 % calcareous species and the species diversity is low with 11 species in the sample (Fig. 16).

5.8.2.5 Assemblage zone 5 (AZ5) (106-74 cm)

AZ5 is characterised by a large shift in the foraminiferal distribution. *C. reniforme* is still the most abundant species with an average relative abundance of 56 % throughout the zone, with a maximum peak at 86 cm of 67 % (Fig. 17). The relative abundance of *E. excavatum* has considerably decreased compared to the lower assemblage zones (4-12 %). *N. labradorica* is moderately abundant shifting between 5-17 % (Fig. 17). The following species fluctuate between absent and moderate abundances; *I. norcrossi* (1-10 %), *C. neoteretis* (2-9 %), *E. subarcticum* (2-8 %), *C. lobatulus* (1-8 %), *M. barleeanus* (2-5 %), *A. gallowayi* (1-4 %), *Cassidulina*/*Islandiella* spp. (0-6%), *Buccella* spp. (0-3 %) and *S. loeblichi* (0-2 %) (Fig. 17).

A large increase in all measured parameters is observed in this zone. The foraminifera concentration and accumulation rate increases to 551 g^{-1} and 1058 cm^{2} ky^{-1} at the base, peaking at 78 cm (1764 g^{-1}; 8126 cm^{2} ky^{-1}) before slightly decreasing at 74 cm. Agglutinated species are not present in this zone. The percentage of fragmentation increases sharply, with more stable values between 33-47 %. The appearance of foraminifera in the 0.5-1 mm grain size fraction occurs in AZ5 with 1-9 g^{-1} (Fig. 16).

5.8.2.6 Assemblage zone 6 (AZ6) (74-30 cm)

The relative abundance of *C. reniforme* is slightly lower in this zone with a general decreasing trend 48-42 %. *E. excavatum* is slightly increased in relative abundance (8-15 %), whereas the relative abundance of *N. labradorica* is marginally decreased (2-13 %) (Fig. 17). The relative abundance of *I. norcrossi* is higher in this zone, shifting between 4-11 %, with the occasional presence of *M. barleeanus* at the base of this zone (2-5 %). Distinct fluctuations are observed in *E. subarcticum*, *C. neoteretis* and *Buccella* spp. *E. subarcticum* ranges between 3-11 %, with notable peaks at 58 cm (11 %) and 50-38 cm (8-10 %) (Fig. 17). Fluctuations in the relative abundance of *C. neoteretis* (1-13 %) and *Buccella* spp. (1-4

%) appear to show a similar relationship. *C. lobatulus*, *S. loeblichi* and *A. gallowayi* are minor contributors in AZ5 (<4 %; <2 %; <2 %). The relative abundance of *Cassidulina*/*Islandiella* spp. fluctuates between 0-7 % in this zone (Fig. 17).

The concentration and accumulation rate of benthic foraminifera have an overall decreasing trend (1656-411 g^{-1}; 6990-2284 cm^2 ky^{-1}). The assemblage is very diverse (15-23 species) and it is entirely composed of calcareous species. The percentage of fragmentation is moderate in this zone 22-37 % except for a peak between 46-54 cm (44-49 %). Foraminifera still occur in low concentrations in the 0.5-1 mm grain size fraction (1-6 g^{-1}) (Fig. 16).

5.8.2.7 Assemblage zone 7 (AZ7) (30-0 cm)

AZ7 is characterised by a marginal decrease in relative abundance of *C. reniforme* (29-38 %) and a slight increase in *E. excavatum* (12-23 %). *I. norcrossi* is moderately abundant (7-16 %) alongside *N. labradorica* (3-11 %) (Fig. 17). There are minor contributions to the assemblage from *E. subarcticum* (<5 %), *M. barleeanus* (<3 %), *C. neoteretis* (<3 %), *C. lobatulus* (<2 %). There is a constant occurrence of *S. loeblichi* (1-4 %), *Buccella* spp. (1-4 %) and *A. gallowayi* (1-3 %) (Fig. 17).

Agglutinated species account for 3-14 % of the assemblage in this zone (Fig. 16). *A. glomerata* is the most abundant agglutinated species (1-9 %) (Fig. 17) and there are extremely minor contributions from *Reophax* spp, *C. crassimargo*, *Deuterammina orchracea* and *R. turbinatus*. The abundance of *Cassidulina*/*Islandiella* spp. shows an overall increasing trend from 0-6 % in AZ7 (Fig. 17).

The decreasing trend of the concentration and accumulation rate of benthic foraminifera continues in this zone (476-251 g^{-1}; 2847-1312 cm^2 ky^{-1}). The percentage of fragmentation is variable in this zone between 22-42 %. The species diversity remains high in this zone (14-23 species) and the foraminifera in the 0.5-1 mm grain size fraction are in low concentrations (1-5 g^{-1}) (Fig. 16).

5.8.3 Planktonic foraminifera

The accumulation rate and concentration of planktonic foraminifera is low in the upper 102 cm of core HH13-26 (10-276 cm^2 ky^{-1}; 2-60 g^{-1}) (Fig. 18), below this the presence of planktonic specimens is extremely rare or absent.

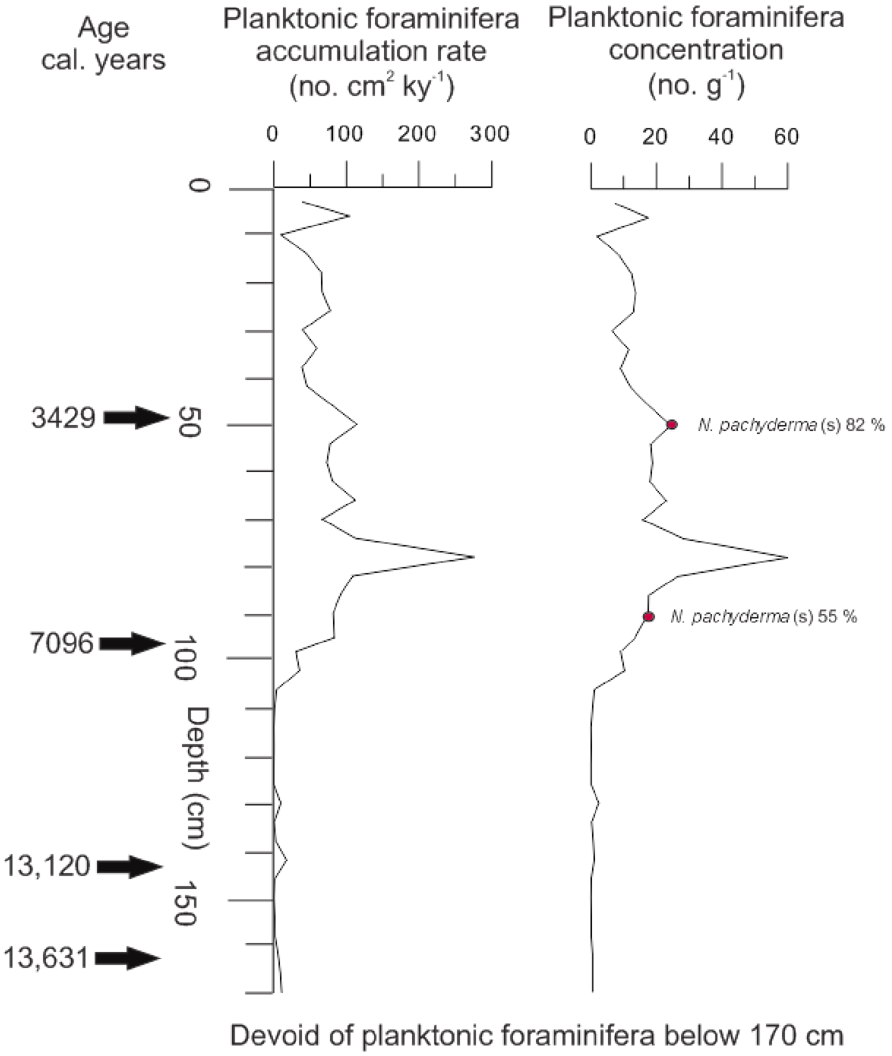

Figure 18: Planktonic foraminifera accumulation rate and concentration plotted against depth, with radiocarbon ages in calendar years and the relative abundance of N. pachyderma (s) indicated.

The distribution of planktonic foraminiferal species was investigated, however only three samples (49-50 cm; 89-90 cm; 97-98 cm) yielded >100 specimens for identification. The planktonic foraminiferal assemblage is predominantly composed of the polar species *Neogloboquadrina pachyderma* (sinistral), and sub-polar species *Neogloboquadrina pachyderma* (dextral), *Turborotalita quinqueloba* and *Globigerina*/*Globigerinita* spp.

N. pachyderma (s) was most dominant (82 %) at 49-50 cm. *T. quinqueloba* had a relative abundance of 17 % and *Globigerina*/*Globigerinita* spp. was extremely rare (1 %) (Fig. 18).

The planktonic assemblage composition changes slightly at 89-90 cm. *N. pachyderma* (s) still dominates the assemblage with a relative abundance of 55 %. Sub-polar species are more persistent and diverse at this depth; *Globigerina*/*Globigerinita* spp. (17%), *T. quinqueloba* (16 %) and *N. pachyderma* (d) (12%) (Fig. 18).

Many of the specimens in the sample from 97-98 cm were unfortunately broken after picking before identification could be performed. Of the species that could be identified, the assemblage was composed of a mixture of polar species *N. pachyderma* (s) and sub-polar species *N. pachyderma* (d), *Globigerina*/*Globigerinita* spp. and *T. quinqueloba*.

6. Interpretation and Discussion

The studied sediment core HH13-26 will be interpreted and discussed concerning the LGM and the early deglaciation, based on the results of the multibeam and acoustic survey, age model and sedimentological composition (Fig. 7-8; 20). The age model, prominent changes in sedimentology, stable isotopes of benthic foraminifera, relative abundance and accumulation rate of foraminifera (Fig. 20, 22-25) will be used to interpret and discuss the palaeooceanographic and palaeoenvironmental conditions that prevailed after the early deglacial period. Sedimentological records from areas adjacent to core HH13-26, the central and outer Storfjorden Trough will also be discussed (Fig. 19).

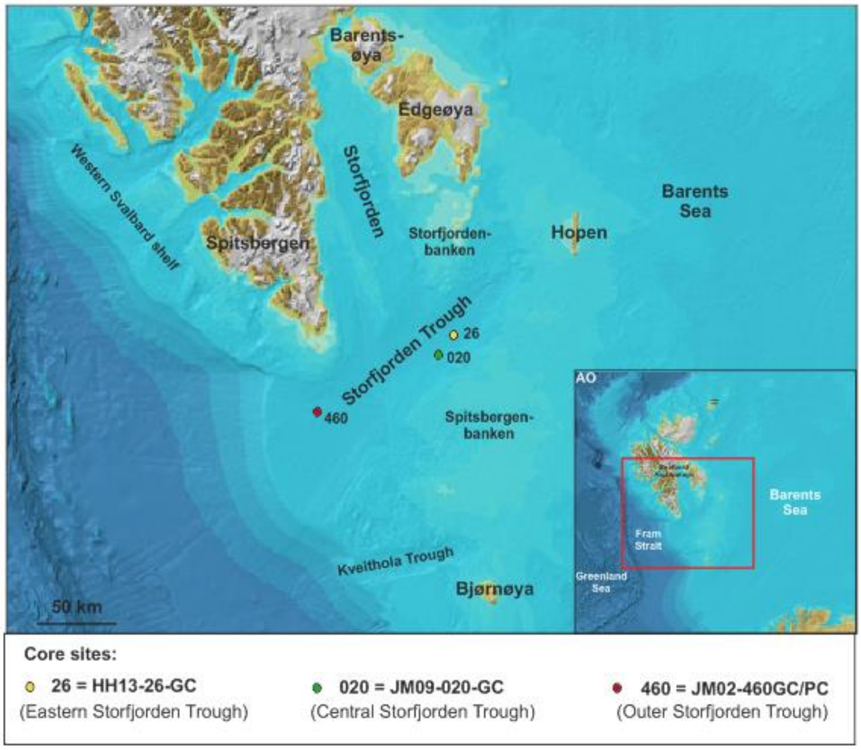

Figure 19: Map of the Svalbard Archipelago based on the International Bathymetric Chart of the Arctic Ocean (IBCAO) Version 3.0 (Jakobsson et al., 2012) with the core locations of HH13-26, JM09-020-GC, JM02-460GC/PC in the Storfjorden Trough marked. AO = Arctic Ocean.

The chronology of the core has been subdivided into five units based on the parameters listed above of the following time intervals: the early deglaciation (<14,000 cal. years), the Allerød interstadial, including the Allerød-Younger Dryas Transition and the Younger Dryas (c. 13,800– 11,500 cal. years), the early Holocene (c. 11,500-8200 cal. years), the mid-Holocene (c. 8200-4000 cal. years) and the late Holocene (the last c. 4000 cal. years).

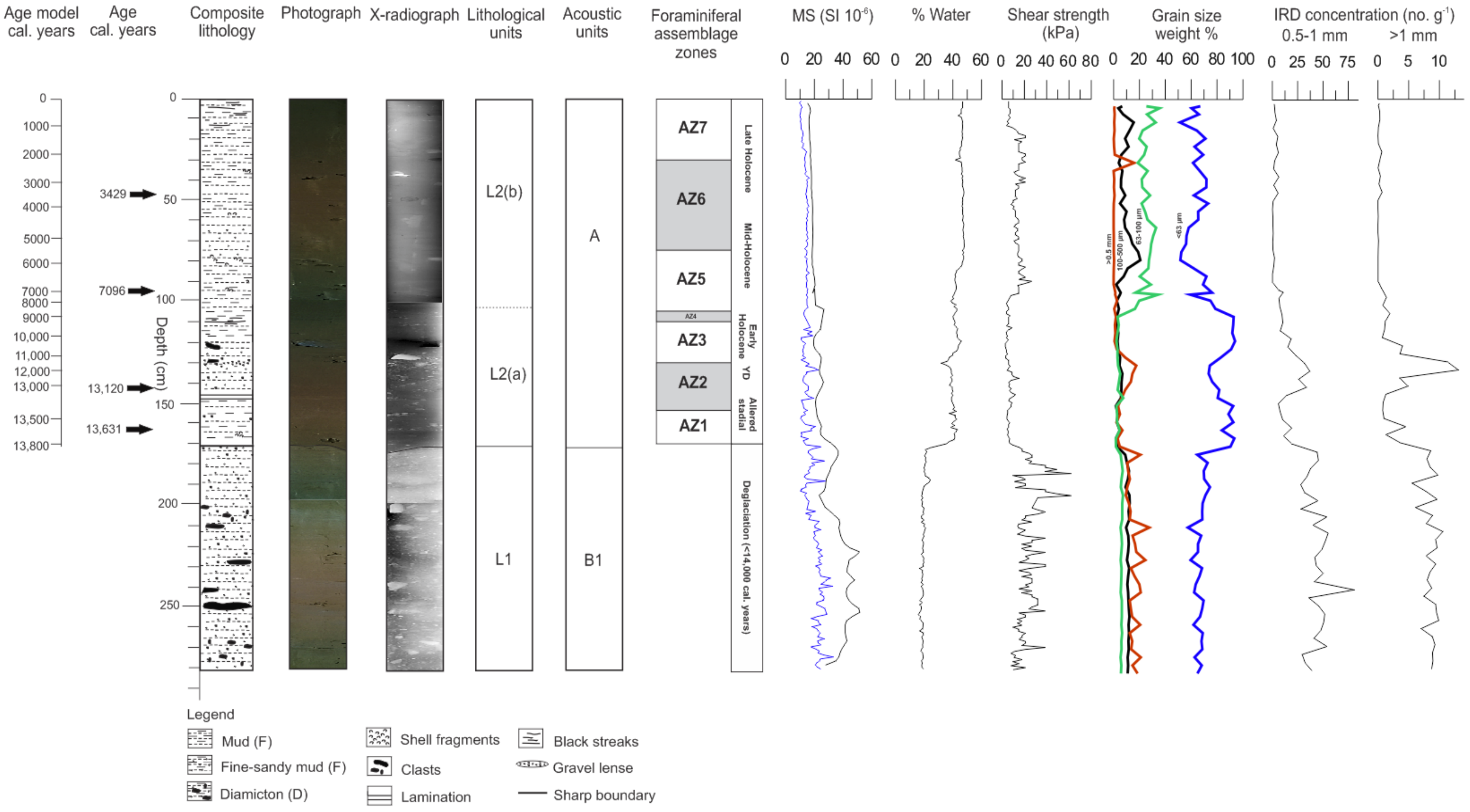

Figure 20: Age model, composite lithological log with radiocarbon dates in calendar years indicated, photograph, x-radiograph image, assigned lithological and acoustic units, foraminiferal assemblage zones, magnetic susceptibility, % water, shear strength, grain size weight % and IRD concentration of 0.5-1 mm and >1 mm fraction, with respect to the time zones discussed.

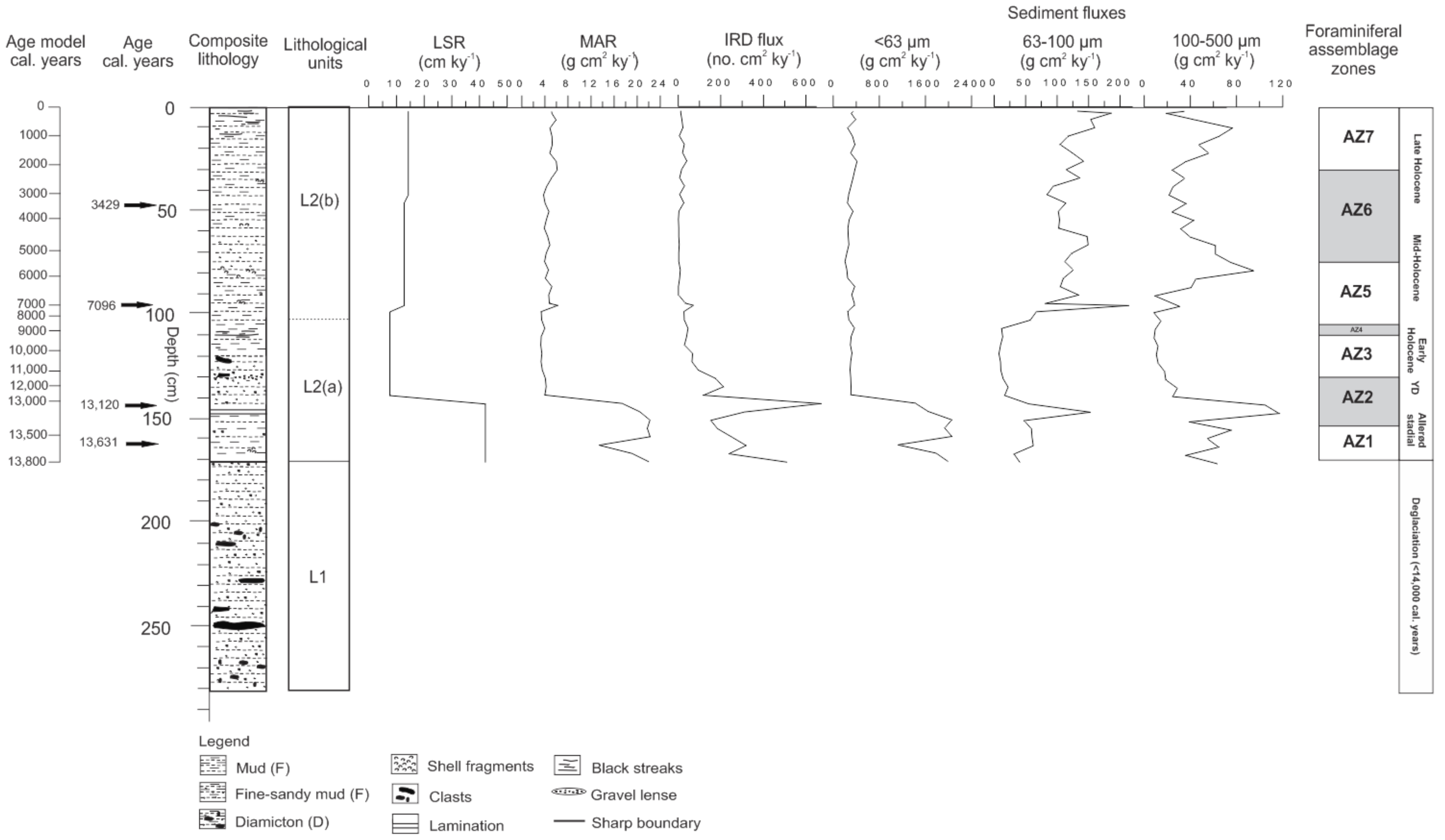

Figure 21: Age model, composite lithological log with radiocarbon dates in calendar years indicated, lithological units, linear sedimentation rates, mass accumulation rates, IRD flux, sediment flux of the various grain sizes, foraminiferal assemblage zones, with respect to the time intervals discussed.

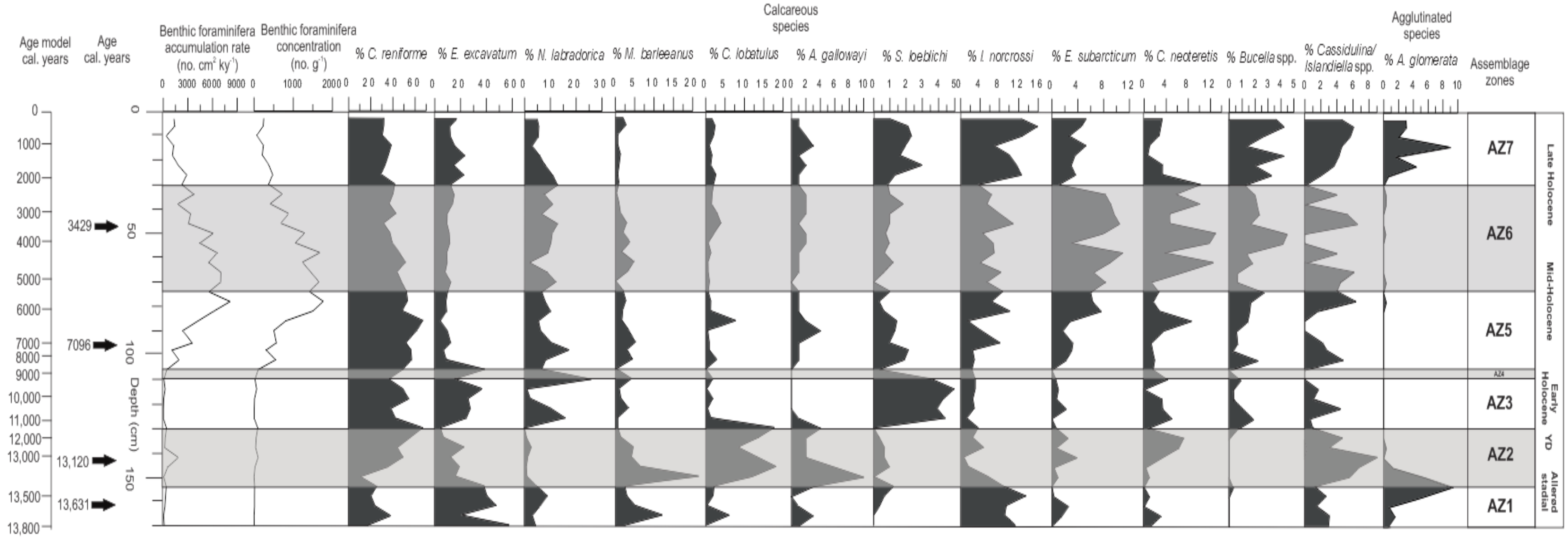

Benthic foraminifera are rare or absent below 170 cm.

Figure 22: Age model and radiocarbon dates in calendar years indicated, benthic foraminifera accumulation rate and concentration, relative abundance of dominant benthic species plotted versus depth, assemblage zones, with respect to the time intervals discussed.

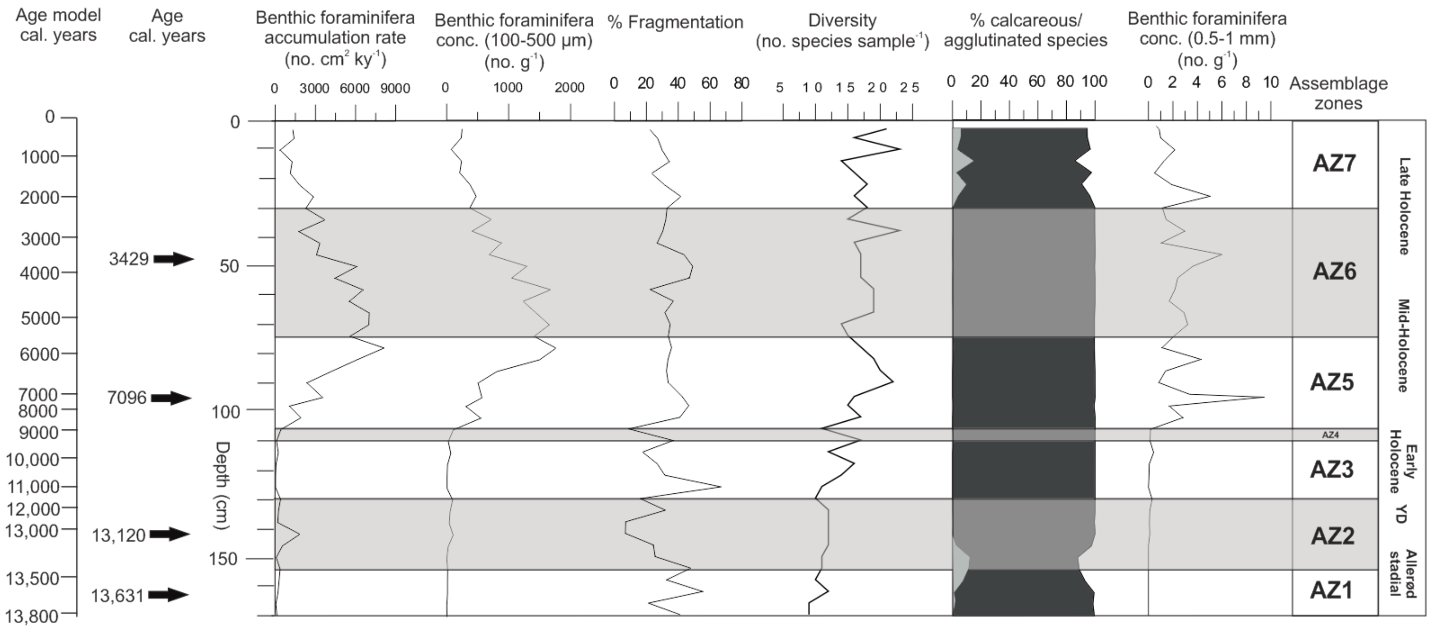

Benthic foraminifera are rare or absent below 170 cm.

Figure 23: Age model and radiocarbon dates in calendar years indicated, benthic foraminifera accumulation rate and concentration, percentage of fragmentation, diversity, % calcareous/agglutinated specimens, benthic foraminifera concentration for the 0.5-1mm size fraction plotted versus depth, assemblage zones, with respect to the time intervals discussed.

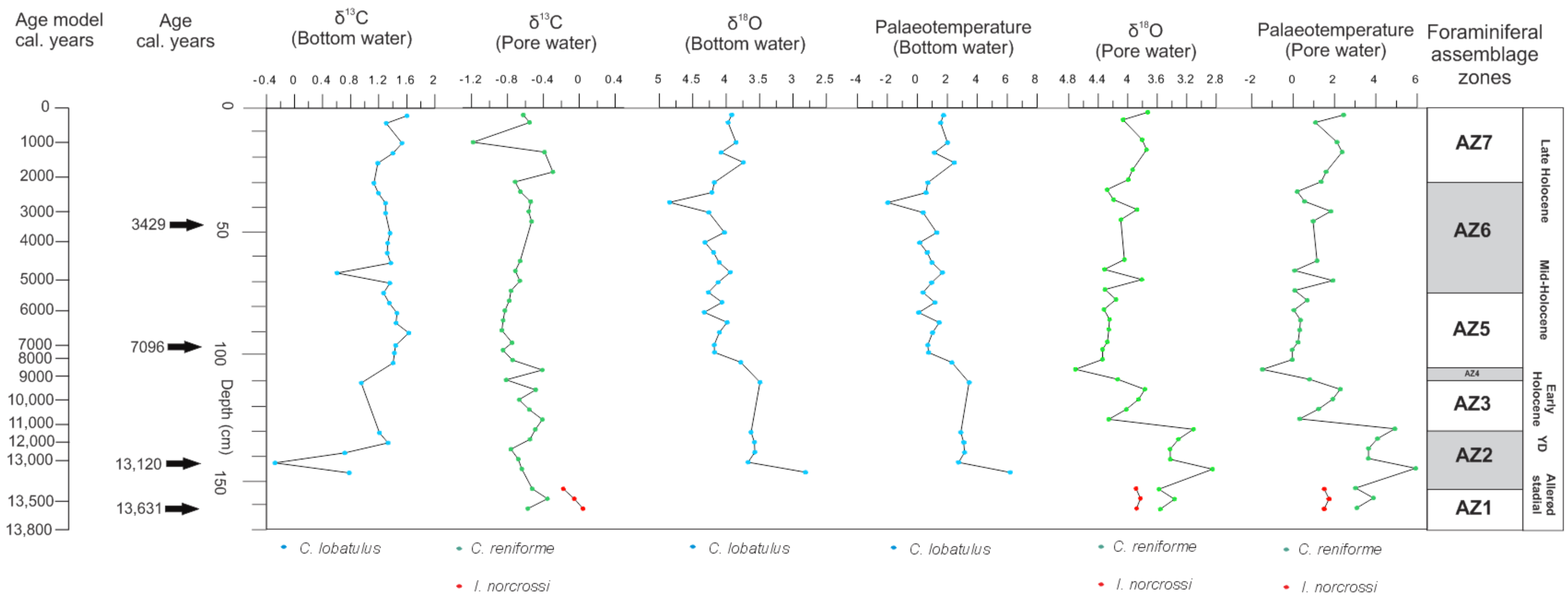

Figure 24: Age model and radiocarbon dates in calendar years indicates, measurements of stable isotopes of $\delta^{13}C$ and $\delta^{18}O$ and calculated palaeotemperatures from benthic foraminifera species C. lobatulus, C. reniforme and I. norcrossi, with respect to the foraminiferal assemblage zones and the time intervals discussed.

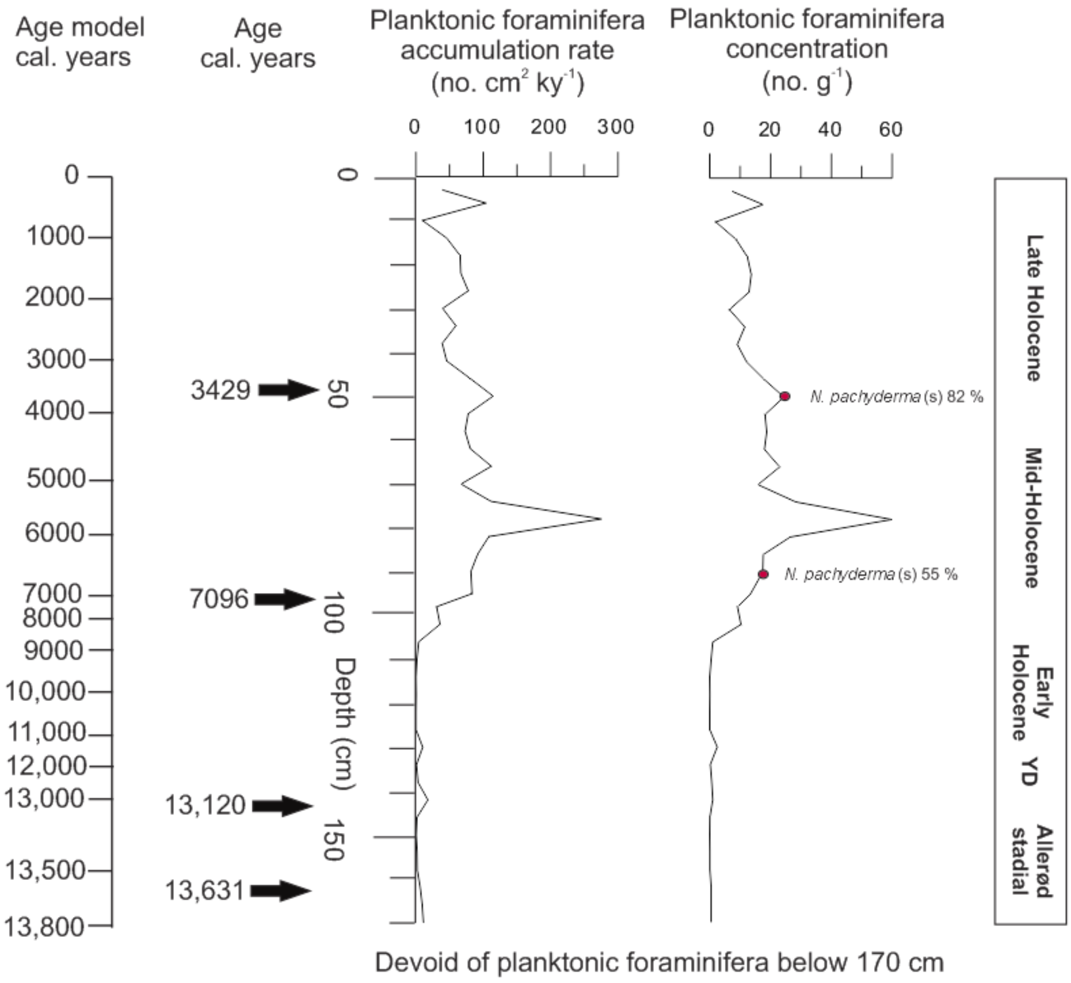

Figure 25: Age model with radiocarbon dates in calendar years indicated. Planktonic foraminifera accumulation rate and concentration with respect to the time intervals discussed.

6.1 Last Glacial Maximum and early deglaciation (<14,000 cal. years)

The Storfjorden Trough on the northwest Barents shelf was host to a large fast-flowing ice stream that was draining the SBIS during the last glaciation (e.g., Elverhøi et al., 1998; Landvik et al., 1998; Ottesen et al., 2005) (Fig. 26). The Storfjorden Trough Mouth Fan (TMF) on the continental slope acted one of the sediment depo-centres for the SBIS. The Storfjorden TMF combined with sediment ridges interpreted as moraines have provided evidence of palaeo-ice flow within the Storfjorden Trough during the LGM and previous glaciations (Elverhøi et al., 1993: Laberg and Vorren, 1996; Hjelstuen et al, 1996).

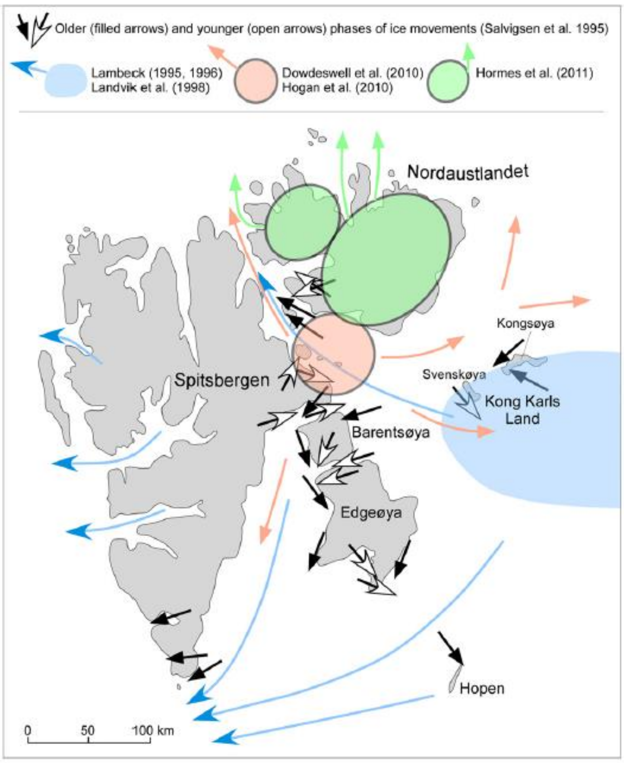

Figure 26: Proposed ice-sheet domes and reconstructed ice-flow directions from LGM and subsequent deglaciation. Modified by Ingólfsson and Landvik. (2013) from Salvigsen et al. (1995); Hogan et al. (2010) and Hormes et al. (2011).

.

The direction of ice flow through the Storfjorden Trough has been proposed as being primarily from an east to west direction draining a catchment located in the north eastern Barents Sea (Landvik et al., 1998; Ottesen et al., 2005) (Fig. 26). Evidence from terrestrial and marine landforms indicates the presence of multiple ice domes draining through various palaeo-ice streams (Fig. 26). Ice-domes have been suggested to have been present over Kong Karls Land, Nordaustlandet, eastern Spitsbergen, Barentsøya, Edgeøya and southern Hinlopen (Lambeck 1995; 1996; Salvigsen et al., 1995; Landvik et al., 1998; Dowdeswell et al., 2010; Hogan et al., 2010; Hormes et al., 2013; Ingólfsson and Landvik, 2013) (Fig. 26). However, it is not known if these domes were confluent during the same period of time or if there were spatial and temporal shifts in the configuration of the ice sheet during its advance and retreat (Ingólfsson and Landvik et al., 2013).

Models have predicted that the north eastern Barents Sea was depressed under an ice sheet that was >2000 m-thick and that this region has undergone the greatest isostatic uplift following the deglaciation of the SBIS (Bondevik, 1993; Forman et al., 1995; Landvik et al., 1998) (Fig. 27).

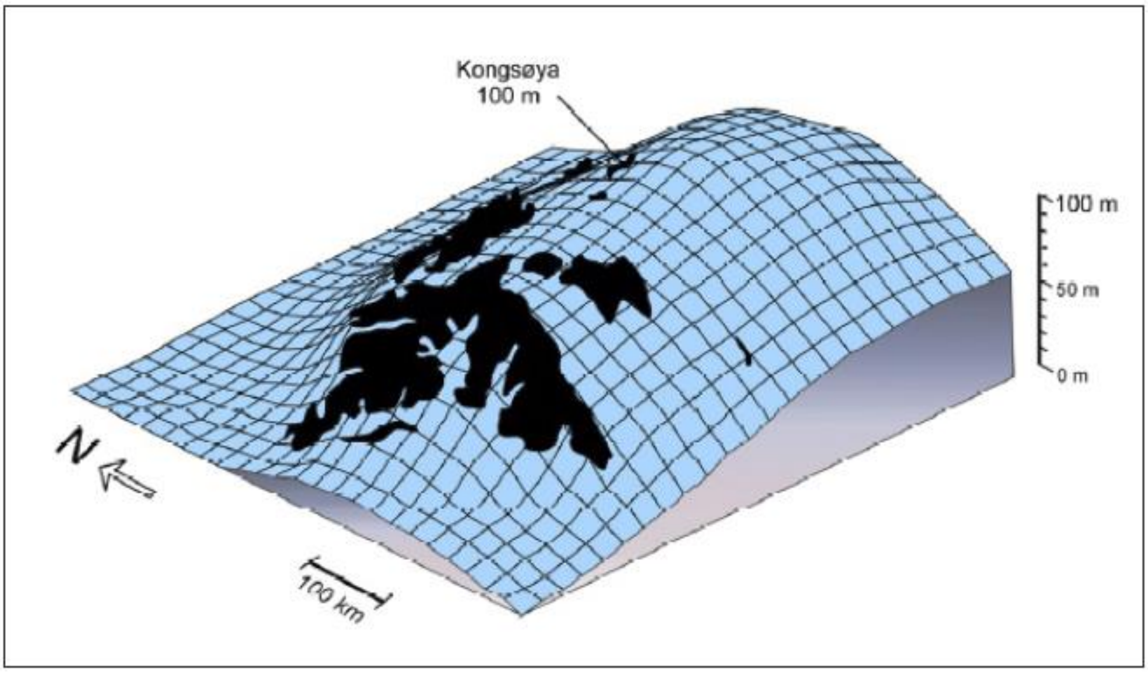

Figure 27: Postglacial isostatic rebound since 10 ^{14}C ky caused by the isostatic depression from the SBIS. Modified by Ingólfsson and Landvik. (2013) from Bondevik. (1993).

The continental slope at the mouth of the Storfjorden Trough is composed of depositional lobes of glacigenic debris flows leading to the build-up of the TMF (Fig. 28), dating back to when the grounding line of the SBIS reached the shelf edge during the LGM c. 24-23,000 cal. years (Laberg and Vorren, 1996; Mangerud et al., 1998; Jessen et al., 2010).

Three wide sediment lobes have been described as part of the Storfjorden TMF system, with various styles of sedimentation (Fig. 28), suggesting that the ice stream behaviour was even more dynamic within the Storfjorden Trough than previously thought (Ottesen et al., 2005; Pedrosa et al., 2011). The current hypothesis is that ice streams flowed within the trough and sediment deposition at the TMF was not uniform. It has been proposed that the Storfjorden Trough was under the influence of multiple sub-ice streams with drainage from different catchment areas (Lucchi et al., 2012; 2013; Pedrosa et al., 2011) (Fig. 28).

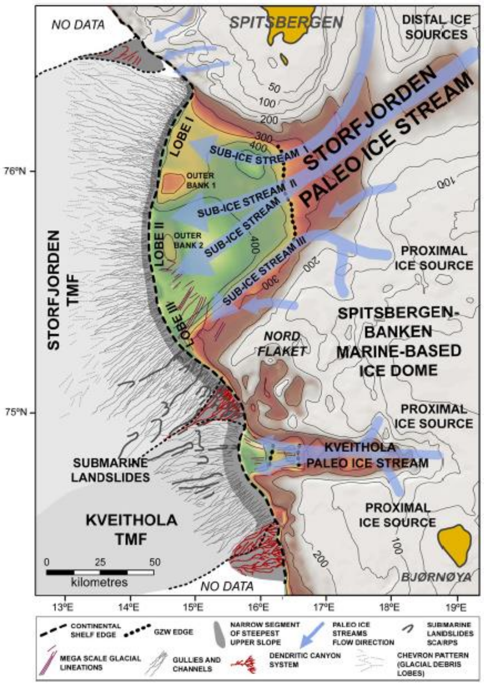

Figure 28: Morphological characteristics of the Storfjorden and Kveithola TMF systems. Shaded relief bathymetry based on the International Bathymetric Chart of the Arctic Ocean (IBCAO) after Jakobsson et al. (2008) and a grid produced by the Geological Survey of Norway from Ottesen et al. (2006).

Sub-ice stream I is suggested to have drained ice sources from the northeast and flowed through the inner basin of Storfjorden and the northern part of the Storfjorden Trough, which led to the deposition of the northernmost sediment lobe I (Fig. 28). Sub-ice stream II is suggested to have been split by a shallow bank on the outer shelf, contributing to deposition of sediment lobe II. Sub-ice stream II is the largest of the sub-ice streams and is thought to have flowed from sources in the east (Pedrosa et al., 2011) (Fig. 28). Sub-ice streams I and II are believed to have been under the influence of thick and perhaps fast-flowing ice from distal sources (Pedrosa et al., 2011). Core site HH13-26 is suggested to have been under the influence of this largest sub-ice stream II in the Storfjorden Trough (Fig. 29b).

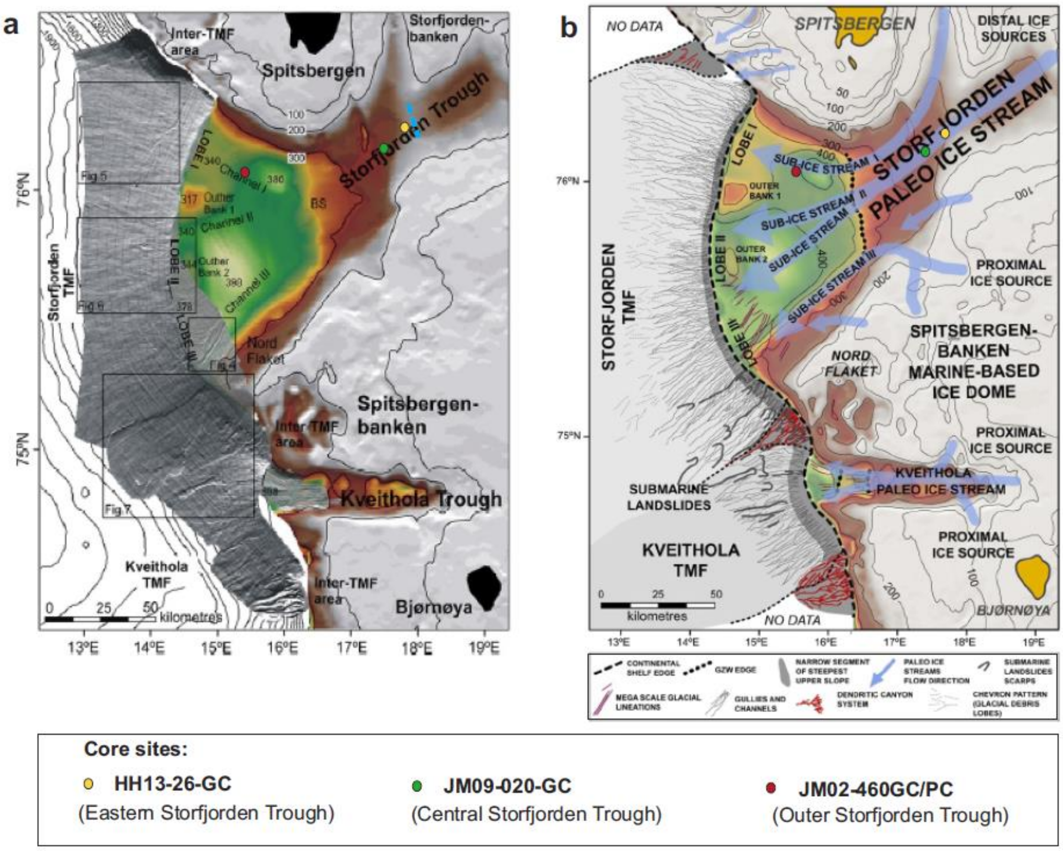

Figure 29: Morphological features of the Storfjorden Trough with core locations HH13-26; JM09-020-GC; JM02-460GC/PC. (a) Proposed change in bathymetry in the eastern Storfjorden Trough and possible grounding line of the ice front indicated by the blue dashed line. (b) Core sites HH13-26; JM09-020-GC; JM02-460GC/PC are shown under the influence of the proposed palaeo-ice streams and ice catchment areas. Modified from Pedrosa et al. (2011).

Sub-ice stream III is proposed to have been under different depositional processes during deglaciation as it was draining more proximal ice sources from a local marine-based ice dome on Spitsbergenbanken (Elverhøi et al., 1993; Rebesco et al., 2011) (Fig. 28).

Records from cores JM02-460PC suggest that the outer part of the Storfjorden Trough (Fig. 19; 29) was deglaciated prior to c. 19,700 cal. years (Rasmussen et al., 2007). The inner Storfjorden basin deglaciated by the start of the Holocene by c. 11,700 cal. years (Rasmussen and Thomsen, 2015). There are limited data from the central and eastern part of the Storfjorden Trough, however one AMS ^{14}C dated core (JM09-020-GC) from central Storfjorden (Fig. 19; 29) suggests that it was ice-free before c. 13,950 cal. years (Łącka et al., 2015).

Lithological unit L1 in the oldest part of the core HH13-26 (<14,000 cal. years) consists of dark grey, compact, poorly sorted sediments composed of gravel to cobble-sized clasts in a fine-sandy mud matrix (Fig. 20). L1 was almost devoid of foraminifera with the few specimens that were present were of poor preservation and showed signs of being re-worked. The magnetic susceptibly and shear strength are high and variable (23.3-51.6 SI 10^{-6}; 11-62 kPa), with a low water content (<24 %), which is typical of sediments that are indicative of glacigenic debris flows and/or glacial activity (e.g., Laberg and Vorren et al., 1996) (Fig. 20).

The multibeam and acoustic images show that HH13-26 was recovered from the margin of a prominent sedimentary protrusion in the eastern sector of the Storfjorden Trough (Fig. 7-8). The large protrusion observed is interpreted to be a well-developed glacially derived lobe, due to the sediment composition and acoustic characteristics of acoustic unit B1 (Fig. 8; 20; Table 6). The acoustic unit B1 is interpreted to relate to lithological unit L1 (Fig. 20).

Acoustic unit B and B1 are inferred to be composed of similar glacially derived material due to the high amplitude and chaotic nature of the acoustic reflections (Fig. 8), but deposited in a different style (Table 6). Acoustic unit B is situated west of B1 and is interpreted as a separate acoustic unit due to the reflections terminating at the start of B1, where the margin of the glacial lobe is located (Fig. 7-8). Perhaps unit B was deposited first by meltwater inputs during the rapid retreat of sub-ice stream II in this area, which is inferred from the stratified layers of various densities (Fig. 8; 29b; Table 6).

The initial retreat of sub-ice stream II to an area adjacent to the core site HH13-26 (Fig. 29a) may have occurred during the Bølling interstadial c. 14,700 cal. years, depositing unit B in response to warming during this period. However, dates from this sequence would need to be obtained to constrain this theory.

The rapid retreat and subsequent release of sediment laden meltwater plumes depositing fine-grained, laminated sediments during the Bølling interstadial has been documented in the outer portion of the Storfjorden Trough in two AMS ^{14}C dated cores, JM02-460GC/PC (Rasmussen et al., 2007) (Fig. 19; 29). The proposed meltwater deposits from acoustic unit B are not observed in unit B1, this is likely due to the fact the glacial lobe was deposited during a different glacial process, where it pushed and subsequently transported the deposits of unit B westward. This could explain why the deposits in B1 appear to be built up and thicker close to the margin of B1 (Fig. 8).

Acoustic unit A overlies B and B1 as a homogenous, continuous layer and is interpreted to represent marine deposits in lithological unit L2 (Fig. 8; 20). The mapped area does not cover the entire glacial lobe, therefore it is not known the exact size or how the geomorphology appears further to the north, south and east.

The bathymetry of the Storfjorden Trough is shallower (<200 m) with steep isobaths in the area east of the HH13-26 (Fig. 29). The possibility that during the eastward retreat of sub-ice stream II there was a still-stand of the grounding line of sub-ice stream II proximal to core site HH13-26 is considered (Fig. 29a; 30b). The cause of this still-stand is not known, but is likely due to the change in the bathymetry (Fig. 29), possibly combined with isostatic uplift, which is proposed to have been greatest in the eastern Barents Sea (Bondevik, 1993; Forman et al., 1995).

The large ice sheets during the LGM are proposed to have caused global sea level lower by 120 m (Fairbanks, 1989). The sea level may have been too low <14,000 cal. years to influence the melting of the ice front at this location (Fig. 30b-c). This is supported by Siegert and Dowdeswell (2002) proposing that ice retreated from the deeper bathymetric troughs first and a large embayment of ice grew around them. Łącka et al. (2015) suggest that the central Storfjorden Trough could have acted as an embayment during deglaciation.

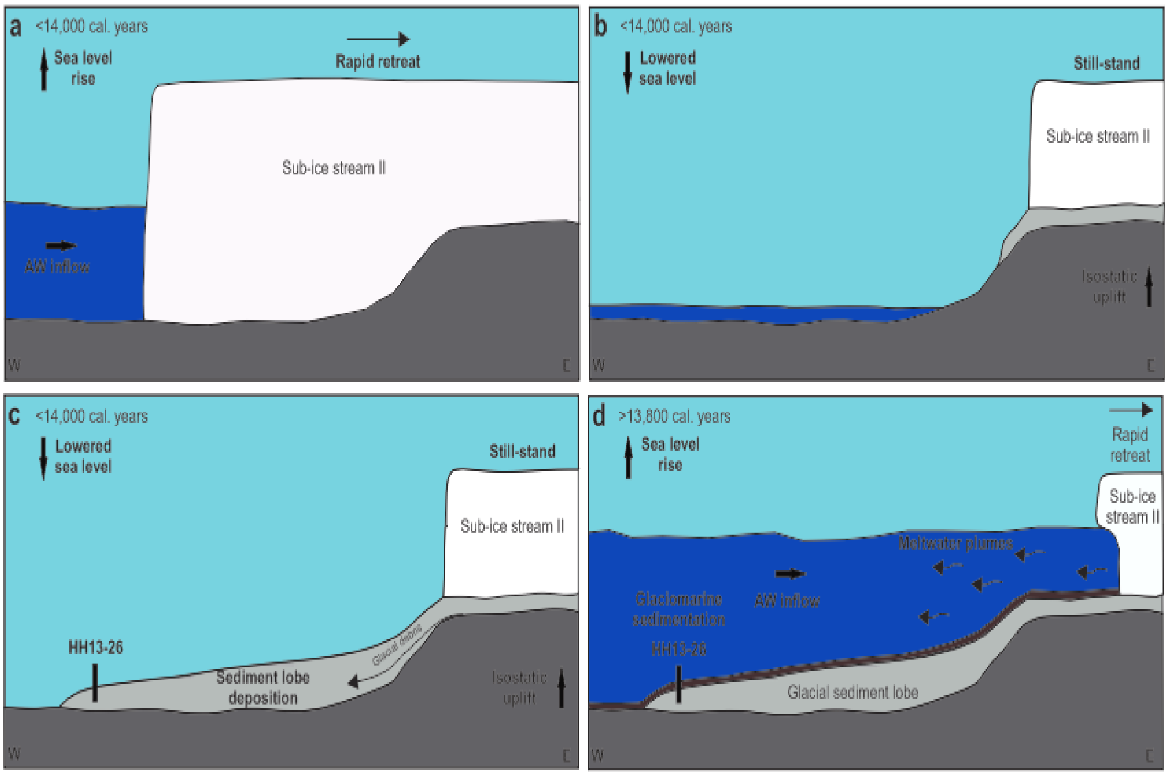

Figure 30: Schematics of proposed scenario of a still-stand of the grounding line of sub-ice steam II (a) initial rapid retreat in response to Atlantic Water inflow and/or sea level rise. (b) initial still-stand of the grounding line caused by the change in bathymetry combined with possible effects of isostatic uplift and a lowered sea level. (c) still-stand of the grounding line proximal to the location of core HH13-26 and subsequent deposition of the sediment lobe with the possible effects of isostatic uplift and lowered sea level (d) rapid retreat of the grounding line in response to Atlantic Water inflow and onset of glaciomarine sedimentation from meltwater plumes. AW = Atlantic Water.

Pedrosa et al. (2011) note a 'bathymetric step' and the presence of a grounding zone wedge (GZW) on the outer shelf (Fig. 29) and that it indicates a similar still-stand during the first stage of retreat of the ice streams. Although Pedrosa et al. (2011) show no data of the GZW, the bathymetry of the seafloor clearly shows the change in depth of this 'bathymetric step' (Fig. 29). The area where the proposed GZW is located has been thoroughly surveyed, however none of these data have been published yet.

We propose that during the still-stand sub-ice stream II continuously supplied vast quantities of glacial debris downslope from the east to the core site, which led to the deposition of the glacial sediment lobe through similar processes to those that occurred on the continental slope during the LGM (e.g., Laberg and Vorren et al., 1996) (Fig. 30). This east to west mode of transportation is supported by the thickness of the lobe is ~25 m-thick towards the east and is ~12 m-thick towards at the core site HH13-26 near the margin on the west (Table 6).

The possibility of a glacial re-advance was also explored (Fig. 31). Sub-ice stream II may have initially retreated further than previously estimated to a more distal setting during the early stages of deglaciation and subsequently re-advanced (Fig. 31 b-c). The driving mechanism of this proposed re-advance could have been through basal melting of the grounding line during the Bølling interstadial at c. 14,700 cal. years. The basal melting of sub-ice-stream II combined with isostatic uplift in the east may have provided the lubrication to cause it to re-advance downslope to a location proximal to core site HH13-26 and lead to the deposition of the glacial lobe (Fig. 31c).

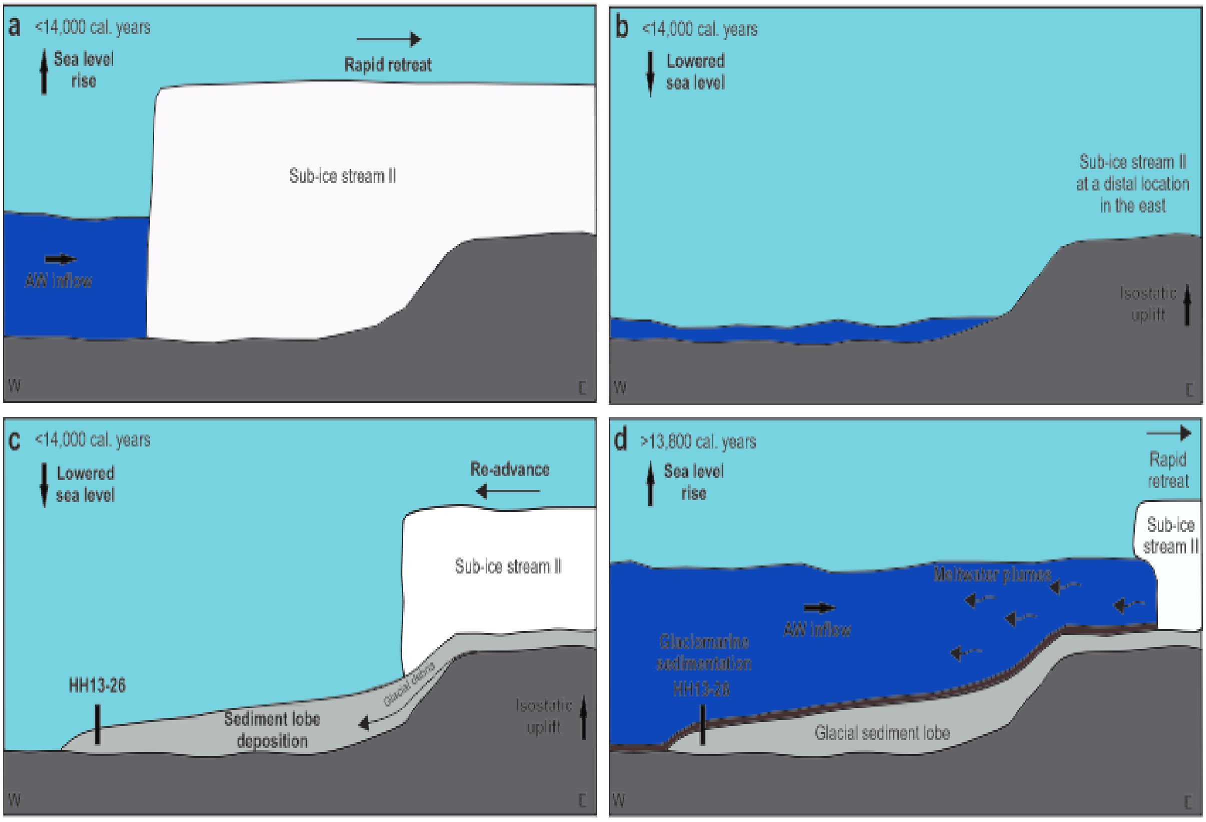

Figure 31: Schematics of proposed scenario of a re-advance of the grounding line of sub-ice steam II (a) initial rapid retreat in response to Atlantic Water inflow and/or sea level rise. (b) the grounding line location in a distal location in the east due to the possible effects of isostatic uplift and a lowered sea level. (c) re-advance of the grounding line to a proximal location to core site HH13-26 and subsequent deposition of the sediment lobe, with the combined effects of isostatic uplift and a lowered sea level (d) rapid retreat of the grounding line in response to Atlantic Water inflow and onset of glaciomarine sedimentation from meltwater plumes.AW = Atlantic Water.

There are no data further east in the Storfjorden Trough to provide supporting evidence for either hypothesis regarding either a still-stand during retreat or a re-advance of the grounding line. However, it is clear that the glacial lobe must have been deposited under a glacier proximal setting, due to the sedimentological composition (Fig. 20).

The oldest AMS ^{14}C date obtained in the marine sediments above the diamict in L1 suggest that the minimum age of the glacial lobe is c. 13,800 cal. years (Fig. 20). The age model presented by Łącka et al. (2015) for the core JM09-020-GC recovered near to HH13-26 (Fig. 19) is based on the assumption of linear sediment accumulation rates between the AMS ^{14}C data points. Łącka et al. (2015) propose that JM09-020-GC has a sedimentary unit that was deposited sub-glacially before c. 13,450 cal. years. This date was derived from a bivalve shell fragment within the 'sub-glacial unit' which gave an age of c. 13,950 cal. years. The presence of benthic species living sub-glacially is highly unlikely, according to Dunton. (1992), as aerial exposure of continental shelves in the Arctic during the last glaciation almost eliminated all benthic assemblages. Dayton et al. (1994) note that the presence of ice sheets on the shelves would prevent any shallow water assemblage to inhabit these areas and that recolonization of the benthos occurred between c. 14,000-6000 cal. years (Dunton, 1992). The grounding line of the ice stream may have lifted at c. 13,950 cal. years at the core site JM09-020-GC and a floating ice shelf could have allowed colonisation of the benthos. Considering this, the interpretation presented by Łącka et al. (2015) that the shell was deposited sub-glacially would be incorrect and it would be a sub-ice shelf environment.

A more plausible scenario is that the bivalve shell fragment was re-deposited from the sediments above, possibly during the coring process or when splitting the core. Articulated shells are more likely to be preserved in situ and yield accurate AMS ^{14}C dates rather than shell fragments that have probably been re-deposited (Bondevik et al., 2006). Łącka et al. (2015) do note that all of their dates are from shell fragments and they could have been subject to re-deposition.

HH13-26 is situated approximately 12 km to the north east of JM09-020 (Fig. 19) and we propose that the grounding line had already retreated to the east of both core sites before c. 14,000 cal. years. Considering this, and the western location of JM09-020 (Fig. 19) it is improbable that the date from the sub-glacial unit of c. 13,900 cal. years and their suggestion that the transition from a sub-glacial to ice proximal setting occurred at c. 13,450 cal. years is accurate. The proposed date of retreat (< 14,000 cal. years) of sub-ice stream II are more precise than the date suggested by Łącka et al. (2015).

The large-scale streamlined grooves observed on the multibeam image (Fig. 7) are interpreted to be mega-scale glacial lineations (MSGL) that are deposited parallel to the past ice-flow direction. MSGL are evidence of former fast flowing ice and have subsequently been overprinted by the glacial sediment lobe (Ottesen et al., 2005; Ottesen and Dowdeswell. 2009) (Fig. 7).

The transition from sub-glacial to ice proximal setting at the core site HH13-26 and the adjacent areas before c. 14,000 cal. years is thought to have occurred fairly rapidly due to the presence of these MSGL (Fig. 7; 30a; 31a). If the retreat of sub-ice stream II over this area was slow it is believed that the evidence of these streamlined bedforms would have been completely eroded. Possibly the ice stream was not grounded at this time in response to rapid global sea level change and/or isostatic uplift, with a similar scenario been proposed in the close-by Kveithola Trough (Bondevik, 1993; Forman et al., 1995; Rebesco et al., 2011) (Fig. 29).

Following the rapid retreat of sub-ice stream II it may have become grounded again in response to bathymetric changes in the east of the Storfjorden Trough, which led to the proposed still-stand proximal to core site HH13-26 (Fig. 29).

There are no other published multibeam data from central and eastern Storfjorden Trough to support any models of retreat, however extensive multibeam surveys have been performed in this region which will hopefully resolve the nature of retreat of the SBIS in the Storfjorden Trough (e.g., Projects by Andreassen; Noormets; Rasmussen).

6.2 Allerød interstadial and the Younger Dryas (c. 13,800-11,500 cal. years)

The Bølling-Allerød interstadials (c. 14,700-12,900 cal. years) have been documented to be periods of Atlantic Water inflow and high sedimentation rates from meltwater supply. The Younger Dryas (c. 12,900-11,500 cal. years) is recognised as a short-term cold event of reduced Atlantic Water inflow and dominance of polar waters (e.g., Rasmussen et al., 2007; Ślubowska-Woldengen et al., 2007).

The age model presented suggests that any evidence of the Bølling interstadial is not recorded in the investigated core HH13-26 (Fig. 13), as the age of the onset of glaciomarine sedimentation is c. 13,800 cal. years (Fig. 20). The dominant sediment supply at the core site was likely still from glacigenic debris flows from sub-ice stream II, with little or no inflow of Atlantic Water during the Bølling interstadial.

The Allerød interstadial began c. 14,000 cal. years and appears to have changed the style and supply of sedimentation rapidly. A sharp boundary in sediment colour and composition is observed at 171 cm, the border between lithological unit L1 and L2(a) in core HH13-26 (Fig. 20), with the sediments changing from grey, coarse diamicton to dark grey, fine-grained mud with rare to abundant clasts. The magnetic susceptibility and shear strength are considerably lower than L1 (15.3-26.3 SI 10^{-6}; 4.1-27 kPa) and the water content is high (>32 %) (Fig. 20). The acoustic characteristics of units B1 and A (Fig. 8; Table 6), clearly shows the transition from high density material to homogenous material of a lower density. This indicates a rapid change in sedimentation style and supply, possibly due to a further retreat of sub-ice stream II and the onset of glaciomarine sedimentation in an ice proximal setting by c. 13,800 cal. years (Fig. 30d; 31d).

The very fine silty clay between 171-146 cm with a lamination observed between 148-147 cm (Fig. 20) is interpreted to be deposited by suspension settling from sediment-laden meltwater plumes emanating from sub-ice stream II between c. 13,800-13,200 cal. years (Fig. 30d; 31d). Sub-ice stream II may have been undergoing a rapid retreat in response to the inflow of Atlantic Water during the Allerød interstadial (Fig. 30a; 31a).

The retreat is interpreted to be rapid due to the high sedimentation rates in at this time with an average of 41.2 cm ky^{-1} estimated at c. 13,800-13,100 cal. years between 171-141 cm (Table 8). The mode of deposition of fine-grained laminated sediments from turbid meltwater plumes appears to have recorded during initial deglaciation during the different stages retreat of the ice streams within the Storfjorden Trough. Evidence of these meltwater deposits have been recorded on the continental slope, outer continental shelf and the central part of the Storfjorden Trough (Rasmussen et al., 2007; Lucchi et al., 2013; Łącka et al., 2015). The meltwater deposits during deglaciation appear to be wide-spread and have been documented along the western Svalbard and the northern Barents Sea (Hogan et al., 2010; Jessen et al., 2010; Klitgaard-Kristensen et al., 2013).

The proposed retreat is also thought to have been rapid as the multibeam image shows no signs of pronounced gully systems on the glacial sediment lobe (Fig. 8). Gullies are indicative of erosion from prolonged proximal meltwater input that would have incised the glacial sediment lobe, similar to processes that occurred on the outer slope (Pedrosa et al., 2011). It should still be considered that such gullies may have been present and subsequently filled in by Holocene hemipelagic sedimentation.

The appearance of benthic foraminifera and dominance of opportunistic species *E. excavatum*, *C. reniforme* (average relative abundance, 41 %; 25%) and a moderate occurrence of *I. norcrossi* (9-13 %) in AZ1 confirms the presence of a proximal ice sheet with decreased salinity in the early stages of the Allerød interstadial between c.13,800-13,400 cal. years (e.g., Hald and Korsun, 1997; Korsun and Hald, 1998) (Fig.22). AZ1 is characterised by a low concentration of benthic foraminifera (<16 g^{-1}) and low species diversity (<12 species) (Fig. 28), which indicate a highly unstable and stressed environment (Hald and Korsun, 1998). The preservation of benthic foraminifera is low, which is indicated from the percentage of fragmentation (22-55 %) (Fig. 23), suggesting the presence of cold corrosive bottom waters (Hald and Korsun, 1997). The occurrence of agglutinated species *A. glomerata* (5 %) (Fig. 22) suggests cold, fresh bottom waters, likely due to the presence of glacial meltwater (Hald and Korsun, 1997). A peak in *M. barleeanus* (21 %) at c. 13,300 cal. years and its increased relative abundance in AZ2 (2-5 %), indicate sedimentation of fine-grained muds and steady food supply (Fig. 20; 22). This is indicative of a stronger subsurface Atlantic Water inflow during these periods (e.g., Mackensen and Hald, 1988; Hald and Steinsund et al., 1992; Ślubowska et al., 2005; Rasmussen et al., 2007).

There is a shift in the foraminiferal species composition in AZ2 at 146 cm to a dominance of *C. reniforme* over *E. excavatum* (average relative abundance, 43 %; 14 %) (Fig. 22), which suggests that bottom water conditions slightly improved with a lesser influence of sediment-laden meltwater by c. 13,200 cal. years (Hald and Korsun, 1997). The accumulation rate of benthic foraminifera increases (527-1841 cm^2 ky^{-1}) during this time (Fig. 23) and can be linked to the improved environmental conditions and subsequent higher productivity. The sedimentology changes to coarser fine sandy silt with clasts and the sedimentation rate decreases to 7.6 cm ky^{-1} (Fig. 20; Table 8) during the latter portion of the Allerød interstadial and persisted throughout Younger Dryas stadial c. 13,200-11,500 cal. years.

A large peak in the IRD flux (311-669 cm^2 ky^{-1}) occurs at the end of the Allerød interstadial (c. 13,200-13,150 cal. years) (Fig. 21), suggests that ice-rafting during this time was increased. This transition is interpreted to be driven by a further retreat of sub-ice stream II driven by persistent Atlantic Water inflow, with enhanced ice-rafting during the latter portion of the Allerød interstadial. Stronger currents must have persisted during the late Allerød interstadial, indicated by the peak in the relative abundance of *C. lobatulus* (12-18 %) (c. 13,300-13,100 cal. years and single peak of *A. gallowayi* (3-10 %) at c. 13,300-13,200 cal. years in AZ2 (Fig. 22). The strong bottom currents were probably driven through the mixing of Atlantic Water with the turbulent meltwater, which would have caused winnowing of the finer grain sizes and may have contributed to the reduced sedimentation rates during this time (Table. 6).

The IRD flux decreases sharply (119 cm^2 ky^{-1}) at the start of the Younger Dryas stadial (c. 12,700 cal. years) (Fig. 21). The influence of Atlantic Water may have been reduced at c. 12,700 cal. years perhaps due to weakened AMOC due to the meltwater release from the proglacial Lake Agassiz (e.g., Kennett and Shackleton, 1975; Broecker et al., 1989, Clark et al., 2001). The meltwater is thought to have drained directly into the Arctic via the Mackenzie Delta, leading to a rapid freshening of the surface and enhanced sea-ice formation (Murton et al., 2010; Müller and Stein, 2014).

The strength of the bottom currents also appears to have been affected in the start of the Younger Dryas, observed as a decrease in the relative abundance of C. *lobatulus* at 138 cm (8 %) (Fig. 22). Weakening of the bottom currents may have been driven by reduced mixing processes due to the reduced Atlantic Water inflow at this time. Although Atlantic Water may have been reduced at the start of the Younger Dryas a small peak in *C. neoteretis* (3-7 %) at c. 13,150-12,200 cal. years (Fig. 22), suggests Atlantic Water must still be present, but to a lesser degree in the Storfjorden Trough.

The gradual decreasing trend in relative abundance of *E. excavatum* (47 to 4 %) during the Allerød interstadial is interrupted by a slight peak in relative abundance (23 %) at the start of the Younger Dryas (Fig. 22). The increase in *E. excavatum*, combined with the rapid decrease in the flux of IRD (Fig. 22-23) indicate that c. 12,700 cal. years was characterised by more polar conditions compared to the Allerød interstadial, which has also been documented on the outer Storfjorden Trough (Rasmussen et al., 2007).

The formation of perennial sea-ice cover could have possibly prevented icebergs from being transported from the ice front, which has also been proposed at this time in the central Storfjorden Trough and the northern and eastern Barents Sea (Ślubowska-Woldengen et al., 2008; Klitgaard-Kristensen et al., 2013; Łącka et al., 2015). The presence of perennial sea-ice cover is supported by the sharp decrease in accumulation rate of benthic foraminifera from 1841 to 179 cm^2 ky^{-1} (Fig. 23), which is linked to productivity. A thick sea-ice cover would prevent the sunlight from penetrating the surface waters and lead to reduced productivity (Müller and Stein, 2014). A reduction in palaeoproductivity due to persistent sea-ice cover during the early stages of the Younger Dryas has been documented in the northern Barents Sea and eastern Fram Strait (Wollenburg et al., 2004; Müller and Stein, 2014).

The relative abundance of *E. excavatum* decreases towards the end of the Younger Dryas from 23 % to 4 % (Fig. 22). This, combined with peaks in the relative abundance of *C. neoteretis* (7 %), *C. lobatulus* (14-18 %) and *A. gallowayi* (4 %) between c. 12,200-11,500 cal. years (Fig. 22), indicates the rejuvenation of Atlantic Water and stronger bottom water currents. The IRD flux also increases slightly (176-212 cm^2 ky^{-1}) coinciding with a prominent gravel lens at c. 11,900-11,500 cal. years between 132-128 cm (Fig. 20; 21). This suggests that ice-rafting to the core site HH13-26 increased drastically, supplied from the release of icebergs that were trapped by the perennial sea-ice during the early stages of the Younger Dryas.

The impact of colder conditions and reduced Atlantic Water inflow during the Younger Dryas appears to have been an abrupt, short-lived event. The temporal resolution of our data did not capture the interval between c. 12,700-12,200 cal. years and we were unable to come to any conclusions on how long these cold, polar conditions prevailed. However, we propose that the conditions had improved by the end of the Younger Dryas c. 12,200-11,500 cal. years.

The δ^{18}O values are at their lowest (2.81-3.97 ‰) during the Allerød-Younger Dryas periods and relate to estimated pore water palaeotemperatures between 3.06-5.90 ºC from the *C. reniforme* record and bottom water palaeotemperatures between 2.75-6.19 ºC from the *C. lobatulus* record (Fig. 24). A temperature rise of this magnitude is inconsistent with high volumes of cold, turbid meltwater. The markedly low δ^{18}O values (Fig. 24) are perhaps due to the large input of isotopically light δ^{18}O fresh, cold meltwater from the retreating sub-ice stream II. However, bottom water salinities in the Barents Sea are considered to be relatively stable and high due to Atlantic inflow (Lubinski et al., 2001; Klitgaard-Kristensen et al., 2013). Therefore, it is unlikely that the bottom water salinity reduced enough to be the controlling mechanism to produce the low δ^{18}O values. The meltwater is interpreted to have risen to the surface as it was less dense than the saline Atlantic Water, forming a fresh water lid. Strong stratification of the water masses at the surface may have permitted the bottom water temperature to rise considerably, especially when mixed with the subsurface warm Atlantic Water. The estimated palaeotemperatures (Fig. 24) are highly seasonal and reflect the bottom water temperature during the summer as all three species (*C. lobatulus*, *C. reniforme* and *I. norcrossi*) are proposed to calcify during the summer months (Zajączkowski et al., 2010; Skirbekk et al., 2014)

The low peak in δ^{13}C record (-0.28 to 0.78 ‰) from *C. lobatulus* observed at c. 13,200-12,700 cal. years between 146-138 cm (Fig. 24). The low peak is probably produced through a high volume of fresh, meltwater input containing low δ^{13}C DIC that reduced the overall δ^{13}C DIC of the sea water. Low δ^{13}C DIC could also suggest a poor ventilation conditions, but this is highly unlikely as the mixing of meltwater with Atlantic Water would form a well-ventilated water mass. Similar low $\delta^{13}C$ values have been recorded in planktonic and benthic foraminifera in response to meltwater input during deglaciation in the northern Barents and Kara Seas (Lubinski et al., 2001).

The low $\delta^{13}C$ value (0.72 ‰) recorded at the start of the Younger Dryas (c. 12,700 cal. years) at 138 cm (Fig. 24) may have indicated poor ventilation and/or increased supply of low $\delta^{13}C$ DIC, due to the reduced Atlantic Water inflow proposed for this time and the presence of meltwater. However, due to the high relative abundance of *E. excavatum* (23 %) (Fig. 22) suggesting low salinity, cold bottom water it is interpreted to be derived from remnants of low salinity meltwater and/or the dominance of polar water during this period.

6.3 Early Holocene (c. 11,500-8200 cal. years)

The early Holocene is documented to have been a period of enhanced summer insolation with stronger Atlantic Water inflow into the Arctic, reduced sea-ice and the northward movement of the Arctic Front (Berger and Loutre, 1991; Koç et al., 1993; Kaufman et al., 2004; Jessen et al., 2010).

The sedimentology in the upper part of lithological unit L2(a) consists of fine-silty clay with low magnetic susceptibility and decreased IRD concentration (Fig. 20). The high content of very fine sediments (<63 µm) (83-94 %) is interpreted to be caused by a reduction in the strength of the bottom currents (Fig. 20). The low IRD concentration (<23 g^{-1}) suggests that ice rafting during this time was significantly reduced (Fig. 20). The reduction in the strength of the bottom currents is also observed from the low relative abundance of *C. lobatulus* (<2%) and *A. gallowayi* (<1 %) in AZ3 and AZ4 (Fig. 22), possibly due to the reduction of input of turbid meltwaters as sub-ice stream II was at a more distal position.

The sedimentation rate remains low during this period 7.6 cm ky^{-1} (Table 8), and combined with the low accumulation rate of benthic foraminifera (<425 cm^2 ky^{-1}) (Fig. 23) it indicates that productivity was low. A gradual increase is observed in the species diversity although it does fluctuate (11-17 species) from c. 10,000-8400 cal. years (Fig. 23).

The foraminiferal assemblage in AZ3 and AZ4 is dominated by 'ice-proximal' faunas *C. reniforme* (relative abundance 36-54 %) and *E. excavatum* (relative abundance 15-38 %) (Fig. 22). The dominance of *C. reniforme* over *E. excavatum* suggests that conditions were slightly improved (Hald and Korsun, 1997) and the influence of sub-ice stream II was reduced as it had likely retreated further east by this time. The relative abundance of *N. labradorica* fluctuates significantly throughout this period (1-26 %), peaking at two intervals c. 11,100-10,600 cal. years and c. 9000 cal. years (Fig. 22). However, it was noted that the samples from the earliest period contained <200 specimens therefore will contribute to the observed peak during this time. The appearance of *S. loeblichi* (<5 %)*, I. norcrossi* (<3 %) and *Buccella* spp. (<2 %) (Fig. 22) are indicative of less extensive, and more seasonal sea-ice cover (Steinsund, 1994; Polyak et al., 2002).

The $\delta^{18}O$ values from *C. reniforme* are low (3.63-4.05 ‰) before c. 9500 cal. years and change to higher values (>4.16 ‰) by c. 9000 cal. years (Fig. 24), which is interpreted to represent a shift from the dominance of isotopically lighter Arctic water to Atlantic Water (Duplessey et al., 2005; Ślubowska et al., 2005). Increased summer insolation in the northern hemisphere during the early Holocene (Berger and Loutre, 1991) likely caused sub-ice stream II to retreat further to the east and permitted the inflow of the ESC. The influence of Arctic water during the start of the early Holocene may have been driven by the inflow of the ESC into the Storfjorden Trough after sub-ice stream II retreated. The minor occurrence of *C. neoteretis* (<5%) and *E. subarcticum* (<2 %) indicates that Atlantic water inflow was present throughout this period (Sejrup et al., 1987; Mackensen and Hald, 1988; Polyak and Mikhailov, 1996) (Fig. 22). However, during the start of the early Holocene the Atlantic Water signal was inhibited in the $\delta^{18}O$ record due to the inflow of the ESC. The extremely low benthic foraminifera concentration (6 g^{-1}) at the start of the early Holocene coincides with a peak in the percentage of fragmentation of the tests (67 %) (Fig. 23), suggesting the cold Arctic waters were very corrosive.

The estimated pore water palaeotemperatures from *C. reniforme* displays an increasing trend from 0.30-2.26 ºC between c. 11,100-9500 cal. years and a decreasing trend from 0.78 to -1.50 ºC between c. 9000-8400 cal. years (Fig. 24). There was only one data point available at c. 9000 cal. years for the preferred species *C. lobatulus* (Fig. 24), which records bottom water temperatures. The estimated bottom water palaeotemperature for that time was 3.46 ºC (Fig. 24), supporting the dominance of Atlantic Water at this time. The high relative abundance of *N. labradorica* (26 %) and the occurrence of *M. barleeanus* (4 %) at c. 9000 cal. years (Fig. 22) strongly suggests that the Arctic Front was close-by (Hald and Steinsund, 1992). The shift in dominance of water masses from Arctic water to Atlantic Water during the early Holocene has been documented in the central (JM09-020-GC) and outer parts of the Storfjorden Trough (JM02-460GC/PC) (Rasmussen et al., 2007; 2015; Łącka et al., 2015) (Fig. 19), as well as in several records from the western and northern Svalbard shelf (Ślubowska-Woldengen et al., 2007; Skirbekk et al., 2010; Kubischta et al., 2011; Chauhan et al., 2014).

The $\delta^{13}C$ values from *C. reniforme* are difficult to interpret as this species records changes in the pore water conditions, which are usually quite stable. The one data point obtained from *C. lobatulus* (0.95 ‰) at c. 9000 cal. years is relatively low (Fig. 24), but higher than the meltwater inputs from the Allerød interstadial indicating that the meltwater inputs were supressed at this time.

The estimated low palaeotemperature (-1.50 ºC) from *C. reniforme* at c. 8400 cal. years coincides with the timing of the 8.2 Ky event (Fig. 24). The 8.2 Ky event is recorded as an abrupt climatic event where AMOC was reported to be inhibited, due to a huge freshwater input from the drainage of proglacial lakes Agassiz and Ojibway into the Hudson Bay (Klitgaard-Kristensen et al., 1998; Clark et al., 2001; Carlson et al., 2009). This short-lived event appears to have been recorded at the core site HH13-26 as a reduced pore water temperature (-1.50 ºC) and an increase in the relative abundance of *E. excavatum* (38 %) (Fig. 22; 24), interpreted as the prevalence of cold, fresh Arctic water over the suppressed Atlantic Water inflow during this time.

The early Holocene appears to be under the influence of improved yet fluctuating conditions in a relatively short period of time c. 11,500-8200 cal. years.

6.4 Mid-Holocene (c. 8200-4000 cal. years)

The mid-Holocene has been documented to be a prolonged period of strong Atlantic Water inflow into the Arctic with very little glacial activity reported on Svalbard (Elverhøi et al., 1995; Svendsen and Mangerud, 1997; Ślubowska-Woldengen et al., 2008).

The sediments within lithological unit L2(b) consist of fine-grained mud of clayey silt with bivalve shells and fragments (Fig. 20). A period of deposition of coarser very fine-sandy silt occurs between c. 6000-4750 cal. years. The sediments are of low magnetic susceptibility (<20.8 SI 10^{-6}) and shear strength (<27 kPa), with the presence of few clasts (Fig. 20) indicating ice-rafting of larger material was significantly reduced throughout the mid-Holocene.

The estimated sedimentation rates between c. 8200-7100 cal. years remain low 7.6 cm ky^{-1} and increase to 12.8 cm ky^{-1} after c. 7100 cal. years (Table 8). The sediments in this interval were noted as being very organic-rich when sieving and the increase in sedimentation rate likely corresponds to high productivity during this time. The accumulation rate of both planktonic (276 cm^2 ky^{-1}) and benthic foraminifera (8126 cm^2 ky^{-1}) increase to a maximum at

c. 5700 cal. years and decreases thereafter, but still remains high (67; 534 cm^2 ky^{-1}) (Fig. 23; 25). The concentration of larger specimens of benthic foraminifera (0.5-1 mm) increases in the mid-Holocene, peaking at c. 7000 cal. years (9 g^{-1}) (Fig. 23). The high accumulation rate of foraminifera during this period is also documented in the central Storfjorden Trough (JM09-020-GC) (Łącka et al., 2015) (Fig. 19).

The percentage of fragmentation is relatively low (22-47 %) (Fig. 23), indicating that bottom waters were not sufficiently cold enough for corrosion or the lack of strong bottom currents that may lead to fragmentation.

The foraminiferal assemblage in both AZ5 and AZ6 has a high species diversity peaking at c. 6600 cal. years (22 species), then decreases slightly between c. 6300-5000 cal. years (20 to14 species), before increasing again between c. 4750-4000 cal. years (19 species) (Fig. 23). The relative abundance of *C. reniforme* (>44 %) dominates the assemblage throughout the mid-Holocene, with the relative abundance of *E. excavatum* reduced even further (<12 %) compared to the preceding interval (Fig. 22). The high relative abundance of *C. reniforme* and presence of *M. barleeanus* (<5 %), *Buccella* spp. (<3 %), *C. neoteretis* (1-13 %) and *E. subarcticum* (2-11 %) indicate the constant inflow and dominance of Atlantic Water during this period (Sejrup et al., 1987; Mackensen and Hald, 1988; Steinsund, 1994; Polyak and Mikhailov, 1996; Hald and Korsun, 1997; Korsun and Hald, 1998) (Fig. 22).

The planktonic assemblage at the start of the mid-Holocene is dominated by the polar species *N. pachyderma* (s) (55 %) (Fig. 25) and sub-polar species *T. quinqueloba* (16 %), *N. pachyderma* (d) (12 %), and *Globigerina/Globigerinita* spp. (1 %) (Bé and Tolderlund, 1971). The peak in planktonic foraminifera in particular *T. quinqueloba* (16 %), correspond to peaks in benthic species *N. labradorica* (6-10 %) and occurrence of *M. barleeanus* (3-5 %) (Fig. 25). The relative abundance of these species combined with the high accumulation rate and sedimentation rate is interpreted to be indicative of high productivity due to the presence of the Arctic Front nearby, separating Atlantic Water and Arctic water (Bé and Tolderlund, 1971; Cedhagen, 1991; Polyak et al., 2002)

A single peak in the relative abundance of *A. gallowayi* (4 %) at c. 6600 cal. years and *C. lobatulus* (8 %) is observed at c. 6300 cal. years (Fig. 22), perhaps indicating slightly elevated bottom currents and a high food supply (Sejrup et al., 1981; Wollenburg and Mackensen, 1998; Polyak et al., 2002). The increased relative abundance of *I. norcrossi* (5-10 %) and *Buccella* spp. (2-3 %) and occurrence of *S. loeblichi* (1 %) from c. 6000 cal. years corresponds to the slight increase in sand content at this time (Fig. 20-22), which suggest that seasonal sea-ice was present and ice-rafting to the core site occurred (Polyak et al., 2002). This ice-rafting indicates a shift to more polar conditions, with the very fine-sand possibly supplied from the export of land fast ice that formed along the sandy coastline of Barentsøya and Edgeøya as observed today (Etzelmüller et al., 2003).

The $\delta^{18}O$ record from *C. lobatulus* displays high and relatively stable values (3.94-4.33 ‰) with the estimated bottom water palaeotemperatures between 0.10-1.67 ºC (Fig. 24), indicating the prevalence of Atlantic Water throughout the mid-Holocene. The maximum palaeotemperature (1.67 ºC) (Fig. 24) corresponds to c. 4750 cal. years and a peak in the relative abundance of *C. neoteretis* (13 %) (Fig. 22), suggesting the Atlantic Water inflow was less modified by Arctic water and surface water may have been stratified. The palaeotemperatures exhibit a gradual decreasing trend thereafter (1.67 to 0.67 ºC) and relate to an increase in *N. labradorica* (9 %) which thrive in marginal-ice zones (Fig. 22; 24), indicating the southward movement of the location of the Arctic Front (Polyak et al., 2002).

The shifts in relative abundance of *C. neoteretis* (2-13 %) and *E. subarcticum* (2-11%) suggest less modified Atlantic Water and show a slight inverse relationship to the relative abundance of *N. labradorica* (2-17 %) and *M. barleeanus* (0-5 %) (Fig. 22), that are indicative of oceanic fronts and higher food supply (Carlap, 1989, Polyak et al., 2002). Although the presence of Atlantic Water is believed to have occurred throughout the mid-Holocene, the shifts in foraminiferal species relative abundances (Fig. 22) may be indicative of the shifting position of the Arctic Front.

The $\delta^{13}C$ values from *C. lobatulus* are relatively high and stable (1.27-1.63 ‰) indicating well-ventilated water masses during the mid-Holocene (Fig. 24). There is one low peak (0.61 ‰) in the $\delta^{13}C$ record observed at c. 4750 cal. years that corresponds to the peak in estimated palaeotemperature (1.67 ºC) and the end of the high input of sand content (Fig. 24). The low $\delta^{13}C$ value at this time may have been derived from the inflow of fresh, cold Arctic water or poor ventilation, however it is unlikely considering the high $\delta^{18}O$ value (3.94 ‰) (Fig. 24) and presence of Atlantic Water at this time. It is therefore considered to either be an erroneous value or it could be linked to enrichment in ^{12}C supplied from the organic input from high surface water productivity.

The prevalence of Atlantic Water throughout the mid-Holocene and shift to colder conditions towards the Late Holocene from increased ice-rafting has also been documented in the central (JM09-020-GC) and outer Storfjorden Trough (JM02-460GC/PC) (Rasmussen et al., 2007; Łącka et al., 2015) (Fig. 19), and in several records along western Svalbard and the northern Svalbard shelf (e.g., Ślubowska et al., 2005; Ślubowska-Woldengen et al., 2007; 2008; Skirbekk et al., 2010; Kubischta et al., 2011; Klitgaard-Kristensen et al., 2013; Rasmussen et al., 2013).

6.5 Late Holocene-recent (the last 4000 cal. years)

The Late Holocene climate has been documented to have shifted between short-term warm and cold phases, with evidence of glacial advance on Svalbard (Svendsen and Mangerud, 1997).

The sediments in the upper portion of lithological unit L2(b) consist of fine-grained mud of clayey silt and silty clay at the top with low magnetic susceptibility and shear strength (Fig. 20). The sedimentation rate is 12.8 cm ky^{-1} until c. 3400 cal. years then increases to 14.3 cm ky^{-1} (Table 8).

The accumulation rate of the benthic foraminifera shows a decreasing trend in this period (6088 to 367 cm^2 ky^{-1}), but species diversity remains high (14-23 species) (Fig. 23). The benthic foraminifera assemblage AZ6 and AZ7 is still dominated by *C. reniforme* (>29 %) and *E. excavatum* (>10 %) (Fig. 22). The relative abundance of *N. labradorica* is high in AZ6 (7-13 %), with the occurrence of *E. subarcticum* (3-10 %), *C. neoteretis* (5-12 %), *M. barleeanus* (1-4 %) and *Buccella* spp. (1-4 %) between c. 4000-1800 cal. years (Fig. 22). This is indicative of strong Atlantic Water inflow and a proximal location of the Arctic Front during this time, with a high food supply (Sejrup et al., 1987; Mackensen and Hald, 1988; Cedhagen, 1991; Hald and Korsun, 1997; Polyak et al., 2002). There is a small peak in the relative abundance of *C. lobatulus* (2-4 %) and the percentage of fragmentation (44-49 %) at c. 3500-2600 cal. years (Fig. 22-23), which may be caused from enhanced bottom currents at this time (Sejrup et al., 1981; Hald and Korsun, 1997). The accumulation rate of planktonic species (10-115 cm^2 ky^{-1}) is low throughout the Late Holocene (Fig. 28), with one sample at c. 3400 cal. years predominantly consisting of polar species *N. pachyderma* (s) (82 %) (Fig. 25) with little contribution of sub-polar species *T. quinqueloba* (17 %), suggesting the Arctic Front was close and sea surface temperatures were low (Bé and Tolderlund, 1971).

The relative abundance of the opportunistic species *E. excavatum* is increased (12-23 %) at c. 2700-1000 cal. years (Fig. 22). The benthic foraminiferal assemblage in AZ7 from c. 1800 cal. years shifts to increased relative abundances of species that are indicative of increased sea-ice. The relative abundance of *I. norcrossi* remains high (7-16 %) from c. 1800 cal. years, combined with the presence of *S. loeblichi* (<3 %) and *A. gallowayi* (<3 %) (Fig. 22). This is interpreted to represent the southward movement of the Arctic Front with colder conditions and more extensive sea ice cover. Although the IRD flux of larger clasts was low throughout the late Holocene, there is a peak in the fine-sand fraction from c. 1800 cal. years (Fig. 21), which could be indicative of ice-rafting from land fast ice. The accumulation rate of benthic foraminifera in AZ7 is low (<2847 cm^2 ky^{-1}) from c. 1800 cal. years (Fig. 23), suggesting that productivity was reduced during this period. The percentage of agglutinated species also increases (3-14 %) (Fig. 23), with peaks in the relative abundance of *A. glomerata* (2-9 %) between c. 1800-1000 cal. years (Fig. 22), suggesting colder climatic conditions as observed in inner Storfjorden (Rasmussen and Thomsen, 2015). An increase in sea ice cover and reduced productivity during the Late Holocene has also been documented on the Yermak Plateau and northern Svalbard slope by Wollenburg et al. (2004).

The proposed colder conditions and increased sea ice cover could relate to the short-term colder periods that have been documented throughout Europe, the Dark Ages Cold Period c. 1500-1100 cal. years and the Little Ice Age c. 600-100 cal. years (Grauel et al., 2013).

The δ^{13}C values obtained from *C. lobatulus* are high and stable (1.13-1.36 ‰) until c. 1500 cal. years and increase further (>1.40 ‰) thereafter (Fig. 24). The high δ^{13}C values indicate well-ventilated bottom water and the increase at c. 1500 cal. years may be contributed to the inflow of cold, Arctic waters transported by the ESC. The δ^{18}O values remain high (>3.74 ‰) with the estimated bottom water palaeotemperatures (0.15-2.46 ºC) (Fig. 24), indicating the presence of relatively warm, saline Atlantic Water throughout the Late Holocene. The δ^{18}O values are slightly lower than the mid-Holocene (Fig. 24), suggesting Atlantic Water inflow was decreased. A single peak in $\delta^{18}O$ (4.85 ‰) is observed at c. 2700 cal. years, corresponding to a low estimated bottom water palaeotemperature of -1.98 ºC (Fig. 24) and slight increase in the relative abundance of *E. excavatum* (14 %) (Fig. 22), which may be related to an influx of colder, fresher Arctic water at this time.

The general cooling trend with slightly increased bottom-currents during the Late Holocene has been documented in the central Storfjorden Trough (JM09-020-GC) (Łącka et al., 2015) (Fig. 19). Although Łącka et al. (2015) did not propose a driving mechanism for the increased bottom-currents, we propose they may have occurred from brine overflow from the inner Storfjorden basin as the sea ice production and subsequent brine formation was high in the late Holocene (Rasmussen and Thomsen, 2015). The colder conditions and reduced Atlantic inflow has been documented in the inner Storfjorden Basin, the central Storfjorden Trough (Fig. 19) and in several records along the western and northern Svalbard shelf (Ślubowska-Woldengen et al., 2007; Rasmussen and Thomsen, 2015; Łącka et al., 2015)

The suggested cooling trend during the Late Holocene is supported with evidence of glacial advance at least on the west of Spitsbergen (Svendsen and Mangerud, 1997), and corresponds to the disappearance of *Mytilus edulis* around Svalbard during this time (Berge et al., 2006).

The elongate grooves that occur on the multibeam image surface of the glacial lobe (Fig. 8) are interpreted to be ice-berg scours due to their random orientation and the relatively shallow water depth in which they occur. The ice-berg scours could have been formed at any time during the Holocene, illustrating the Storfjorden Trough was still under the influence of ice-rafting by ice-bergs during the Holocene.

7. Conclusions

The first model for the reconstruction of the retreat of sub-ice stream II and the proceeding palaeoceanographical conditions for the eastern Storfjorden Trough has been presented. The main outcomes of this study are described as follows:

- Sub-ice stream II had retreated rapidly from the core site in the eastern Storfjorden Trough and still-stand of the grounding line occurred proximal to core HH13-26 supplying vast quantities of glacial debris, leading to the build-up of the glacial lobe prior to c. 14,000 cal. years.
- The nature of the still-stand could have followed the initial rapid retreat at the core site or have been related to a re-advance of sub-ice stream II. The still-stand was proposed to have been controlled by changes in bathymetry in the eastern Storfjorden Trough and/or isostatic uplift and subsequent lowered sea level.
- This new model of retreat of sub-ice stream II in the eastern Storfjorden Trough may aid in the reconstruction and give further insight into the dynamics of the deglaciation of the SBIS.
- The onset of glaciomarine sedimentation occurred by c. 13,800 cal. years during the Allerød interstadial and was characterised by the rapid deposition of fine-grained sediments from meltwater plumes during the retreat of sub-ice stream II from the grounding line.
- The initial inflow of Atlantic Water into the eastern Storfjorden Trough is proposed to have driven the further retreat of sub-ice stream II, with persistent ice-rafting and subsequent mixing with the turbid meltwater to form strong-bottom currents towards the end of the Allerød interstadial c. 13,300-13,100 cal. years.

- The end of the Allerød interstadial and the start of the Younger Dryas stadial c. 13,100-12,700 cal. years was characterised by a reduced flow of Atlantic Water, with weakened bottom-currents. Polar conditions persisted at the start of the Younger Dryas with extensive perennial sea-ice cover.

- The rejuvenation of stronger Atlantic Water inflow occurred towards the end of the Younger Dryas, with enhanced bottom-currents and increased ice-rafting from the break-up of the perennial sea ice c. 12,200-11,500 cal. years.

- The early Holocene c. 11,500-8200 cal. years was influenced by fluctuating but improved oceanographic conditions, with seasonal sea-ice cover, reduced bottom-currents and ice-rafting. The dominance of Atlantic Water over Arctic water occurred at c. 9000 cal. years. A short-lived cold event is documented at c. 8400 cal. years with a suppression of Atlantic water inflow corresponding to the 8.2 Ky event.

- The mid-Holocene was characterised by the prevalence of Atlantic Water inflow into the eastern Storfjorden Trough, with high productivity and the shifting position of the Arctic Front. Towards the Late Holocene c. 6000 cal. years there was a shift to more polar conditions with increased ice-rafting.

- A general cooling trend is observed in the late Holocene with reduced Atlantic Water inflow, extensive sea ice cover and increased bottom-currents from c. 1800 cal. years.

References

Aagaard, K., Swift, J. H., and Carmack, E. C. (1985). Thermohaline circulation in the Arctic Mediterranean seas. *J. Geophys. Res*, *90*(C3), 4833-4846.

Akimova, A., Schauer, U., Danilov, S., and Núñez-Riboni, I. (2011). The role of the deep mixing in the Storfjorden shelf water plume. *Deep Sea Research Part I: Oceanographic Research Papers, 58*(4), 403-414.

Andersen, E. S., Dokken, T. M., Elverhøi, A., Solheim, A., and Fossen, I. (1996). Late Quaternary sedimentation and glacial history of the western Svalbard continental margin. *Marine Geology*, *133*(3), 123-156.

Armstrong, H. A., and Brasier, M. D. (2005). Foraminifera. *Microfossils.* Second Edition, 142-187.

Arnold, J. R., and Libby, W. F. (1949). Age determinations by radiocarbon content: checks with samples of known age. *Science*. *110*(2869), 678-680.

Austin, W. E. N., and Kroon, D. (1996). Late glacial sedimentology, foraminifera and stable isotope stratigraphy of the Hebridean Continental Shelf, northwest Scotland. *Geological Society, London, Special Publications*, *111*(1), 187-213.

Bartington User Manual, Issue 48.

Bé, A.W.H., and Tolderlund, D. S. (1971). Distribution and ecology of living planktonic foraminifera in surface waters of the Atlantic and Indian Oceans. *The micropaleontology of oceans*, 105-149.

Berge, J., Johnsen, G., Nilsen, F., Gulliksen, B., Slagstad, D., and Pampanin, D. M. (2006). The Mytilus edulis population in Svalbard: how and why. *Marine-Ecology Progress Series*, *309*, 305.

Boltovskoy, E., Boltovskoy, D., Correa, N., and Brandini, F. (1996). Planktic foraminifera from the southwestern Atlantic (30–60 S): species-specific patterns in the upper 50 m. *Marine micropaleontology*, *28*(1), 53-72.

Bondevik, S., 1993. Postglasial strandforskyvning på Svalbard. Unpublished Cand. scient. thesis, University of Bergen, 81 pp.

Bondevik, S., Mangerud, J., Birks, H. H., Gulliksen, S., and Reimer, P. (2006). Changes in North Atlantic radiocarbon reservoir ages during the Allerød and Younger Dryas. *Science*, *312*(5779), 1514-1517.

Broecker, W. S. (1982). Ocean chemistry during glacial time. *Geochimica et Cosmochimica Acta*. *46*(10), 1689-1705.

Broecker, W. S., Kennett, J. P., Flower, B. P., Teller, J. T., Trumbore, S., Bonani, G., and Wolfli, W. (1989). Routing of meltwater from the Laurentide Ice Sheet during the Younger Dryas cold episode. *Nature*, *341*, 318-321.

Broecker, W. S. (1991). The great ocean conveyor. *Oceanography*, *4*(2), 79-89.

Broecker, W. S. (2006), a. Abrupt climate change revisited. *Global and Planetary Change*, *54*(3), 211-215.

Broecker, W. S. (2006), b. Was the Younger Dryas triggered by a flood? *Science*, *312*(5777), 1146-1147.

Carlap, M.H., 1989. Abundance of *Bulimina exilis* and *Melonis barleeanum*: Relationship to the quality of marine organic matter. *Geo-Marine Letters*, *9*, 37-43.

Carstens, J., Hebbeln, D., and Wefer, G. (1997). Distribution of planktic foraminifera at the ice margin in the Arctic (Fram Strait). *Marine Micropaleontology*, *29*(3), 257-269.

Cedhagen, T. (1991). Retention of chloroplasts and bathymetric distribution in the sublittoral foraminiferan Nonionellina labradorica. *Ophelia*, *33*(1), 17-30.

Corliss, B. H. (1985). Microhabitats of benthic foraminifera within deep-sea sediments. *Nature*, *314*, 435-438.

Corliss, B. H. (1991). Morphology and microhabitat preferences of benthic foraminifera from the northwest Atlantic Ocean. *Marine Micropaleontology*, *17*(3), 195-236.

Curry, J. A., Schramm, J. L., and Ebert, E. E. (1995). Sea ice-albedo climate feedback mechanism. *Journal of Climate*, *8*(2), 240-247.

Dansgaard, W., Johnsen, S. J., Clausen, H. B., Dahl-Jensen, D., Gundestrup, N., Hammer, C. U., and Oeschger, H. (1984). North Atlantic climatic oscillations revealed by deep Greenland ice cores. *Climate processes and climate sensitivity*, 288-298.

Dayton, P. K., Mordida, B. J., and Bacon, F. (1994). Polar marine communities. *American Zoologist*, *34*(1), 90-99.

De Jong, J. (1988). Climatic variability during the past three million years, as indicated by vegetational evolution in northwest Europe and with emphasis on data from The Netherlands. *Philosophical Transactions of the Royal Society of London B: Biological Sciences*, *318*(1191), 603-617.

Donn, W. L., and Ewing, M. (1966). A theory of ice ages III. *Science*, 152 (3730), 1706-1712

Dowdeswell, J. A., Kenyon, N. H., Elverhøi, A., Laberg, J. S., Hollender, F. J., Mienert, J., and Siegert, M. J. (1996). Large-scale sedimentation on the glacier-influenced polar North Atlantic Margins: Long-range side-scan sonar evidence. *Geophysical Research Letters*, *23*(24), 3535-3538.

Dunton, K. (1992). Arctic biogeography: the paradox of the marine benthic fauna and flora. *Trends in Ecology & Evolution*, *7*(6), 183-189.

Duplessy, J. C., Lalou, C., and Vinot, A. C. (1970). Differential isotopic fractionation in benthic foraminifera and paleotemperatures reassessed. *Science*, *168*(3928), 250-251.

Duplessy, J. C., Cortijo, E., Ivanova, E., Khusid, T., Labeyrie, L., Levitan, M., Murdmaa, I., and Paterne, M. (2005). Paleoceanography of the Barents Sea during the Holocene. *Paleoceanography*, *20*(4).

Elverhøi, A., and Bomstad, K. (1980). Late Weichselian glacial and glaciomarine sedimentation in the western, central Barents Sea.

Elverhøi, A., Fjeldskaar, W., Solheim, A., Nyland-Berg, M., and Russwurm, L. (1993). The Barents Sea Ice Sheet—a model of its growth and decay during the last ice maximum. *Quaternary Science Reviews*, *12*(10), 863-873.

Elverhøi, A., Andersen, E. S., Dokken, T., Hebbeln, D., Spielhagen, R., Svendsen, J. I., Sørflaten, M., Rørres, A., Hald, M., and Forsberg, C. F. (1995). The growth and decay of the Late Weichselian ice sheet in western Svalbard and adjacent areas based on provenance studies of marine sediments. *Quaternary Research*, *44*(3), 303-316.

Elverhøi, A., Hooke, R. L., and Solheim, A. (1998). Late Cenozoic erosion and sediment yield from the Svalbard–Barents Sea region: implications for understanding erosion of glacierized basins. *Quaternary Science Reviews*, *17*(1), 209-241.

Emiliani, C. (1955). Pleistocene Temperatures. *The Journal of Geology*. 63 (6), 538-578.

Eyles, N., Eyles, C. H., and Miall, A. D. (1983). Lithofacies types and vertical profile models; an alternative approach to the description and environmental interpretation of glacial diamict and diamictite sequences. *Sedimentology*, *30*(3), 393-410.

Fairbanks, R. G. (1989). A 17, 000-year glacio-eustatic sea level record: influence of glacial melting rates on the Younger Dryas event and deep-ocean circulation. *Nature*, *342*(6250), 637-642.

Faure, G., and Mensing, T.M. (2005). *Isotopes Principles and Applications*. 3rd ed. New Jersey: John Wiley & Sons Ltd. 691-767.

Forman, S. L., Lubinski, D., Miller, G. H., Snyder, J., Matishov, G., Korsun, S., & Myslivets, V. (1995). Postglacial emergence and distribution of late Weichselian ice-sheet loads in the northern Barents and Kara seas, Russia. *Geology*, *23*(2), 113-116.

Forwick, M., and Vorren, T. O. (2012). Submarine mass wasting in Isfjorden, Spitsbergen. In *Submarine mass movements and their consequences* (pp. 711-722). Springer Netherlands.

GeoTek website: *http://www.geotek.co.uk/products/magsusc*

Grossman, E. L. (1987). Stable isotopes in modern benthic foraminifera; a study of vital effect. *The Journal of Foraminiferal Research*, *17*(1), 48-61.

Haarpaintner, J., Gascard, J. C., and Haugan, P. M. (2001). Ice production and brine formation in Storfjorden, Svalbard. *Journal of Geophysical Research*, *106*(14.00314), 013.

Hald, M., and Vorren, T. O. (1987). Foraminiferal stratigraphy and environment of Late Weichselian deposits on the continental shelf off Troms, Northern Norway. *Marine Micropaleontology*, *12*, 129-160.

Hald, M., and Steinsund, P. I. (1992). Distribution of surface sediment benthic foraminifera in the southwestern Barents Sea. *The Journal of Foraminiferal Research*, *22*(4), 347-362.

Hald, M., Steinsund, P. I., Dokken, T., Korsun, S., Polyak, L., and Aspeli, R. (1994). Recent and Late Quaternary distribution of Elphidium excavatum f. clavatum in Arctic seas. *Cushman Foundation Special Publication*, *32*, 141-153.

Hald, M., and Steinsund, P. I. (1996). Benthic foraminifera and carbonate dissolution in the surface sediments of the Barents and Kara Seas. *Surface-sediment composition and sedimentary processes in the central Arctic Ocean and along the Eurasian Continental Margin. Berichte zur Polarforschung*, *212*, 285-307.

Hald, M., and Korsun. (1997). Distribution of modern benthic foraminifera from fjords of Svalhard, European Arctic. *Journal of Foraminiferal Research*, *27*, 101-122.

Hald, M., Kolstad, V., Polyak, L., Forman, S. L., Herlihy, F. A., Ivanov, G., and Nescheretov, A. (1999). Late-glacial and Holocene paleoceanography and sedimentary environments in the St. Anna Trough, Eurasian Arctic Ocean margin. *Palaeogeography, Palaeoclimatology, Palaeoecology*, *146*(1), 229-249.

Hald, M., Ebbesen, H., Forwick, M., Godtliebsen, F., Khomenko, L., Korsun, S., Ringstad Olsen, L., and Vorren, T. O. (2004). Holocene paleoceanography and glacial history of the West Spitsbergen area, Euro-Arctic margin. *Quaternary Science Reviews*, *23*(20), 2075-2088.

Hebbeln, D., Dokken, T., Andersen, E. S., Hald, M., and Elverhøi, A. (1994). Moisture supply for northern ice-sheet growth during the Last Glacial Maximum.

Hoefs. J. (2009), a. Isotope Fractionation Processes of Selected Elements. In: *Stable Isotope Geochemistry*. Berlin: Springer-Verlag. 48-53; 58-64.

Hoefs. J. (2009), b. Variations of Stable Isotope Ratios in Nature. In: *Stable Isotope Geochemistry*. Berlin: Springer-Verlag. 107; 150-152.

Holtedahl, H. (1959). Geology and paleontology of Norwegian Sea bottom cores. *Journal of Sedimentary Research*, *29*(1).

Hut, G. (1987). Consultants' group meeting on stable isotope reference samples for geochemical and hydrological investigations.

Ingólfsson, O. (2004). Outline of the geography and geology of Svalbard. *University of Iceland and UNIS*.

Ingólfsson, Ó., and Landvik, J. Y. (2013). The Svalbard–Barents Sea ice-sheet–Historical, current and future perspectives. *Quaternary Science Reviews*, *64*, 33-60.

Jakobsson, M., Andreassen, K., Bjarnadóttir, L. R., Dove, D., Dowdeswell, J. A., England, J. H., Funder, S., Hogen, K., Ingólfsson, Ó., Jennings, A., Larsen, N. K., Kirchner, N., Landvik, J. Y., Mayer, L., Mikkelsen, N., Möller, P., Niessen, F., Nilsson, J., O'Regan, M., Polyak, L., Nørgaard-Pedersen, N., and Stein, R. (2014). Arctic Ocean glacial history. *Quaternary Science Reviews*, *92*, 40-67.

Jansen, E., and Veum, T. (1990). Evidence for two-step deglaciation and its impact on North Atlantic deep-water circulation. *Nature*, *343*, 612-616.

Jessen, S. P., Rasmussen, T. L., Nielsen, T., and Solheim, A. (2010). A new Late Weichselian and Holocene marine chronology for the western Svalbard slope 30,000–0 cal years BP. *Quaternary Science Reviews*, *29*(9), 1301-1312.

Katz, M. E., Cramer, B. S., Franzese, A., Hönisch, B., Miller, K. G., Rosenthal, Y., and Wright, J. D. (2010). Traditional and emerging geochemical proxies in foraminifera. *The Journal of Foraminiferal Research*. *40*(2), 165-192.

Kaufman, D. S., Ager, T. A., Anderson, N. J., Anderson, P. M., Andrews, J. T., Bartlein, P. J., Brubaker, L. B., Coats, L. L., Cwynar, L. C., Duvall, M. L., Dyke, A. S., Edwards, M. E., Eisner, W. R., Gajewski, K., Geirsdóttir, A., Hu, F. S., Jennings, A. E., Kaplan, M. R., Kerwin, M. W., Lozhkin, A. V., MacDonald, G. M., Miller, G. H., Mock, C. J., Oswald, W. W., Otto-Bliesner, B. L., Porinchu, D. F., Rühland, K., Smol, J. P., Steig, E. J., and Wolfe, B. B. (2004). Holocene thermal maximum in the western Arctic (0–180 W). *Quaternary Science Reviews*, *23*(5), 529-560.

Kempf, P., Forwick, M., Laberg, J. S., and Vorren, T. O. (2013). Late Weichselian and Holocene sedimentary palaeoenvironment and glacial activity in the high-arctic van Keulenfjorden, Spitsbergen. *The Holocene*, 0959683613499055.

Kennett, J. P., and Shackleton, N. J. (1975). Laurentide ice sheet meltwater recorded in Gulf of Mexico deep-sea cores. *Science*, *188*(4184), 147-150.

Klenke, M., and Schenke, H. W. (2002). A new bathymetric model for the central Fram Strait. *Marine Geophysical Researches*, *23*(4), 367-378.

Klitgaard-Kristensen, D., Rasmussen, T. L., and Koç, N. (2013). Palaeoceanographic changes in the northern Barents Sea during the last 16 000 years–new constraints on the last deglaciation of the Svalbard–Barents Sea Ice Sheet. *Boreas*, *42*(3), 798-813.

Knies, J., Matthiessen, J., Vogt, C., Laberg, J. S., Hjelstuen, B. O., Smelror, M., Larsen, E., Andreassen, K., Eidvin, T and Vorren, T. O. (2009). The Plio-Pleistocene glaciation of the Barents Sea–Svalbard region: a new model based on revised chronostratigraphy. *Quaternary Science Reviews*, *28*(9), 812-829.

Knudsen, K. L., Eiríksson, J., Jansen, E., Jiang, H., Rytter, F., and Gudmundsdóttir, E. R. (2004). Palaeoceanographic changes off North Iceland through the last 1200 years: foraminifera, stable isotopes, diatoms and ice rafted debris. *Quaternary Science Reviews*, *23*(20), 2231-2246.

Koç, N., Jansen, E., and Haflidason, H. (1993). Paleoceanographic reconstructions of surface ocean conditions in the Greenland, Iceland and Norwegian seas through the last 14 ka based on diatoms. *Quaternary Science Reviews*, *12*(2), 115-140.

Korsun, S. A., Pogodina, I. A., Forman, S. L., and Lubinski, D. J. (1995). Recent foraminifera in glaciomarine sediments from three arctic fjords of Novaja Zemlja and Svalbard. *Polar Research*, *14*(1), 15-32.

Korsun, S., and Hald, M. (1998). Modern benthic foraminifera off Novaya Zemlya tidewater glaciers, Russian Arctic. *Arctic and Alpine Research*, 61-77.

Korsun, S., and Hald, M. (2000). Seasonal dynamics of benthic foraminifera in a glacially fed fjord of Svalbard, European Arctic. *The Journal of Foraminiferal Research*, *30*(4), 251-271.

Kroopnick, P. (1980). The distribution of 13 C in the Atlantic Ocean. *Earth and Planetary Science Letters*. *49*(2), 469-484.

Laberg, J. S., & Vorren, T. O. (1996). The glacier-fed fan at the mouth of Storfjorden trough, western Barents Sea: a comparative study. *Geologische Rundschau*, *85*(2), 338-349.

Laberg, J. S., Andreassen, K., Knies, J., Vorren, T. O., and Winsborrow, M. (2010). Late Pliocene–Pleistocene development of the Barents Sea ice sheet. *Geology*, *38*(2), 107-110.

Łącka, M., Zajączkowski, M., Forwick, M., & Szczuciński, W. (2015). Late Weichselian and Holocene palaeoceanography of Storfjordrenna, southern Svalbard. *Climates of the Past*, *11*, 587-603.

Lambeck, K. (1995). Constraints on the Late Weichselian ice sheet over the Barents Sea from observations of raised shorelines. *Quaternary Science Reviews*, *14*(1), 1-16.

Lambeck, K. (1996). Limits on the areal extent of the Barents Sea ice sheet in Late Weichselian time. *Global and Planetary Change*, *12*(1), 41-51.

Landvik, J. Y., Hjort, C., Mangerud, J., Moller, P., and Salvigsen, O. (1995). The Quaternary record of eastern Svalbard-an overview. *Polar Research*, *14*(2), 95-104.

Landvik, J. Y., Bondevik, S., Elverhøi, A., Fjeldskaar, W., Mangerud, J. A. N., Salvigsen, O., Siegert, M.J., Svendsen, J-I., and Vorren, T. O. (1998). The last glacial maximum of Svalbard and the Barents Sea area: ice sheet extent and configuration. *Quaternary Science Reviews*, *17*(1), 43-75.

Landvik, J. Y., Ingolfsson, O., Mienhert, J., Lehman, S. J., Solheim, A., Elverhøi, A., and Ottesen, D. A. G. (2005). Rethinking Late Weichselian ice-sheet dynamics in coastal NW Svalbard. *Boreas, 34*(1), 7-24.

LeBlanc, L. R., Mayer, L., Rufino, M., Schock, S. G., and King, J. (1992). Marine sediment classification using the chirp sonar. *The Journal of the Acoustical Society of America*, *91*(1), 107-115.

Libby, W. F., Anderson, E. C., and Arnold, J. R. (1949). Age determination by radiocarbon content: world-wide assay of natural radiocarbon. *Science, 109*(2827), 227-228.

Linick, T.W., Damon, P.E., Donahue, D.J., and Jull, A.J. (1989). Accelerator Mass Spectromerty: The New Revolution in Radiocarbon Dating. *Quaternary International*. *1*, 1-6.

Loeblich, A. R., and Tappan, H. (1964). Foraminiferal classification and evolution. *Geological Society of India*, *5*, 5-40.

Loeblich, A. R., and Tappan, H. (1992). Studies in benthic foraminifera. In Y. Takayanagi, & T. Saito (Eds.), *Proceedings of the Fourth International Symposium on Benthic Foraminifera*. Tokyo: Tokai University Press.

Loeng, H. (1991). Features of the physical oceanographic conditions of the Barents Sea. *Polar research*, *10*(1), 5-18.

Lowe, J., and Walker, M. (2015). *Reconstructing Quaternary Environments*. 3rd ed. Oxon: Routledge. 165-171; 267-279.

Lubinski, D. J., Polyak, L., and Forman, S. L. (2001). Freshwater and Atlantic water inflows to the deep northern Barents and Kara seas since ca 13 14 Cka: foraminifera and stable isotopes. *Quaternary Science Reviews*, *20*(18), 1851-1879.

Lucchi, R. G., Pedrosa, M. T., Camerlenghi, A., Urgeles, R., De Mol, B., and Rebesco, M. (2012). Recent submarine landslides on the continental slope of Storfjorden and Kveithola trough-mouth fans (North West Barents Sea). In *Submarine mass movements and their consequences* (pp. 735-745). Springer Netherlands.

Lucchi, R. G., Camerlenghi, A., Rebesco, M., Colmenero-Hidalgo, E., Sierro, F. J., Sagnotti, L., Urgeles, R., Melis, R., Morigi, C., Bárcena, M.A., Giorgetti, G., Villa, G., Persico, D., Flores, J.A., Rigual-Hernández, A.S., Pedrosa, M.T., Macri, P., and Giorgetti, G. (2013). Postglacial sedimentary processes on the Storfjorden and Kveithola trough mouth fans: Significance of extreme glacimarine sedimentation. *Global and planetary change*, *111*, 309-326.

Mackensen, A., Sejrup, H. P., and Jansen, E. (1985). The distribution of living benthic foraminifera on the continental slope and rise off southwest Norway. *Marine Micropaleontology*, *9*(4), 275-306.

Mackensen, A., and Hald, M. (1988). Cassidulina teretis Tappan and C. laevigata d'Orbigny; their modern and late Quaternary distribution in northern seas. *The Journal of Foraminiferal Research*, *18*(1), 16-24.

MacLachlan, S. E., Cottier, F. R., Austin, W. E., and Howe, J. A. (2007). The salinity: δ18O water relationship in Kongsfjorden, western Spitsbergen. *Polar Research*, *26*(2), 160-167.

Mangerud, J., Dokken, T., Hebbeln, D., Heggen, B., Ingólfsson, Ó., Landvik, J.Y., Mejdahl, V., Svendsen, J.I., and Vorren, T.O., (1998). Fluctuations of the Svalbard Barents Sea Ice Sheet during the last 150 000 years. *Quaternary Science Reviews 17*, 11-42.

Mangerud, J., Bondevik, S., Gulliksen, S., Hufthammer, A. K., and Høisæter, T. (2006). Marine 14 C reservoir ages for 19th century whales and molluscs from the North Atlantic. *Quaternary Science Reviews*, *25*(23), 3228-3245.

Moodley, L., and Hess, C. (1992). Tolerance of infaunal benthic foraminifera for low and high oxygen concentrations. *The Biological Bulletin*, *183*(1), 94-98.

Nier, A.O. (1947). A Mass Spectrometer for Isotope and Gas Analysis. *Review of Scientific Instruments*. *18*, 398-411.

Noormets, R., and Flodén, T. (2002). Glacial deposits and ice-sheet dynamics in the north-central Baltic Sea during the last deglaciation. *Boreas*, *31*(4), 362-377.

Nørgaard-Pedersen, N., Spielhagen, R. F., Erlenkeuser, H., Grootes, P. M., Heinemeier, J., and Knies, J. (2003). Arctic Ocean during the Last Glacial Maximum: Atlantic and polar domains of surface water mass distribution and ice cover. *Paleoceanography*, *18*(3).

O'Regan, M., Williams, C., Frey, K., and Jakobsson, M. (2011). A synthesis of the long-term paleoclimatic evolution of the Arctic. *Oceanography*, *24*(3), 66-80.

Ottesen, D., Dowdeswell, J. A., and Rise, L. (2005). Submarine landforms and the reconstruction of fast-flowing ice streams within a large Quaternary ice sheet: The 2500-km-long Norwegian-Svalbard margin (57–80 N). *Geological Society of America Bulletin*, *117*(7-8), 1033-1050.

Ottesen, D. A. G., Dowdeswell, J. A., Landvik, J. Y., and Mienert, J. (2007). Dynamics of the Late Weichselian ice sheet on Svalbard inferred from high-resolution sea-floor morphology. *Boreas*, *36*(3), 286-306.

Ottesen, D., Dowdeswell, J. A., Benn, D. I., Kristensen, L., Christiansen, H. H., Christensen, O., Hansen, L., Lebesbye, E., Forwick, M., and Vorren, T. O. (2008). Submarine landforms characteristic of glacier surges in two Spitsbergen fjords. *Quaternary Science Reviews*, *27*(15), 1583-1599.

Ottesen, D., and Dowdeswell, J. A. (2009). An inter–ice-stream glaciated margin: Submarine landforms and a geomorphic model based on marine-geophysical data from Svalbard. *Geological Society of America Bulletin*, *121*(11-12), 1647-1665.

Pearson, P.N. (2012). Oxygen Isotopes in Foraminifera: Overview and Historical Review. *The Paleontological Society Papers*. *18*, 1-38.

Pedrosa, M. T., Camerlenghi, A., De Mol, B., Urgeles, R., Rebesco, M., and Lucchi, R. G. (2011). Seabed morphology and shallow sedimentary structure of the Storfjorden and Kveithola trough-mouth fans (north west Barents Sea). *Marine Geology*, *286*(1), 65-81.

Piechura, J., and Walczowski, W. (1995). The Arctic Front: structure and dynamics. *Oceanologia*, *37*(1), 47-73.

Polyak, L., and Mikhailov, V. (1996). Post-glacial environments of the southeastern Barents Sea: foraminiferal evidence. *Geological Society, London, Special Publications*, *111*(1), 323-337.

Polyak, L., Korsun, S., Febo, L. A., Stanovoy, V., Khusid, T., Hald, M., Paulsen, B, E., and Lubinski, D. J. (2002). Benthic foraminiferal assemblages from the southern Kara Sea, a river-influenced Arctic marine environment. *The Journal of Foraminiferal Research*, *32*(3), 252-273.

Quadfasel, D., Gascard, J. C., and Koltermann, K. P. (1987). Large-scale oceanography in Fram Strait during the 1984 Marginal Ice Zone Experiment. *Journal of Geophysical Research: Oceans*, *92*(C7), 6719-6728.

Quadfasel, D., Rudels, B., and Kurz, K. (1988). Outflow of dense water from a Svalbard fjord into the Fram Strait. *Deep Sea Research Part A. Oceanographic Research Papers*, *35*(7), 1143-1150.

Rasmussen, T. L., Thomsen, E., Ślubowska, M. A., Jessen, S., Solheim, A., and Koç, N. (2007). Paleoceanographic evolution of the SW Svalbard margin (76 N) since 20,000 14 C yr BP. *Quaternary Research*, *67*(1), 100-114.

Rasmussen, T. L., and Thomsen, E. (2015). Palaeoceanographic development in Storfjorden, Svalbard, during the deglaciation and Holocene: evidence from benthic foraminiferal records. *Boreas*, *44*(1), 24-44.

Ravelo, A.C., and Hillaire-Marcel, C. (2007). The Use of Oxygen and Carbon Isotopes of Foraminifera in Paleoceanography. In: *Foraminifera in Paleoceanography*. Amsterdam: Elsevier. 735-759.

Rebesco, M., Liu, Y., Camerlenghi, A., Winsborrow, M., Laberg, J. S., Caburlotto, A., Diviacco, P., Accettella, D., Sauli, C., Wardell, N., and Tomini, I., (2011). Deglaciation of the western margin of the Barents Sea Ice Sheet—A swath bathymetric and sub-bottom seismic study from the Kveithola Trough. *Marine Geology, 279*(1), 141-147.

Rosoff, D. B., and Corliss, B. H. (1992). An analysis of Recent deep-sea benthic foraminiferal morphotypes from the Norwegian and Greenland seas. *Palaeogeography, Palaeoclimatology, Palaeoecology, 91*(1), 13-20.

Rudels, B. (2009). Arctic ocean circulation. *Encyclopedia of Ocean Sciences. Elsevier*, 211-225.

Salvigsen, O., Forman, S. L., and Miller, G. H. (1992). Thermophilous molluscs on Svalbard during the Holocene and their paleoclimatic implications. *Polar Research*, *11*(1), 1-10.

Schauer, U. (1995). The release of brine-enriched shelf water from Storfjord into the Norwegian Sea. *Journal of Geophysical Research: Oceans*, *100*(C8), 16015-16028.

Seidenkrantz, M. S. (1995). *Cassidulina teretis* Tappan and *Cassidulina neoteretis* new species (Foraminifera): stratigraphic markers for deep sea and outer shelf areas. *Journal of Micropalaeontology*, *14*(2), 145-157.

Sejrup, H. P., Fjaeran, T., Hald, M., Beck, L., Hagen, J., Miljeteig, I., Morvik, I., and Norvik, O. (1981). Benthonic foraminifera in surface samples from the Norwegian continental margin between 62 degrees N and 65 degrees N. *The Journal of Foraminiferal Research*, *11*(4), 277-295.

Sejrup, H. F. (1987). Molluscan and foraminiferal biostratigraphy of an Eemian-Early Weichselian section on Karmøy, southwestern Norway. *Boreas*, *16*(1), 27-42.

Sejrup, H. P., Hjelstuen, B. O., Dahlgren, K. T., Haflidason, H., Kuijpers, A., Nygård, A., Praeg, D., Stoker, M.S., and Vorren, T. O. (2005). Pleistocene glacial history of the NW European continental margin. *Marine and Petroleum Geology*, *22*(9), 1111-1129.

Shackleton, N. J. (1974). Attainment of isotopic equilibrium between ocean water and the benthonic foraminifera genus Uvigerina: isotopic changes in the ocean during the last glacial. In: J. Labeyrie (Ed.), *Me´thodes quantitatives d’ étude des variations du climat au cours du Pl éistocéne*, *219*, 203-209.

Shackleton, N. J., Lamb, H. H., Worssam, B. C., Hodgson, J. M., Lord, A. R., Shotton, F. W., Schove, D.J., and Cooper, L. H. N. (1977). The oxygen isotope stratigraphic record of the late pleistocene [and discussion]. *Philosophical Transactions of the Royal Society of London B: Biological Sciences*. *280*(972), 169-182.

Siegert, M. J. and Dowdeswell, J. A.: Late Weichselian iceberg, surface-melt and sediment production from the Eurasian Ice Sheet: results from numerical ice sheet modelling. *Marine. Geology. 188*, 109–127, 2002.

Sigman, D. M., and Boyle, E. A. (2000). Glacial/interglacial variations in atmospheric carbon dioxide. *Nature*, *407*(6806), 859-869.

Sjøkartverk, N. (1990). Arctic Pilot Svalbard and Jan Mayen. *Statens Kartverk*, *7*, 1-433.

Skirbekk, K., Kristensen, D. K., Rasmussen, T. L., Koç, N., and Forwick, M. (2010). Holocene climate variations at the entrance to a warm Arctic fjord: evidence from Kongsfjorden trough, Svalbard. *Geological Society, London, Special Publications*, *344*(1), 289-304.

Skogseth, R., Haugan, P. M., and Jakobsson, M. (2005). Watermass transformations in Storfjorden. *Continental Shelf Research*, *25*(5), 667-695.

Ślubowska, M. A., Koç, N., Rasmussen, T. L., and Klitgaard-Kristensen, D. (2005). Changes in the flow of Atlantic water into the Arctic Ocean since the last deglaciation: evidence from the northern Svalbard continental margin, 80 N. *Paleoceanography*, *20*(4).

Ślubowska-Woldengen, M., Rasmussen, T. L., Koç, N., Klitgaard-Kristensen, D., Nilsen, F., and Solheim, A. (2007). Advection of Atlantic Water to the western and northern Svalbard shelf since 17,500 calyr BP. *Quaternary Science Reviews*, *26*(3), 463-478.

Ślubowska-Woldengen, M., Koç, N., Rasmussen, T. L., Klitgaard-Kristensen, D., Hald, M., and Jennings, A. E. (2008). Time-slice reconstructions of ocean circulation changes on the continental shelf in the Nordic and Barents Seas during the last 16,000 cal yr BP. *Quaternary Science Reviews*, *27*(15), 1476-1492.

Steinsund, P. I. (1994). Benthic foraminifera in surface sediments of the Barents and Kara seas: modern and late Quaternary applications. *Unpublished PhD Thesis, University of Tromsø.*

Stuiver, M., and Reimer, J. (1993). Extended 14C data base and revised CALIB 3.014 C age calibration program. *Radiocarbon*, *35*, 215-230

Stuiver, M., and Grootes, P.M., 2000. GISP2 oxygen isotope ratios. *Quaternary Research, 53*, 277–284.

Stuiver, M., Reimer, P. J., and Reimer, R. W. (2005). CALIB 5.0. [WWW program and documentation].

Svendsen, J. I., and Mangerud, J. (1997). Holocene glacial and climatic variations on Spitsbergen, Svalbard. *The Holocene*, *7*(1), 45-57.

Tappan, H., & Loeblich, A. R. (1988). Foraminiferal evolution, diversification, and extinction. *Journal of Paleontology*, *62*(05), 695-714.

Thiede, J., Pfirman, S., Schenke, H. W., and Reil, W. (1990). Bathymetry of Molloy Deep: Fram Strait between Svalbard and Greenland. *Marine Geophysical Researches*, *12*(3), 197-214.

Urey, H.C. (1947). The thermodynamic properties of isotopic substances. *Journal of the Chemical Society*. 562-581.

Walker, M. (2005). Radiometric Dating 1: Radiocarbon Dating. In: *Quaternary Dating Methods*. England: John Wiley & Sons Ltd. 17-35.

White, W.M. (2015). Stable Isotope Geochemistry III: Low Temperature Applications. In: *Isotope Geochemistry*. USA: Wiley-Blackwell. 320.

White, W.M. (2015). The carbon cycle, Isotopes, and Climate. In: *Isotope Geochemistry*. USA: Wiley-Blackwell. 317-322.

Wollenburg, J. E., and Mackensen, A. (1998). Living benthic foraminifers from the central Arctic Ocean: faunal composition, standing stock and diversity. *Marine Micropaleontology*, *34*(3), 153-185.

Wynn Jones, Robert (2014). *Foraminifera and their Applications*. Cambridge: Cambridge University Press. 13-122.

Zachos, J., Pagani, M., Sloan, L., Thomas, E., and Billups, K. (2001). Trends, rhythms, and aberrations in global climate 65 Ma to present. *Science*. *292*(5517), 686-693.

Zajączkowski, M., Szczuciński, W., Plessen, B., and Jernas, P. (2010). Benthic foraminifera in Hornsund, Svalbard: Implications for paleoenvironmental reconstructions. *Polish Polar Research*, *31*(4), 349-375.

Zamelczyk, K., Rasmussen, T. L., Husum, K., and Hald, M. (2013). Marine calcium carbonate preservation vs. climate change over the last two millennia in the Fram Strait: Implications for planktic foraminiferal paleostudies. *Marine Micropaleontology*, *98*, 14-27.